



Universitat Autònoma de Barcelona

Department of Telecommunications and Systems Engineering

# PHD THESIS

Specialty : Telecommunications Engineering

## Analysis and Design of Bulk Acoustic Wave Filters Based on Acoustically Coupled Resonators

Edén Corrales López

Thesis Advisors:

Prof. Pedro de Paco Sánchez

Prof. Óscar Menéndez Nadal

Cerdanyola del Vallès (Barcelona), May 2011



*What is research, but a blind  
date with knowledge.*  
William J. Henry



# Abstract

The speedy growth of wireless telecommunication systems has led to an increasing demand for hand-held devices with more and more stringent requisites for microwave filters including better performance, miniaturization and reduced costs.

Until the end of the 90s, filters used in mobile telecommunication applications were based on ceramic and SAW technologies. Ceramic filters could work with acceptable losses of up to 2 GHz but they were large and bulky. SAW filters offer good miniaturization due to their acoustic wave-based operation but they present good performance only at the lower mobile telecommunication frequencies. Moreover, neither ceramic filters nor SAW filters can be integrated on-chip because they are not compatible with CMOS technologies.

A new RF filter technology has emerged during the last decade: BAW technology. BAW filters are perfectly suitable as miniaturized high performance filters for high frequency and power applications. Compared to SAW filter technology, BAW filter solutions can provide lower insertion loss, better selectivity, CMOS compatibility, higher power handling and higher operation frequency.

A BAW CRF is one of the latest BAW filter topologies to offer a range of new and interesting properties compared to its predecessors. Based on the concept of acoustically coupled resonators, it can provide classical and advanced Chebyshev responses, better bandwidths, more miniaturization and mode conversion.

The complexity of a CRF is considerable in terms of design and fabrication due to the quantity of films that it comprises. The number of layers that make up a BAW resonator is already high: a transducer layer composed of a piezoelectric material, electrodes that can be formed of several layers of different metals to combine their properties, temperature-compensation layers to compensate the negative temperature coefficient for stiffness of the piezoelectric materials and passivation layers. In the case of SMR resonators, multiple layers acting as a Bragg reflector confine the acoustic wave in the resonator. A CRF comprises at least two resonators with their associated layers and also the set of coupling layers that control their mechanical interaction.

The design of BAW filters is based on sizing the layers of the physical device. It becomes complicated with this amount of layers, and optimization procedures may not be efficient due to the number of variables involved in the process. A methodology to analyze and synthesize BAW CRFs is presented in this work. The techniques can deal with multilayered structures in a straightforward way.

This dissertation focuses on the CRF device and is divided into two main blocks. The first block presents a set of fully electric circuitual models that simplify, represent and gather the behavior of CRFs, devices that work both in the electrical and the mechanical domains. The block starts with a chapter in which the analogy between mechanical and electrical variables and the one-dimensional approximation of propa-

gation in thin-film plates enable the network representation of a BAW resonator. A set of tools to analyze the resonator by means of network theory is established and is the basis for analyzing structures composed of several resonators and multiple thin-film layers. In the following chapter, a model for the most basic CRF is developed using network transformations and approximations regarding the frequencies of operation of the BAW devices. The model presents a simplified circuit topology that will enable the device to be linked with filter synthesis techniques. Then, the model is extended to more complex situations with a higher number of coupled resonators and asymmetric structures. Lastly, the set of coupling layers, a key mechanism in CRFs, is discussed and a set of closed-form expressions for their design is presented.

In the second block a profound analysis of BAW CRFs is presented using the proposed models as an enabling tool to guide the analytical procedure. The analysis of those filters facilitates a better understanding of their performance and a way to establish the limits on the responses that they can provide. Systematic filter design methodologies are presented in order to obtain the structure geometries and topologies of BAW filters to fulfill prescribed responses in such a way that fully time-consuming and sometimes not very controlled optimization-oriented procedures are avoided. Therefore, the design of the filter from a clear understanding of its performances facilitates the exploitation of its inherent characteristics. Then, advanced responses with transmission zeros or stopband filters coming from new devices are synthesized by means of the proposed methodologies.

# Resum

El ràpid creixement de sistemes de telecomunicacions sense fils ha portat a un augment en la demanda de dispositius mòbils que incorporin filtres de microones amb requisits cada vegada més exigents incloent millors prestacions, miniaturització i reducció de costos.

Fins a finals dels anys 90, els filtres utilitzats en aplicacions de telecomunicacions mòbils estaven basats en tecnologia ceràmica o SAW. Els filtres ceràmics podien operar amb pèrdues acceptables fins a 2 GHz però eren grans i voluminosos. Els filtres SAW ofereixen un alt grau de miniaturització gràcies a la seva operació basada en ona acústica però només presenten un bon comportament a les freqüències baixes de les aplicacions de telecomunicacions mòbils. A més a més, cap de les dos tecnologies pot ser integrada on-chip degut a la seva incompatibilitat amb tecnologia CMOS.

Una nova tecnologia de filtres de RF ha emergit durant la darrera dècada, la tecnologia BAW. Els filtres BAW són perfectament adequats per al seu ús com a filtres miniaturitzats de elevades prestacions per a alta freqüència i per a aplicacions de potència. En comparació amb la tecnologia SAW, les solucions basades en filtres BAW ofereixen menors pèrdues d'inserció, una millor selectivitat, compatibilitat CMOS, major maneig de potència i poden operar a freqüències majors.

Un CRF és una de les topologies de filtre BAW més recents i ofereix una sèrie de noves i interessants característiques respecte els seus predecessors. Basat en el concepte de ressonadors acoblats acústicament, pot oferir respostes de tipus Chebyshev clàssiques i avançades, millores en l'ample de banda, alts graus de miniaturització i conversió de modes.

La complexitat d'un CRF és considerable en quant a disseny i fabricació degut a la quantitat de làmines que el componen. Tan sols el número de capes que componen un ressonador BAW ja és elevat: una capa de transducció composta per un material piezoelèctric, elèctrodes que poden estar formats per diferents metalls per combinar les seves propietats, capes de compensació de temperatura i capes de passivació. En el cas de ressonadors de tipus SMR múltiples capes implementen un reflector de Bragg que confina l'ona acústica en el ressonador. Un CRF està compost de com a mínim dos ressonadors amb les seves corresponents capes i a més, el conjunt de capes d'acoblament que controlen la seva interacció mecànica.

El disseny dels filtres BAW consisteix en dimensionar les geometries de les capes que componen el dispositiu físic. Això resulta complicat amb aquesta quantitat de capes que hi són presents i per tant tècniques d'optimització poden no ser eficients degut a l'elevat número de variables que intervenen en el procés. En aquest treball es presenta una metodologia per analitzar i sintetitzar dispositius CRF. Les tècniques presentades permetran tractar complexes estructures multicapa d'una manera senzilla i clara.

Aquesta tesi està enfocada en el dispositiu CRF i està dividida en dos blocs

principals. El primer bloc presenta un conjunt de models circuitalment completament elèctrics, que simplifiquen, representen i reuneixen el comportament dels CRFs, dispositius que operen en els dominis elèctric i mecànic. Aquest bloc comença amb un capítol on s'estableix l'analogia entre les variables elèctriques i mecàniques i s'explica l'aproximació unidimensional de propagació en làmines primes que permet la representació circuital del ressonador BAW. S'estableixen un conjunt d'eines per analitzar el ressonador mitjançant teoria de xarxes i aquestes serveixen de base per analitzar estructures compostes de varis resonadors i per múltiples làmines. En el següent capítol, es proposa un model pel CRF bàsic desenvolupat mitjançant transformacions de xarxes i aproximacions al voltant de les freqüències d'operació dels dispositius BAW. El model presenta una topologia circuital simplificada que permetrà enllaçar el dispositiu amb tècniques de síntesi de filtres. Llavors el model s'estén a situacions més complexes amb un major número de resonadors i a estructures asimètriques. Finalment, les capes d'acoblament, mecanisme clau en el CRF, s'analitzen i s'ofereixen un conjunt d'expressions pel seu disseny.

En el segon bloc s'analitza en profunditat el CRF mitjançant els models proposats com a eines que permeten guiar el procés d'anàlisi. L'anàlisi d'aquests filtres permet un millor enteniment del seu comportament i una forma d'establir els límits en les respostes que poden oferir. Es presenten metodologies de disseny de filtres per tal de dimensionar les geometries de les estructures i definir les topologies dels filtres BAW que permeten satisfer respostes prescrites de tal manera que s'eviten els processos d'optimització que poden arribar a ser massa costosos en quant a temps de disseny i de vegades no massa controlats. Per tant, el disseny del filtre a partir d'un clar enteniment del seu comportament fa possible explotar les seves característiques inherents. Llavors, es sintetitzaran respostes avançades amb zeros de transmissió i filtres rebuig de banda a partir de nous dispositius proposats a partir d'aquestes metodologies de disseny.

# Resumen

El rápido crecimiento de sistemas de telecomunicaciones inalámbricas ha llevado a un aumento en la demanda de dispositivos móviles que incorporen filtros de microondas con requisitos cada vez más exigentes incluyendo mejores prestaciones, miniaturización y reducción de costes.

Hasta finales de los años 90, los filtros utilizados en aplicaciones de telecomunicaciones móviles estaban basados en tecnología cerámica o SAW. Los filtros cerámicos podían operar con pérdidas aceptables hasta 2 GHz pero eran grandes y voluminosos. Los filtros SAW ofrecen un alto grado de miniaturización gracias a su operación basada en onda acústica pero sólo presentan un buen comportamiento en las frecuencias bajas de las aplicaciones de telecomunicaciones móviles. Además, ninguna de las dos tecnologías puede ser integrada on-chip debido a su incompatibilidad con tecnología CMOS.

Una nueva tecnología de filtros de RF ha emergido durante la última década, la tecnología BAW. Los filtros BAW son perfectamente adecuados para su uso como filtros miniaturizados de elevadas prestaciones para alta frecuencia y aplicaciones de potencia. En comparación con la tecnología SAW, las soluciones basadas en filtros BAW ofrecen menores pérdidas de inserción, una mejor selectividad, compatibilidad CMOS, mayor manejo de potencia y pueden operar a frecuencias mayores.

Un CRF es una de las topologías de filtro BAW más recientes y ofrece una serie de nuevas e interesantes características respecto a sus predecesores. Basado en el concepto de resonadores acoplados acústicamente, puede ofrecer respuestas de tipo Chebyshev clásicas y avanzadas, mejoras en el ancho de banda, altos grados de miniaturización y conversión de modo.

La complejidad de un CRF es considerable en cuanto a diseño y fabricación debido a la cantidad de láminas que lo componen. Tan solo el número de capas que componen un resonador BAW ya es elevado: una capa de transducción compuesta por un material piezoeléctrico, electrodos que pueden estar formados por diferentes metales para combinar sus propiedades, capas de compensación de temperatura y capas de pasivación. En el caso de resonadores de tipo SMR múltiples capas implementan un reflector de Bragg que confina la onda acústica en el resonador. Un CRF está compuesto de al menos dos resonadores con sus correspondientes capas y además, el conjunto de capas de acoplamiento que controlan su interacción mecánica.

El diseño de los filtros BAW consiste en dimensionar las geometrías de las capas que componen el dispositivo físico. Esto resulta complicado con tal cantidad de capas presentes y por tanto técnicas de optimización pueden no ser eficientes debido al elevado número de variables que intervienen en el proceso. En este trabajo se presenta una metodología para analizar y sintetizar dispositivos CRF. Las técnicas presentadas permitirán tratar complejas estructuras multicapa de una manera sencilla y clara.

Esta tesis está enfocada en el dispositivo CRF y está dividida en dos bloques principales. El primer bloque presenta un conjunto de modelos circuitales completamente eléctricos, que simplifican, representan y reúnen el comportamiento de los CRFs, dispositivos que operan en los dominios eléctrico y mecánico. Este bloque comienza con un capítulo donde se establece la analogía entre las variables eléctricas y mecánicas, explica la aproximación unidimensional de propagación en láminas delgadas que permite la representación circuital del resonador BAW. Se establecen un conjunto de herramientas para analizar el resonador mediante teoría de redes y estas sirven de base para analizar estructuras compuestas de varios resonadores y por múltiples láminas. En el siguiente capítulo, se propone un modelo para el CRF básico desarrollado mediante transformaciones de redes y aproximaciones en torno a las frecuencias de operación de los dispositivos BAW. El modelo presenta una topología circuital simplificada que permitirá enlazar el dispositivo con técnicas de síntesis de filtros. Luego, el modelo se extiende a situaciones más complejas con un mayor número de resonadores y estructuras asimétricas. Entonces, las capas de acoplamiento, mecanismo clave en el CRF, se analizan y se ofrece un conjunto de expresiones para su diseño.

En el segundo bloque se analiza en profundidad el CRF mediante los modelos propuestos como herramientas que permiten guiar el proceso de análisis. El análisis de estos filtros permite un mejor entendimiento de su comportamiento y una forma de establecer los límites de las respuestas que pueden ofrecer. Se presentan metodologías de diseño de filtros para dimensionar las geometrías de las estructuras y definir las topologías de los filtros BAW que permiten satisfacer respuestas prescritas de tal manera que se eviten los procesos de optimización que pueden llegar a ser demasiado costosos en cuanto a tiempo de diseño y a veces no demasiado controlados. Por lo tanto, el diseño del filtro a partir de un claro entendimiento de su comportamiento hace posible explotar sus características inherentes. Entonces, se sintetizarán respuestas avanzadas con ceros de transmisión y filtros rechazo de banda a partir de nuevos dispositivos propuestos a partir de estas metodologías de diseño.

# Acknowledgements

I would like to take this occasion to acknowledge all the people that has helped me through this Ph.D. dissertation. First of all, I must thank my advisors, Pedro and Óscar, for introducing me in the world of scientific research, for guiding me through my years of education as a researcher and for their motivation. I should also acknowledge all the people who took part in my education from the very beginning.

I would like to thank my colleagues Joan, Jordi Verdú, Jordi Marín, Mónica, Toni, Ramón and Rafa, for the fantastic working environment that has existed over the years that we have worked together and the members of the Antenna and Microwave Systems group Josep and Gary. Their spirit of collaboration and support has been very helpful. Humberto from CNM has allowed the understanding of fabrication procedures in clean rooms and their complexity. I would also like to refer to my old friends, among them I must mention Carlos who has followed a parallel path in the computer engineering field and we have shared multiple discussions.

I would also like to thank the RF Acoustic Devices R&D team at TriQuint Semiconductor in the US, where I carried out my stay. Robert gave me the chance to do the stay. The conversations with Gernot were really worthy because of his sharp and dynamic mind. Greg immersed me in the coupled resonator filter fabrication issues.

Last but not least, I would specially like to thank my family. My parents, Xavi and Hèctor have always supported me and Anna has been very important for me.



# Contents

<b>Acronyms</b>	<b>xxiii</b>
<b>1 Introduction</b>	<b>1</b>
1.1 Wireless Telecommunication RF Filters Scenario . . . . .	1
1.2 Bulk Acoustic Wave Resonators . . . . .	4
1.2.1 Electrical Input Impedance Characteristic . . . . .	5
1.2.2 Confinement of the Acoustic Wave . . . . .	6
1.2.3 Parameters of Interest . . . . .	8
1.2.4 Materials . . . . .	9
1.3 Types of BAW Filters . . . . .	11
1.3.1 Ladder Filters . . . . .	11
1.3.2 Lattice Filters . . . . .	13
1.3.3 Stacked Crystal Filters . . . . .	14
1.3.4 Coupled Resonator Filters . . . . .	16
1.4 Objectives . . . . .	19
1.5 Outline of the Dissertation . . . . .	21
1.6 Research Contributions . . . . .	22
1.7 Other Research Contributions . . . . .	23
<b>2 Bulk Acoustic Wave Device Basics</b>	<b>27</b>
2.1 Types of Acoustic Waves . . . . .	28
2.2 Device Physics . . . . .	28

2.2.1	Stress . . . . .	28
2.2.2	Strain . . . . .	30
2.2.3	Stiffness . . . . .	30
2.2.4	One-dimensional Approximation . . . . .	31
2.3	Bulk Acoustic Wave Propagation in Non-piezoelectric Slabs . . . . .	32
2.3.1	Acoustic Wave Equation . . . . .	32
2.3.2	Acoustic Transmission Line Model . . . . .	34
2.4	Piezoelectric Plates . . . . .	37
2.4.1	Constitutive Relations . . . . .	37
2.4.2	Mason Model . . . . .	38
2.5	Closed-form Expression for the Input Impedance of a BAW Resonator . . . . .	41
2.6	Bragg Reflectors . . . . .	43
2.6.1	Quarter-wave Reflector . . . . .	43
2.6.2	Shear Wave Leakage . . . . .	45
2.6.3	Optimized Reflectors for Longitudinal and Shear Modes . . . . .	47
2.7	Summary . . . . .	50
<b>3</b>	<b>Equivalent Electrical Models for Acoustically Coupled Resonators</b> . . . . .	<b>51</b>
3.1	CRF Equivalent Electrical Model . . . . .	52
3.1.1	Definitions and Network Transformations . . . . .	53
3.1.2	Synthesis of the Series Impedance $Z_a/2$ . . . . .	58
3.1.3	Validation of the Proposed Model of a CRF . . . . .	59
3.1.4	Bandpass Prototype Filter Analogy . . . . .	60
3.2	CRF with Multiple Acoustically Coupled Resonators . . . . .	63
3.2.1	CRF Equivalent Network . . . . .	64
3.2.2	Equivalent Electrical Model for the Multi-resonator CRF and Bandpass Filter Analogy . . . . .	65
3.3	Asymmetrically Coupled Resonator Structures . . . . .	66
3.3.1	Structure Definition . . . . .	67
3.3.2	Electrical Equivalent Circuit . . . . .	69

3.3.3	Validation of Asymmetrical Structures Using 3D Simulations . . .	71
3.4	Coupling Layers Mechanism . . . . .	74
3.4.1	Multiple Coupling Layers as a Coupling Mechanism . . . . .	74
3.4.2	Generalized Impedance Inverter . . . . .	76
3.4.3	Closed-Form Expressions for the Coupling Layers Dimensions . .	77
3.4.4	Coupling Layers Frequency Behavior . . . . .	79
3.5	Single Coupling Layer . . . . .	82
3.6	Summary . . . . .	83
<b>4</b>	<b>Design of Acoustically Coupled Resonator Filters</b>	<b>85</b>
4.1	Coupling Matrix of Coupled Resonator Circuits . . . . .	87
4.1.1	The $N + 2$ Coupling Matrix . . . . .	87
4.1.2	Relationships between Coupling Matrix Elements and External Quality Factors, Coupling Coefficients and Resonance Frequencies	89
4.1.3	Extraction of Coupling Coefficients and External Quality Factors	90
4.2	The Coupling Technique in Bulk Acoustic Wave Coupled Resonator Filters	92
4.2.1	Electrical Equivalent Circuit . . . . .	93
4.2.2	Analysis and Design of a CRF . . . . .	96
4.2.3	Example CRF Geometry and Response . . . . .	109
4.3	Advanced Responses with CRFs . . . . .	112
4.3.1	Parallel Connected CRFs . . . . .	112
4.3.2	Folded Canonical Configuration with CRFs . . . . .	120
4.4	Advanced Responses with SCFs . . . . .	127
4.5	Summary . . . . .	133
<b>5</b>	<b>CRF Functionalities beyond the Bandpass Filter</b>	<b>137</b>
5.1	Bandstop BAW Coupled Resonator Filters . . . . .	137
5.1.1	Direct-Coupled Bandstop Filters . . . . .	138
5.1.2	Example of a Bandstop Filter with Parallel Connected CRFs . .	138
5.2	Single to Balanced Mode Operation with Coupled Resonator Filters . .	141

5.2.1	SE2DE CRF Filter with Impedance Transformation Ratio 1:4 . . .	142
5.2.2	SE2DE CRF Filter with Arbitrary Impedance Transformation Ratio 1:t . . . . .	146
5.3	Summary . . . . .	150
<b>6</b>	<b>Conclusions and Future Work</b>	<b>151</b>
6.1	Conclusions . . . . .	151
6.2	Future Work . . . . .	153
	<b>Appendix</b>	<b>155</b>
<b>A</b>	<b>Properties of Selected Materials</b>	<b>155</b>
<b>B</b>	<b>Coupling Matrix Generation</b>	<b>157</b>
B.1	Polynomial Based Chebyshev Filter Functions . . . . .	158
B.2	Coupling Matrix Synthesis . . . . .	161
B.2.1	Admittance Matrix $[Y_N]$ from the $S_{21}$ and $S_{11}$ Polynomials . . .	161
B.2.2	Admittance Matrix $[Y_N]$ from the Canonical Transversal Array .	162
B.2.3	Transversal Coupling Matrix . . . . .	163
B.3	Coupling Matrix Reduction . . . . .	164
B.4	Graphical User Interface . . . . .	164

# List of Figures

1.1	Market evolution for BAW filters and duplexers [5]. . . . .	3
1.2	Mobile commercial applications mapped to current RF filter technologies, performance and frequencies [9]. . . . .	4
1.3	(a) Cross-section of the simplest BAW resonator and (b) electrical equivalent model of a BAW resonator, the BVD model. . . . .	5
1.4	(a) Measured electrical input impedance of a BAW resonator and (b) its Smith chart (courtesy of Triquint). . . . .	6
1.5	FBAR technology. (a) Cross section diagram of a FBAR resonator with pothole process manufacturing and (b) SEM micrograph of an "Air Bridge" FBAR resonator [16] manufactured using surface micromachining. . . . .	7
1.6	SMR technology. (a) Cross section diagram of a SMR resonator and (b) SEM cross-section of 2-pair Tungsten/Oxide composing the SMR [21]. . . . .	8
1.7	FBAR technology. (a) Ladder filter topology and (b) layout [7] . . . . .	11
1.8	(a) Transmission response of one stage of a ladder filter and electrical input impedance of parallel and series resonators and (b) response of a ladder filter with 6-6 construction having equal size series and shunt resonators [37] . . . . .	12
1.9	(a) Lattice filter topology, (b) two-stage lattice BAW filter top view and (c) its corresponding transmission response [40] . . . . .	14
1.10	Stacked Crystal Filter. (a) Cross section, (b) electrical equivalent circuit, (c) representative theoretical response of SCFs showing the three main resonances and, inset, the corresponding internal acoustic displacements for fundamental, second, and third resonances and (d) experimental results for 2-stage SCF [43]. . . . .	15
1.11	Coupled Resonator Filter. (a) Cross section and (b) electrical equivalent circuit. . . . .	17

1.12	(a) Optical and (b) interferometric profilometer view of a two-stage CRF. (c) Transmission and reflection response [49]. . . . .	18
2.1	Types of acoustic waves in solid materials. (a) Longitudinal wave and (b) shear wave. . . . .	29
2.2	Cubic particle in an orthogonal coordinate system subjected to stresses	30
2.3	Transmission line model of a non-piezoelectric slab. . . . .	37
2.4	Mason model of a piezoelectric slab. . . . .	40
2.5	Mason model and transmission line models combined to represent a multilayered model. . . . .	41
2.6	Piezoelectric slab loaded with $Z_1$ and $Z_2$ . . . . .	42
2.7	Electrical input impedance of a measured BAW-SMR resonator (dashed line) and the corresponding Mason model (continuous line) . . . . .	44
2.8	BAW resonator on top of a Bragg mirror composed of $\lambda/4$ layers and the absolute value of the normalized stress in each layer at the operation frequency $f_0=2.4$ GHz. . . . .	45
2.9	(a) Reflectivity and (b) transmissivity of the SMR with quarter-wave layers. . . . .	46
2.10	BAW resonator on top of a Bragg mirror composed of optimized layers to present good reflectivity in both the longitudinal and shear mode and the absolute value of the normalized stress in each layer at the operation frequency $f_0=2.4$ GHz. . . . .	48
2.11	(a) Reflectivity and (b) transmissivity of the SMR with layers thicknesses optimized to offer good reflector behavior in both the longitudinal and the shear mode. . . . .	49
3.1	Coupled resonator filter cross section. . . . .	53
3.2	Set of network transformations to obtain the CRF electrical equivalent model. (a) Original network where the Mason model is applied to each piezoelectric plate. (b) Absorption of the transformers. (c) T to $\Pi$ transformation. (d) Network simplification around the anti-resonance . . . . .	55
3.3	Comparison between the impedance $Z_a/2$ and the impedance of the series LC resonator, $Z_{LC}$ . . . . .	58
3.4	Equivalent circuit model of a Coupled Resonator Filter. . . . .	59

3.5	Simulated transmission response for the proposed equivalent circuit model of the Coupled Resonator Filter (circled line) and for the Mason model based Coupled Resonator Filter (continuous line). . . . .	60
3.6	(a) Reconfigured network of the CRF model (b) Absorption of the transformers. (b) CRF network drawn in order to match the bandpass prototype filter. (c) General bandpass filters using impedance inverters. . .	61
3.7	Impedance inverter equivalence at $f_0$ . . . . .	63
3.8	Cross section of a coupled resonator filter with an additional non-transducing resonator. . . . .	64
3.9	(c) Original network where the Mason and transmission line models are applied to each piezoelectric and non-piezoelectric plate respectively. (b) Electrical equivalent circuit. (c) CRF network in the form of bandpass filter . . . . .	65
3.10	Simulated transmission response for the proposed equivalent circuit model of the Coupled Resonator Filter of order 3 (circled line) and for the Mason model based Coupled Resonator Filter (continuous line). . .	67
3.11	Basic scheme of an acoustically coupled resonator asymmetrical structure.	68
3.12	(a) Network of the asymmetrical structure using the Mason model. (b) Electrical equivalent circuit. . . . .	69
3.13	Transmission response for the asymmetrical CRF structure by means of 1D Mason model (dashed line) and 3D simulation (solid line) including the electrical input impedance of the free-load area.. . . .	73
3.14	Mechanical displacement vector sum for: (a) frequency of maximum transmission and (b) free-load area resonance frequency. . . . .	74
3.15	(a) Three coupling layers behaving as impedance inverter and (b) five coupling layers behaving as impedance inverter. . . . .	77
3.16	Required acoustic lengths to fulfill a particular inverter value using the 3-layer inverter solution. . . . .	80
3.17	Filter response implemented with an ideal inverter such as coupling layers (continuous line) and with real coupling layers (circled line). Evaluation of the implemented multi-layer inverter by means of the magnitude (squared line) and the phase (crossed line) when its ports present the impedance of the desired coupling value, 0.277 kg/s. . . . .	81
3.18	Out-of-band spurious resonances originated from the multi-layer structure in a CRF with an inverter modeling the coupling layers (continuous line) and with real coupling layers (circle line). . . . .	81

3.19	(a) CRF layered structure, (b) CRF with Single Coupling Layer Model and (c) redrawn model to identify resonators and impedance inverters. . . . .	82
4.1	Nodal representation of a multicoupled resonator network. . . . .	87
4.2	(a) Two resonators and their coupling are treated independently to extract the coupling value. (b) Transmission response of the two coupled resonators with their ports decoupled. . . . .	91
4.3	(a) A resonator connected to a port and their coupling are treated independently to extract the external quality factor. (b) Group delay response of $S_{11}$ . . . . .	92
4.4	(a) CRF structure of order 4 and set of couplings that take place. (b) Nodal representation of a bandpass filter of order 4 in mainline configuration. (c) Equivalent electrical circuit composed of two cascaded CRF basic stages. (d) Reconfigured network to identify the coupling and resonance mechanisms. (e) and (f) impedance inverter equivalences. . . . .	94
4.5	Simulation circuits implemented with the Mason model to calculate the couplings that take place in the CRF of order 4. Discontinuous lines refer to acoustic connections between acoustic ports and continuous lines refer to electric connections between electric ports. Note that boxes for piezoelectric plates are composed of 3 ports of the Mason model (2 acoustic ports and 1 electric port) while non-piezoelectric plates are composed of 2 acoustic ports. (a) Circuit to obtain the external quality factor $Q_e$ , (b) the coupling between the lower resonators $k_{23}$ and (c) the coupling between an upper and a lower resonator $k_{12}$ . . . . .	98
4.6	Electrical equivalent circuit for the $Q_e$ measurement . . . . .	100
4.7	External quality factors versus the active area of the BAW resonator for an electrode of $W$ and thickness of 200 nm and the corresponding AlN piezoelectric plate thickness to place the effective resonance at the center frequency of the filter $f_0$ . . . . .	101
4.8	(a) Minimum external quality factor and the corresponding piezoelectric coupling constant that can be achieved for any BAW resonator configuration considering electrodes of $W$ and a piezoelectric of AlN. For every electrode thickness, the piezoelectric thickness is calculated to center the resonator at $f_0$ and the area is selected to minimize the external quality factor. (b) Maximum bandwidth that can be implemented for any BAW resonator configuration and for different RL. . . . .	103
4.9	Electrical equivalent circuit for the $k_{23}$ measurement . . . . .	104

4.10	(a) Coupling values $k_{23}$ and those associated for any lower BAW resonator configuration considering SMR A and SMR B and (b) the corresponding AlN piezoelectric plate thickness to place the effective resonance at the center frequency of the filter $f_0$ . . . . .	106
4.11	(a) Bandwidths that can be implemented for any lower BAW resonator configuration considering SMR A and (b) SMR B. . . . .	107
4.12	Electrical equivalent circuit for the $k_{12}$ measurement . . . . .	108
4.13	(a) Filter response of the CRF of order 4 and (b) comparison of the filter response (continuous line) to an ideal Chebyshev response (dashed line) in a wider frequency span. . . . .	110
4.14	Circuit based on the Mason model to simulate the whole CRF of order 4. . . . .	111
4.15	(a) Nodal representation of a filter network of order 4 in parallel connected configuration. (b) Equivalent networks with series and parallel resonators for a CRF when its parallel capacitors have been removed. . . . .	113
4.16	CRF parallel connected topology. The inverted connection at the lower resonators creates a $180^\circ$ phase shift between branches. . . . .	114
4.17	(a) Mason model configuration to obtain the $Q_e$ of the resonator when the static capacitor is removed by means of a negative capacitor and (b) configuration to extract the inter-resonator coupling. . . . .	116
4.18	$Q_e$ values (continuous line) versus area fulfilling the desired resonance frequency of the resonator composed of a BAW resonator and a shunt cancelling inductor by controlling the piezoelectric thickness $t_p$ (dashed line) . . . . .	117
4.19	(a) Filter response of two parallel connected BAW CRFs and (b) response in a wider span. . . . .	119
4.20	Nodal representation of a filter network of order 4 in folded canonical configuration . . . . .	121
4.21	(a) Folded configuration with parallel LC resonators. (b) Reconfigured network to use series LC resonators. (c) Implementation with CRFs. (d) Equivalent electrical circuit with CRFs. . . . .	122
4.22	Cross section of the CRFs in folded configuration and external elements to implement to topology . . . . .	123
4.23	(a) Mason model configuration to obtain the $Q_e$ of the input/output resonator with folded configuration, (b) inter-resonator coupling between the lower resonators, (c) vertical acoustical coupling and (d) coupling between the input and the output resonators formed by the electrical impedance inverter . . . . .	124

4.24	Equivalent electrical circuit for the extraction of $Q_e$ in the folded configuration. . . . .	125
4.25	Ideal filter response for the folded CRF configuration, response implemented with ideal negative capacitors at the input and output resonators and with inductors . . . . .	127
4.26	(a) Stacked Crystal Filter cross section and (b) model. . . . .	128
4.27	Nodal diagram of the transversal topology. . . . .	129
4.28	Stacked Crystal Filter equivalence to a branch of a transversal topology when the static capacitors are cancelled. . . . .	130
4.29	Transversal configuration with Stacked Crystal Filters. . . . .	132
4.30	(a) Simulation circuit based on the Mason model to extract the $Q_{ei}$ and to center at $f_i$ each resonator $i$ and (b) the equivalent electrical circuit. . . . .	133
4.31	Individual $S_{21}$ response of every Stacked Crystal Filter. . . . .	134
4.32	Response of the transversal SCFs configuration. . . . .	134
5.1	Nodal representation of a bandstop filter of order 4 in parallel connected configuration . . . . .	139
5.2	CRF configuration of the bandstop filter including external elements . . . . .	140
5.3	Response of the stopband filter implemented with CRFs . . . . .	141
5.4	Duplexer block diagram . . . . .	142
5.5	CRF configuration to provide a single-ended to balanced conversion . . . . .	143
5.6	Phase of each branch of the mode-conversion filter with impedance transformation ratio 1:4 . . . . .	145
5.7	Response of the mode-conversion filter with impedance transformation ratio 1:4 . . . . .	146
5.8	CRF configuration to provide a single-ended to balanced conversion and arbitrary 1:t impedance transformation . . . . .	147
5.9	Phase of each branch of the mode-conversion filter with impedance transformation ratio 1:2 . . . . .	149
5.10	Response of the mode-conversion filter with impedance transformation ratio 1:2 . . . . .	149
B.1	Classical Chebyshev response without transmission zeros. . . . .	159
B.2	Chebyshev response with finite transmission zeros at $\pm 4$ rad. . . . .	159

---

B.3	Chebyshev response with finite transmission zeros at $\pm 5$ rad. . . . .	160
B.4	Fully canonical filtering function. . . . .	160
B.5	Canonical Transversal Circuit where $N$ lowpass resonators are coupled to source and load and there exist a direct coupling between source and load. . . . .	162
B.6	Canonical coupling matrix $\mathbf{M}$ for the transversal array . . . . .	164
B.7	(a), (b), (c) and (d) transversal coupling matrixes corresponding to the filter specifications and polynomial coefficients of Figs. B.1, B.2, B.3 and B.4 respectively . . . . .	165
B.8	Graphical user interface of the coupling matrix generation software . . .	166



# List of Tables

3.1	Variables and Elements of the CRF model . . . . .	59
3.2	Variables and Elements of the CRF of order 3 model . . . . .	66
3.3	Definition of Asymmetrical CRF Geometry . . . . .	72
3.4	Structure of the multi-layer inverter . . . . .	78
4.1	Requirements for the example filter and associated couplings . . . . .	99
4.2	Layer thickness of the considered SMR configurations . . . . .	104
4.3	Layer thickness of the CRF . . . . .	109
4.4	Requirements for the example filter with parallel connected configuration and associated couplings . . . . .	115
4.5	Layer thicknesses of the CRF in parallel connected configuration . . . . .	118
4.6	Set of couplings of the folded canonical filter of order 4 . . . . .	124
4.7	Layer thicknesses of the CRF in folded configuration . . . . .	126
4.8	Requirements for the example filter based on SCFs in transversal configuration and associated design parameters . . . . .	130
4.9	SCF dimensions . . . . .	132
5.1	Requirements for the bandstop filter with parallel connected configuration and associated couplings . . . . .	139
5.2	Layer thicknesses of the bandstop CRF . . . . .	140
5.3	Requirements for the mode-conversion filter and associated couplings . . . . .	144
5.4	Layer thicknesses of one CRF stack of the mode-conversion filter . . . . .	145
5.5	Requirements for the mode-conversion filter with impedance transformation ratio 1:2 and associated couplings . . . . .	147

5.6	Layer thicknesses of one CRF stack of the mode-conversion filter with impedance transformation ratio 1:2 . . . . .	148
A.1	Acoustic Properties of Metals . . . . .	155
A.2	Acoustic Properties of Piezoelectric and Dielectric Materials . . . . .	156

# Acronyms

<b>BAW</b>	Bulk Acoustic Wave.
<b>CDMA</b>	Code Division Multiple Access.
<b>CMOS</b>	Complementary Metal-Oxide-Semiconductor.
<b>CRF</b>	Coupled Resonator Filter.
<b>DSBAR</b>	De-Coupled Stacked Bulk Acoustic Resonator.
<b>EDGE</b>	Enhanced Data Rates for GSM Evolution.
<b>ESD</b>	Electrostatic Discharge.
<b>FBAR</b>	Film Bulk Acoustic Resonator.
<b>FBW</b>	Fractional Bandwidth.
<b>FOM</b>	Figure of Merit.
<b>GNSS</b>	Global Navigation Satellite System.
<b>GPRS</b>	General Packet Radio Service.
<b>GSM</b>	Global System for Mobile Communications.
<b>HSDPA</b>	High-Speed Downlink Packet Access.
<b>HSUPA</b>	High-Speed Uplink Packet Access.
<b>IC</b>	Integrated Circuit.
<b>IEEE</b>	Institute of Electrical and Electronics Engineers.
<b>IF</b>	Intermediate Frequency.
<b>ISM</b>	Industrial, Scientific and Medical.
<b>LC</b>	Inductor-Capacitor circuit (L is the symbol for inductance).
<b>LNA</b>	Low Noise Amplifier.
<b>LTE</b>	Long Term Evolution.
<b>mBVD</b>	Modified Butterworth-Van Dyke.

<b>MEMS</b>	Micro-ElectroMechanical Systems.
<b>MMIC</b>	Monolithic Microwave Integrated Circuit.
<b>PCS</b>	Personal Communications System.
<b>RF</b>	Radio Frequency.
<b>RL</b>	Return Loss.
<b>SAW</b>	Surface Acoustic Wave.
<b>SCF</b>	Stacked Crystal Filter.
<b>SE2DE</b>	Single-Ended to Differential.
<b>SiP</b>	System in Package.
<b>SMR</b>	Solidly Mounted Resonator.
<b>SoC</b>	System on Chip.
<b>TEM</b>	Transverse Electro-Magnetic.
<b>TFR</b>	Thin Film Resonator.
<b>TL</b>	Transmission Line.
<b>UMTS</b>	Universal Mobile Telecommunications System.
<b>UWB</b>	Ultra-Wideband.
<b>WCDMA</b>	Wideband Code Division Multiple Access.
<b>WiMAX</b>	Worldwide Interoperability for Microwave Access.
<b>WLAN</b>	Wireless Local Area Network.
<b>WMAN</b>	Wireless Metropolitan Area Network.
<b>WPAN</b>	Wireless Personal Area Network.
<b>WWAN</b>	Wireless Wide Area Network.

# Chapter 1

## Introduction

### 1.1 Wireless Telecommunication RF Filters Scenario

The requirements of wireless devices are continuously changing due to the coexistence and convergence of communication and computing technologies. Wireless wide area networks, WWANs, using mobile telecommunication cellular network technologies, have evolved producing new systems that add to the existing ones, creating a current scenario with a variety of applications such as UMTS, GPRS, EDGE, CDMA2000, GSM, HSDPA, HSUPA, LTE, etc. Wireless local area networks, WLANs, are also extended in the wireless communications, especially the IEEE 802.11 set of standards carrying out WLAN communication in the 2.4, 3.6 and 5 GHz frequency bands. Wireless personal area networks, WPANs, for communication in short distances such as Bluetooth, UWB or ZigBee are also demanded. Wireless metropolitan area networks, WMANs, especially the family of standards IEEE 802.16 commercialized under the name WiMAX are becoming established in the wireless scenario. GNSSs such as the currently fully operational GPS are also being integrated with wireless products and the future European Galileo positioning system or the upcoming restored Russian GLONASS system will also be taken into account once operational.

As can be observed, the network environment is therefore extremely heterogeneous, bringing with it huge challenges for devices that will have to be able to operate under a wide range of frequency bands and protocols. As a consequence, it is highly valuable to use the available frequency spectrum more efficiently.

The control of the spectrum of signals and the handling of interferences in wireless

systems is carried out by means of microwave filters. A microwave filter is a two-port network used to control the frequency response in a microwave system by providing transmission at frequencies within the passband of the filter and attenuation in the stopband of the filter. Guard bands are unused parts of the spectrum between bands that prevent interference. In order to obtain more useable bandwidth the part of the spectrum wasted by guard bands has to be minimized. The minimum width of a guard band is determined by the selectivity of the filter.

The mentioned existing and emerging applications in the constantly growing field of mobile communications are continuously requiring more and more stringent requisites for microwave filters in hand-held devices including better performance, miniaturization and reduced costs.

Ceramic and Surface Acoustic Wave (SAW) filters dominated the markets of wireless telecommunication RF filters until approximately the end of the 90s [1]. Ceramic filters use striplines [2], coupled striplines [3] and other elements with resonant behavior to implement the filters. The size of the ceramic resonators depends on the wavelength of the electromagnetic waves. Although ceramic materials with high dielectric constants are used to shrink the filter, they are still very bulky and large and they usually occupy significant space on the PCB of hand-held devices.

SAW filters are based on the propagation of surface mechanical waves and they can be built very small due to the fact that sound velocity is a factor approximately 10,000 times lower than the velocity of electromagnetic waves [4]. Although SAW filters match the requirements of traditional phone bands, they are not suitable for the most demanding applications. Their limitations stem from the efforts and costs that arise when the filters must work above 2 GHz and their poor power handling capability.

Bulk Acoustic Wave (BAW) technology has emerged during the last decade and is becoming established as a solid option in those applications with stringent requirements [6]. Fig. 1.1 shows the market evolution of filters and duplexers based on BAW technology during recent years. The market of filters has increased every year and has grown exponentially for duplexers. BAW based filters offer high performance, small size, and low cost. Compared to SAW filter technology, BAW filter solutions can provide lower insertion loss, better selectivity, higher power handling, higher operation frequency, and better ESD protection. With these advantages, BAW filter technology has been gaining more market share in wireless communication applications [7]. More-

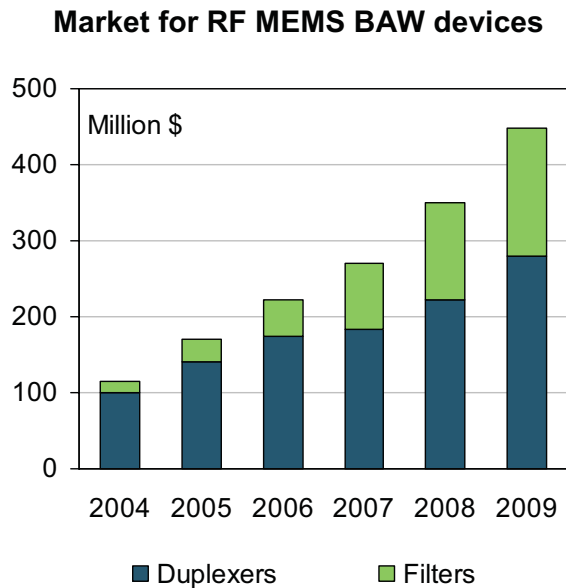


**Figure 1.1:** Market evolution for BAW filters and duplexers [5].

over, BAW technology offers CMOS compatibility, a key element in RF front-ends based on SoC or SiP with other circuitries [8].

Fig. 1.2 shows the broad space that BAW filters may fill in the RF filter scenario. BAW filters are perfectly suitable as high performance filters for high frequency and power applications. SAW filters will probably keep the market for the applications that they are currently serving. This dissertation focuses on BAW technology due to its projection in the RF filter field.

Current BAW technology comes from the classical quartz-crystal technology and the efforts carried out for decades to bring it to RF frequencies. The first publication of a thin film bulk acoustic resonator appeared in 1980 [10] and Zinc Oxide, ZnO, was used as piezoelectric material. In 1982, Lakin, one of the pioneers in BAW technology, stated the potential of thin film BAW resonators [11]. Aluminum Nitride, AlN, was proposed as an alternative piezoelectric material. The advantage of AlN was that it could be easily integrated into an IC facility, while ZnO presents negative aspects in IC facilities such as volatility and contamination.

During the 80s, firms such as Westinghouse researched and assessed resonator usefulness in filter and oscillator circuitry [12]. Research on this technology continued until

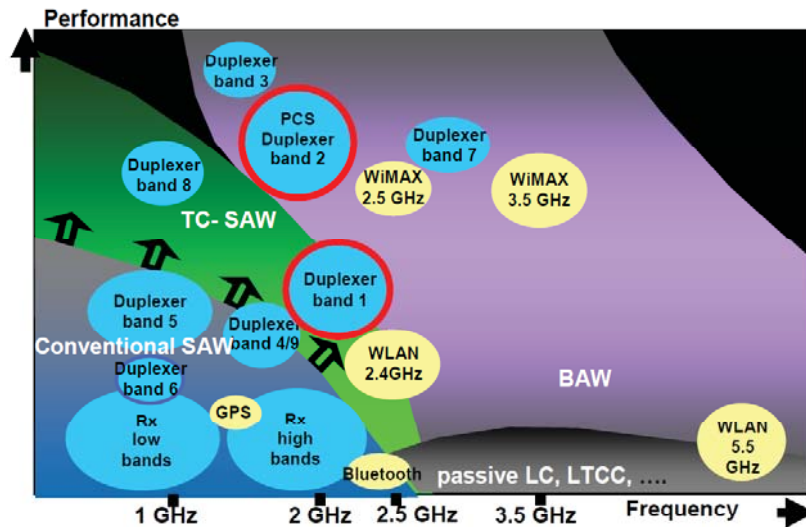


**Figure 1.2:** Mobile commercial applications mapped to current RF filter technologies, performance and frequencies [9].

the decade of the 90s when it vanished due to the reproducibility difficulties of those devices. Nevertheless, in the late 90s, the need for the above-mentioned miniaturized and high-performance filters and the advances in wafer processing in microelectronics aroused interest in BAW technology again [13]. Currently, BAW technology has matured enough to be one of the main trends in RF filters for hand-held devices. Companies that are able to manufacture good RF filters with BAW technology are experiencing success. Many SAW companies are dedicating efforts to research and develop BAW technology due to their success and expectations to cover a great market share. From the research point of view, BAW technology is still a challenging and attractive field where improvements and creations can still take place.

## 1.2 Bulk Acoustic Wave Resonators

The BAW resonator is the core element of BAW technology. It is a piezoelectric device, meaning that the piezoelectric effect brings about the electromechanical conversion. BAW resonators have gained huge popularity in filters but they can also be applied to other applications such as sensors [14] or oscillators [15]. This work focuses on filter applications.

The most basic BAW resonator is composed of a piezoelectric plate sandwiched

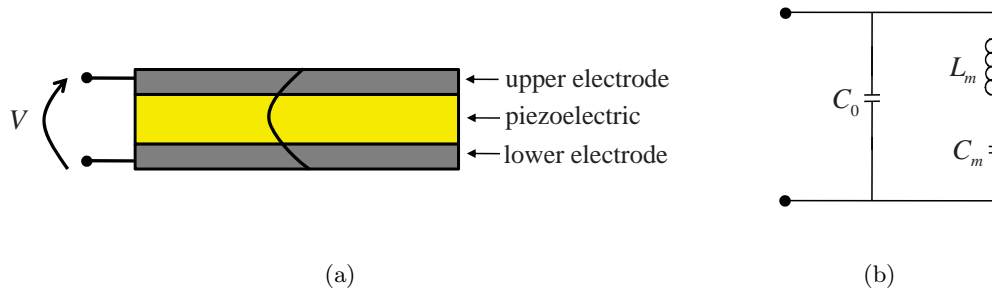


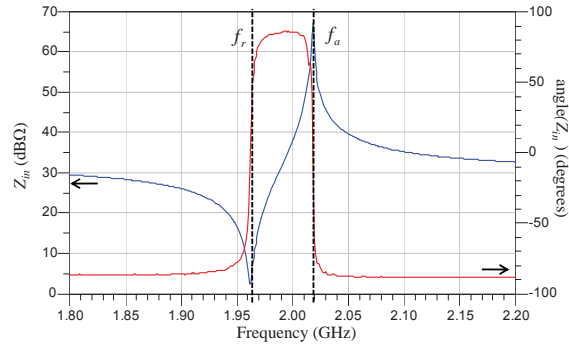
**Figure 1.3:** (a) Cross-section of the simplest BAW resonator and (b) electrical equivalent model of a BAW resonator, the BVD model.

between metallic electrodes and having reflecting boundaries to confine the acoustic wave as shown in Fig. 1.3(a). Geometrically, the resonator is in the form of a simple capacitor. When a voltage difference is applied to the electrodes, an acoustic wave is generated. The main mode of operation of BAW resonators is the thickness or longitudinal mode, meaning that the bulk acoustic wave reflects the larger plate surfaces and the resonance is caused by the wave excitation to the thickness direction.

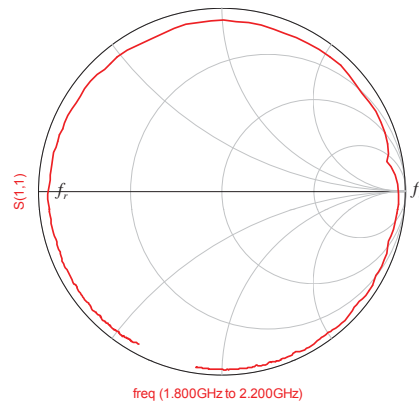
The frequency at which the resonance occurs is determined by the thickness and properties of the piezoelectric layer and the electrodes. In the case of more complex resonators, any additional layer will affect the resonance. There is only one-half of an acoustic wavelength in the resonator plates at the fundamental resonance.

### 1.2.1 Electrical Input Impedance Characteristic

The equivalent circuit of a BAW resonator valid near the fundamental resonance is known as the Butterworth-Van Dyke (BVD) model and its lossless version is shown in Fig. 1.3(b), where  $C_0$  is the static capacitance,  $C_m$  is the motional capacitance and  $L_m$  is the motional inductance. This circuit is of second-order, and it presents a zero and pole as shown in the measured input impedance of a BAW resonator in Fig. 1.4(a). The zero defines the series or resonant frequency  $f_r$ , and the pole defines the parallel or anti-resonant frequency  $f_a$ . The motional branch composed of the series  $L_m C_m$  circuit gathers the acoustic resonance behavior, and parallel to  $C_0$ , forms the parallel resonance. The behavior between the two resonances is inductive; the angle of the impedance is  $90^\circ$ . The behavior out of this range is capacitive with an angle of  $-90^\circ$  and leaning towards  $C_0$ . The Smith chart plot in Fig. 1.4(b) also shows the



(a)



(b)

**Figure 1.4:** (a) Measured electrical input impedance of a BAW resonator and (b) its Smith chart (courtesy of Triqint).

inductive behavior between  $f_a$  and  $f_r$  and the capacitive behavior outside this range of frequencies.

### 1.2.2 Confinement of the Acoustic Wave

BAW resonators can be classified depending on the mechanism that confines the acoustic wave in the resonating structure: FBAR (Film Bulk Acoustic Wave Resonator) and SMR (Solidly Mounted Resonators).

In the case of FBAR, the resonator is surrounded by air by means of micromachining techniques. Fig. 1.5(a) shows the cross section of a FBAR manufactured using the pothole process where a pothole is etched from the rear of the wafer [11]. Air

confines the acoustic wave very well due to its very low impedance related to the resonator materials. Fig. 1.5(b) shows a SEM image of the first FBAR created using a surface machining approach to create the lower air boundary. Surface micromachining is reported to be a more manufacturable process than bulk micromachining.

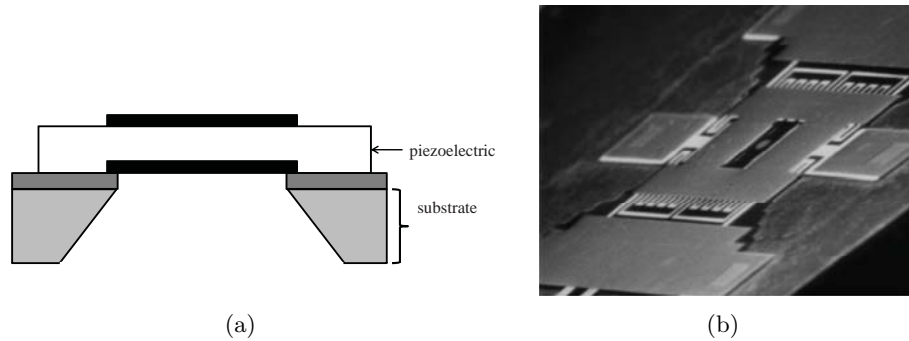


**Figure 1.5:** FBAR technology. (a) Cross section diagram of a FBAR resonator with pothole process manufacturing and (b) SEM micrograph of an "Air Bridge" FBAR resonator [16] manufactured using surface micromachining.

In the case of SMR, see Fig. 1.6(a), an acoustic mirror underneath the device confines this mode. The idea behind the SMR is to obtain a more solid thin film resonator structure than in FBAR which presents more fragile membranes [17]. In [18], the problem of mounting thickness mode piezoelectric resonators on solid structures was addressed for the first time with impedance transforming properties of quarter-wavelength transmission lines. This approach comes from optics and has been extensively developed in that field. The mirror, also known as the Bragg reflector, is formed by a sequence of alternating layers with low and high acoustic impedance forming an approximated acoustic short-circuit or very low effective acoustic impedance seen from its interface with the resonator. Fig. 1.6(b) shows a reflector composed of tungsten and oxide to confine the acoustic energy. Nevertheless, the mirror degrades the quality factor of the resonators and the effective coupling coefficient [19]. In this way, the mirror is an additional part to take into account during the design and optimizations of SMR devices. Recently, a new approach based on reflectors that differ from the traditional quarter-wave nominal thickness has been proposed to avoid losses coming from leaks in the shear mode of propagation [20].

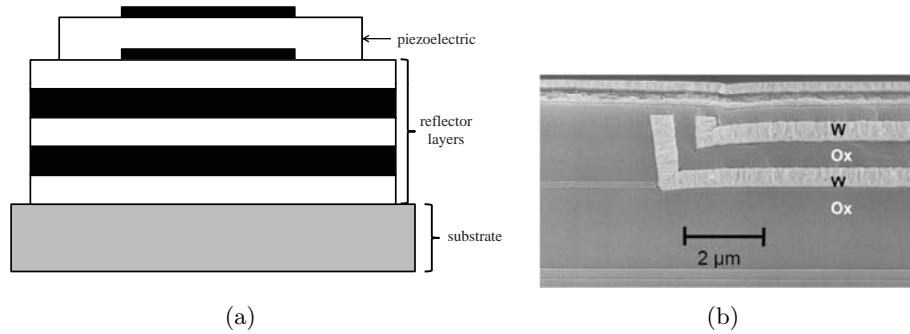


**Figure 1.6:** SMR technology. (a) Cross section diagram of a SMR resonator and (b) SEM cross-section of 2-pair Tungsten/Oxide composing the SMR [21].

### 1.2.3 Parameters of Interest

#### Electromechanical Coupling Coefficient

Electromechanical coupling coefficient,  $k_{eff}^2$ , is one of the biggest challenges in thin-film BAW. It is a highly important parameter for the design of BAW filters because the width of the filter passband that can be achieved depends on it.

The determination of the  $k_{eff}^2$  of a BAW resonator can be obtained from the resonance and anti-resonance frequencies that are measured from its impedance response using:

$$k_{eff}^2 = \frac{\pi f_r}{2 f_a} \frac{1}{\tan\left(\frac{\pi f_r}{2 f_a}\right)} \quad (1.1)$$

The values of  $k_{eff}^2$  achieved in state-of-the-art BAW resonators are about 6.7% at 2 GHz using AlN [22]. This coupling is strongly affected by the electrode materials and configuration and the layer stack including the Bragg reflector. Therefore the set of layers that make up the resonator along with a piezoelectric layer and those layers that modify its boundary conditions can enhance or degrade the coupling depending on their design.

#### Quality Factor

The quality factor,  $Q$ , is a measure of the loss of a resonant circuit and is defined as the ratio of the stored energy divided by the power dissipated in that network over one cycle [23].  $Q$  is a function of the frequency and in this way the quality factor

in a BAW resonator is defined both in the resonance frequency,  $Q_s$ , and in the anti-resonance frequency,  $Q_p$  [24]. Several methods can be found in the literature to calculate the quality factor, such as, for example, calculations based on the BVD model [25] or calculations based on the phase of the impedance extracted from the recorded  $S_{11}$  data [26]. Some of the causes of the losses in a BAW resonator are: electrical resistivity of the electrodes, acoustic leaks, substrate conductivity and acoustic propagation losses. Quality factors of BAW resonators over 2000 have been reported in the literature [22].

The FOM (figure of merit) is defined as the product of the quality factor and the electromechanical coupling constant  $k_{eff}^2$  [19], and sometimes is used to determine how good a resonator is because it gathers the two main parameters of interest of a resonator.

#### 1.2.4 Materials

In this subsection, a brief summary of the most common materials in BAW technology is presented. Although a huge variety of materials has been tested in the literature, here, those materials that have become established in the industry because of their properties, cost, reproducibility and stability have been selected.

##### Piezoelectric Materials

Aluminum Nitride is the most common material for the piezoelectric plates in a BAW device. It can be deposited with high quality in semiconductor facilities on typical metallic electrode materials and can be manufactured in high volumes providing good stability and reproducibility. BAW resonators fabricated with AlN piezoelectric plates can provide typical coupling values of around 6.7%.

Zinc Oxide presents a better coupling coefficient with reported values of  $k_{eff}^2 = 9\%$  [27]. However, ZnO is not currently a viable alternative to AlN for high volumes due to the higher manufacturing difficulties and worse performance in terms of acoustic losses at high frequencies.

Lead zirconate titanate, PZT, presents good performance in terms of coupling, values of  $k_{eff}^2 = 19.8\%$  have been reported in [28], but it presents high intrinsic losses at high frequencies. Lead zirconate titanate also presents a very low acoustic velocity that implies very thin films which render difficult the control of the acoustic behavior.

## Electrode Materials

Aluminum, Al, and alloys of Al present good electrical conductivity but also poor acoustic characteristics because their acoustic impedance is low, which implies a low electromechanical coupling coefficient [29], and therefore, its sole use limits the attainable bandwidths.

Tungsten, W, has a high acoustic impedance and is an excellent material to be used at the Bragg reflector due to the high impedance ratio required between the alternated layers that compose it, and also, at the electrodes due to maximization of the piezoelectric coupling constant [30], [29]. However, its conductivity is significantly lower than Al.

Molybdenum, Mo, has slightly lower acoustic impedance than W and similar conductivity.

The combination of different metals in the electrodes can be used to obtain the good properties of each material: good conductivity and high acoustic impedance. In this case, the outer electrodes are of such high conductivity that they present quite a uniform electrical potential along the layer, and therefore, voltage drops due to current flow along the lateral dimensions of electrodes should not significantly degrade the performance of the resonator. Meanwhile, to achieve an electromechanical coupling enhancement the inner electrodes should exhibit a larger mechanical impedance than the piezoelectric. In [31], a combination of Al and W is used in the electrodes of BAW resonators for this purpose.

Research on electrode materials with good conductivity and high acoustic impedance is still in process. Although some promising materials such as Iridium (Ir) could provide those properties, their compatibility with micro-electronic integrated circuitry processing has still to be assessed [32]. Many other materials have also been investigated such as Platinum [33] and combinations of Tantalum and Ruthenium [34].

## Dielectrics

Silicon dioxide, SiO<sub>2</sub>, presents low acoustic impedance which is favorable for Bragg reflectors. SiO<sub>2</sub> has a positive temperature coefficient and can be used to offset the -25 ppm per degree C coefficient of aluminum nitride [35]. Silicon nitride, SiN, can be used

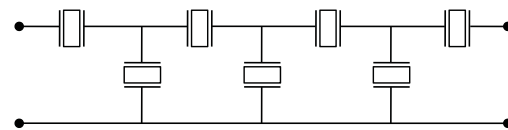
as a passivation layer like in semiconductor manufacturing [36]. Silicon, Si, is basically found in the substrate.

### 1.3 Types of BAW Filters

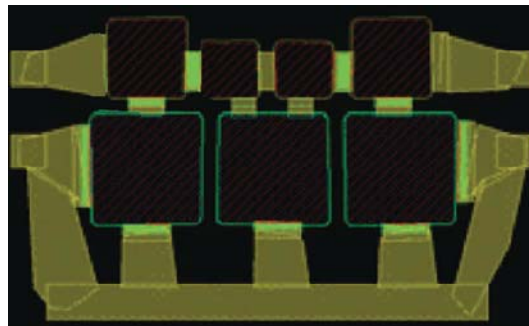
BAW filters can be classified in two main coupling categories: electrically connected resonators, such as ladder and lattice configurations, and acoustically coupled resonators: such as Stacked Crystal Filters, SCFs, and Coupled Resonator Filters, CRFs. Other kinds of BAW filters can be created by combining those basic topologies, or by applying slight changes to the original ones.

#### 1.3.1 Ladder Filters

The typical topology of a ladder-type filter using BAW resonators can be found in Fig. 1.7(a) and a corresponding layout in Fig. 1.7(b). In this case, there are 4 series resonators and 3 parallel resonators and it is called a 4-3. To simplify the analysis of the filter, it is assumed that all the series resonators are identical and all the parallel resonators are identical, but they are different from each other. The frequency difference between the resonance frequency of a series BAW resonator and the parallel one is often called the detuning frequency.

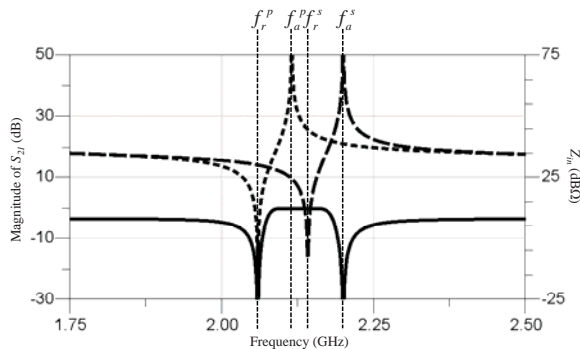


(a)

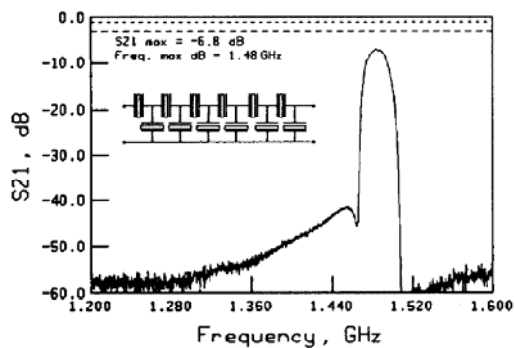


(b)

**Figure 1.7:** FBAR technology. (a) Ladder filter topology and (b) layout [7]



(a)



(b)

**Figure 1.8:** (a) Transmission response of one stage of a ladder filter and electrical input impedance of parallel and series resonators and (b) response of a ladder filter with 6-6 construction having equal size series and shunt resonators [37]

The working principle of one stage of a ladder formed by one BAW resonator in series position and one in parallel can be seen in Fig. 1.8(a), where the transmission response is plotted together with the electrical impedance of the series and parallel BAW resonators. The main feature of this filter is the pair of transmission zeros next to the filter passband, which cause a steep rejection near the passband which is highly desirable for applications that need high selectivity. The lower transmission zero is caused by  $f_r^p$  at which the parallel resonator presents very low impedance grounding the electrical signal, while the upper transmission zero is caused by  $f_a^s$  at which the series resonator presents very high impedance, blocking the way of the electrical signal to the output. Inside the passband,  $f_r^s$  and  $f_a^p$  take place, and the series resonator presents minimum impedance, and the parallel resonator blocks the way of the electrical signal to ground allowing transmission between the input and output.

The drawback of ladder responses is the low rejection at frequencies far from the passband due to the capacitive voltage divider intrinsic to the ladder circuit when the resonators operate as capacitors far from the resonances. This rejection can be improved by adding more stages to the filter but the insertion losses also increase for each new added stage. Fig. 1.8(b) shows the response of a 6-6 ladder filter presented by Lakin et al in TFR Technologies Inc.; the notches typical of ladder filters are distinguished. High bandwidths are difficult to achieve in ladder filters because when the detuning frequency between the series and parallel resonators is too high, the passband is damaged. The design of ladder filters can be performed by means of optimization procedures on the response or by means of systematic analytical procedures [38].

One of the main challenges in BAW filters that require wide relative bandwidths, beyond 4%, is obtaining BAW resonators with piezoelectric coupling constants that can implement them. In recent years, ladder filters have benefited from advances in technological manufacturing processes and from improvements in the quality of the materials.

### 1.3.2 Lattice Filters

Lattice filters, also known as balanced bridge design, are a kind of filter configuration suitable for applications that need balanced networks for direct connection with RF ICs [39].

Fig. 1.9(a) shows one stage of a lattice filter implemented with BAW resonators. It is composed of a bridge structure of 4 resonators: 2 series resonators are placed on the upper and lower branches of the bridge and 2 parallel resonators are connected to the diagonal branches. As is the case with ladder filters, series and parallel resonators are detuned in frequency. When a balanced signal is applied at the inputs of the filter, if all the resonators have the same intrinsic capacitance, the stopbands will present very high attenuation at frequencies far from the resonances, where the resonator behavior is capacitive, due to the perfect balancing structure where the opposite sign and same absolute value input signals cancel each other out. Inside the passband, the path of the electrical signal to one output is allowed from one input where there is a BAW resonator operating with minimum impedance at the resonance frequency, and the path from the other input is blocked by a BAW resonator operating with maximum impedance at the anti-resonance frequency. In this way, inside the passband, there is

no signal cancelation at the outputs. Excellent attenuations can be achieved in the rejection bands with only one lattice stage. The main drawbacks of this configuration are that it offers low selectivity and requires properly balanced input signals. Input signals with phase errors are not filtered correctly.

Fig. 1.9(b) shows a two-stage lattice filter manufactured in the MARTINA project [40]. Fig. 1.9(c) shows its transmission response; the rejection is lower than -50 dB. Configurations with slight variations on the original lattice topology can also be found, as for example in [41], basically combining lattice and ladder sections.

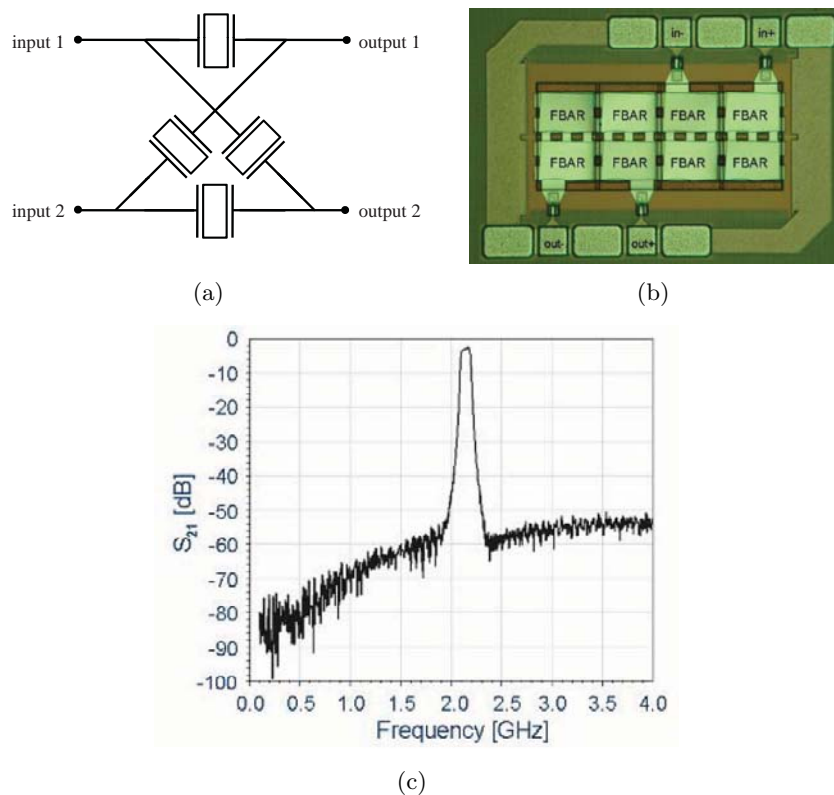


**Figure 1.9:** (a) Lattice filter topology, (b) two-stage lattice BAW filter top view and (c) its corresponding transmission response [40]

### 1.3.3 Stacked Crystal Filters

The stacked crystal filter (SCF) device was proposed in [42] for quartz resonators operating below 10 MHz and according to the principles of thickness modes of vibration in arbitrary stacks. In [43], a thin film implementation of the SCF was presented to

cover microwave applications that were formerly beyond the performance range of quartz crystal SCFs. In [44] experimental results with SCF working up to 12 GHz are presented.

The SCF configuration is shown in Fig. 1.10(a); it is composed of 2 BAW resonators in direct contact and stacked on top of each other separated only by a common ground plane electrode. In the SCF, the 2 BAW resonators are acoustically connected by the direct contact of their faces. The whole stack behaves as a two-port resonator rather than two coupled resonators because there is no acoustic decoupling.

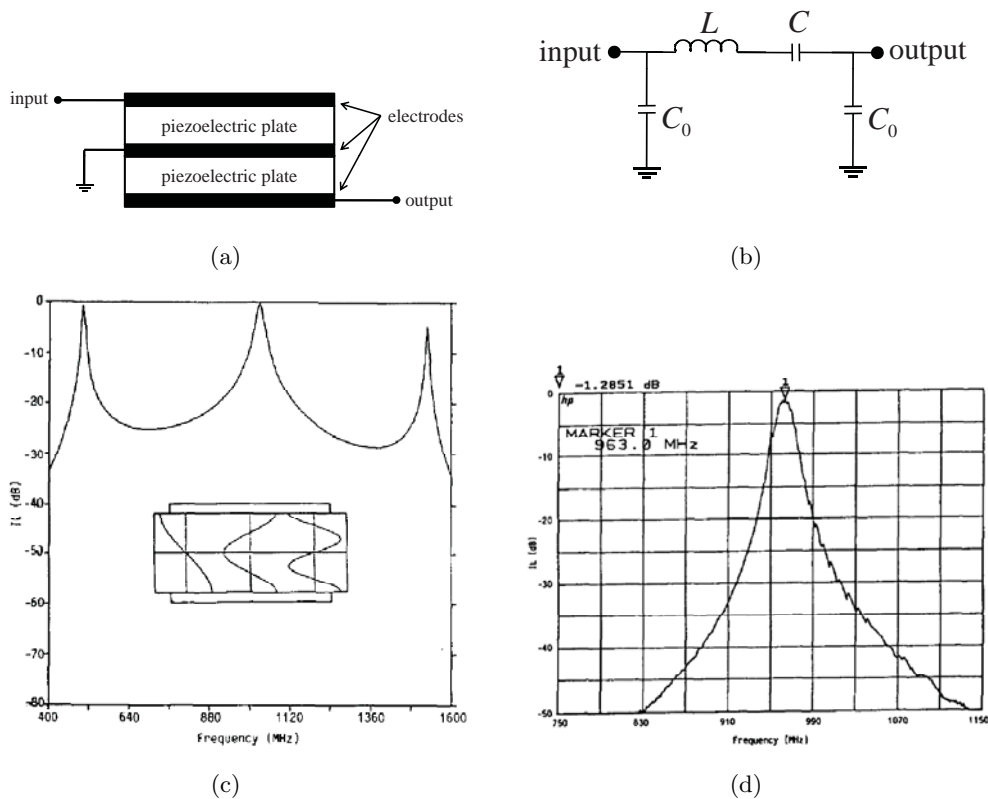


**Figure 1.10:** Stacked Crystal Filter. (a) Cross section, (b) electrical equivalent circuit, (c) representative theoretical response of SCFs showing the three main resonances and, inset, the corresponding internal acoustic displacements for fundamental, second, and third resonances and (d) experimental results for 2-stage SCF [43].

The electrical equivalent circuit of a SCF can be derived from the Mason model as demonstrated in [45] and [46], and is shown in Fig. 1.10(b). It is composed of one shunt capacitor at the input and one at the output of the device modeling the intrinsic capacitance of the resonators. The resonant behavior is modeled by means of the LC

series resonator.

The general nature of the filter passband is illustrated in Fig. 1.10(c) for a theoretical calculation of the filter response for a frequency range covering the three resonances. The inset for Fig. 1.10(c) illustrates the three resonances associated with the three main filter responses. The lowest frequency response corresponds to the fundamental thickness resonance where there is a half wavelength across the entire structure. The second overtone corresponds to a half wavelength across each plate and has the strongest coupling. The filter exhibits the widest bandwidth and lowest insertion loss at the second overtone. Typical experimental devices employ this mode. The third overtone has the weaker coupling. Fig. 1.10(d) shows the measured response of a two-stage SCF working at 963 MHz designed at the second overtone. It presents insertion loss lower than 1.3 dB and a filter bandwidth of 1% [43].

### 1.3.4 Coupled Resonator Filters

The Coupled Resonator Filter (CRF) was proposed in [47] and can be considered as an extension of the SCF structure. It is the key to providing multi-pole filter synthesis by means of resonance splitting due to propagating wave effects as will be shown in this dissertation. A CRF presents a set of coupling layers, as shown in Fig. 3.1, used to acoustically decouple the vertically disposed resonators in such a way that they begin to act as independent resonators rather than as a single resonator. The CRF was initially thought to overcome the limited bandwidth of the SCF thanks to the decoupling of the resonators. However, a basic CRF can be seen as a filter of order 2 and a SCF as a filter of order 1 because of the number of resonators they comprise, which will be shown below in this dissertation. Fig. 1.11(b) shows the electrical equivalent model of the CRF [48] which anticipates the topology of a filter of order 2. It is similar to the SCF model with the difference of having two LC resonators separated by means of an impedance inverter controlling their acoustic coupling.

CRF devices have gained popularity in the last years due to their ability to offer wider bandwidths, Chebyshev responses, miniaturization due to the vertical stacking of resonators and mode conversion.

In [49], a CRF for W-CDMA applications was presented. Aluminum nitride resonators with molybdenum electrodes were acoustically coupled through a W/SiO<sub>2</sub> multi-layered stack and insulated by a fully dielectric SiN/SiOC Bragg mirror. A min-

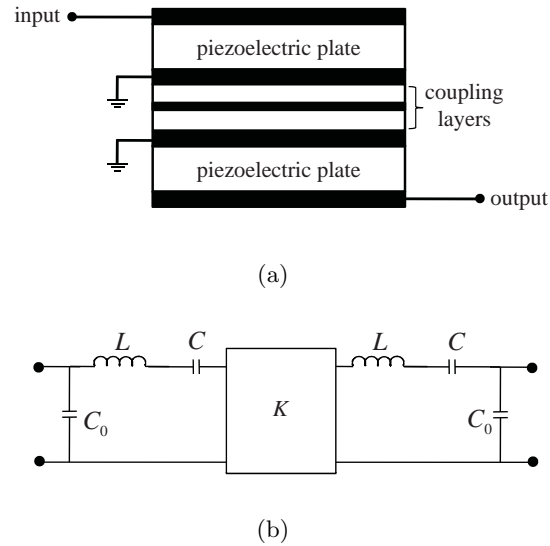


**Figure 1.11:** Coupled Resonator Filter. (a) Cross section and (b) electrical equivalent circuit.

imum insertion loss of 2.9 dB was measured whereas strong spurious resonances were observed. Fig. 1.12(a) and Fig. 1.12(b) show the top-view and the interferometric profilometer view of the CRF device composed of two basic stages electrically connected by means of the lower electrodes of each stack. Fig. 1.12(c) shows the W-CDMA response of the filter.

In lieu of the traditional multi-layer decoupling structure, a technique in which only a single thin polymer layer with appropriate acoustic impedance is used in [50]. The device was called a DSBAR (Decoupled Stacked Bulk Acoustic Resonator) and it demonstrated a 0.4 mm x 0.5 mm filter operating at 2.45 GHz with a bandwidth at the 2 dB points greater than 4%, in-band return loss of less than -10 dB and excellent out-of-band rejection. In [51], the operation of the DSBAR is discussed and it is stated that although it presents a simpler manufacturing process, it is counterbalanced by the high acoustic attenuation of suitable coupler materials. It is also demonstrated that the typically poor near-band rejection of coupled resonator filters can be improved at the die level by connecting a small capacitance between the input and output of the filter to produce a pair of tunable transmission zeros.

In [52], Fattinger et al presented a CRF configuration to provide BAW filters with mode-conversion (single ended to balanced) as well as impedance transformation. Experimental results for CRFs operating at 1.8 GHz manufactured at Infineon Technolo-

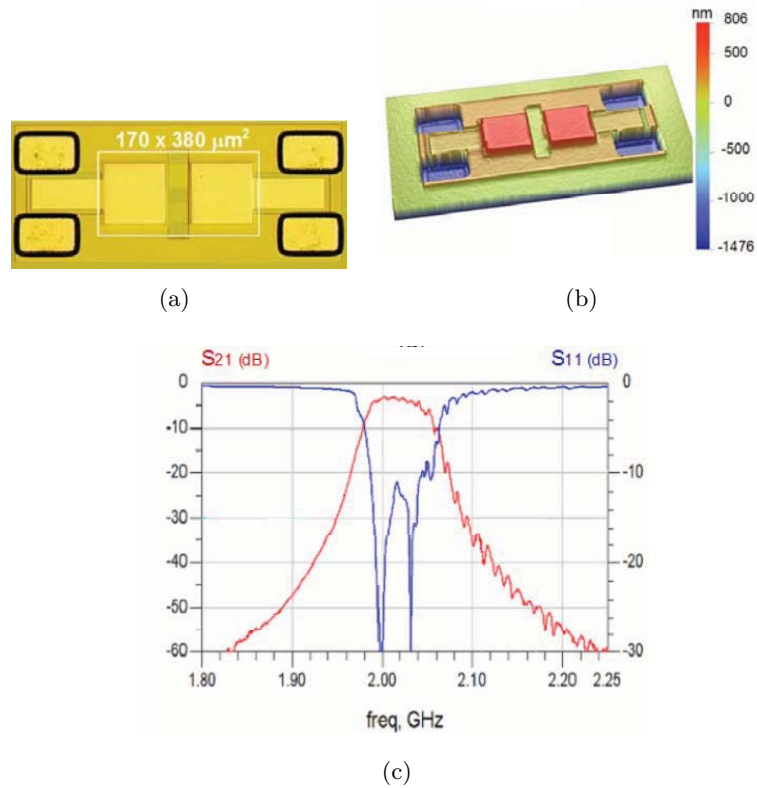


**Figure 1.12:** (a) Optical and (b) interferometric profilometer view of a two-stage CRF. (c) Transmission and reflection response [49].

gies were presented. The total area of the device was of 0.32 mm x 0.42 mm. In [53] the suppression of spurious resonances in CRFs were demonstrated, and unwanted passbands were overcome by modifying the acoustic mirror that attenuated the spurious peaks around 3 GHz by at least 20 dB.

A duplexer based on CRFs for W-CDMA application is presented in [54]. The aim is that the device be integrated in a RF module for cellular phones. It was composed of a single-ended to single-ended filter and a mode conversion filter. The minimum insertion loss for the Tx and Rx filter is better than -3 dB and the isolation between Tx and Rx ports is greater than 60 dB. The rejection of the Tx filter is better than -50 dB in the Rx frequency range and is up to -67 dB in the Tx frequency range. The CRFs are reported to handle up to 27 dBm at Tx center frequency. Coupled resonator filters combined with ladder filters can be found in [55].

## 1.4 Objectives

Bulk acoustic wave devices are based on stacks of multiple thin film layers. Each one of these layers has a specific function in the BAW device to make it operate or to improve its characteristics as explained above. The total number of layers in a BAW device can be raised and that is especially relevant when we refer to multiple stacked resonators such as in SCFs and CRFs. This Ph.D. dissertation focuses on BAW filters based on acoustically coupled resonators with special attention to the CRF.

Since there are no temperature-compensated piezoelectric materials readily available in thin film form, composite structures composed of positive and negative coefficient characteristics may be used. The negative temperature dependence of materials such as AlN, W or Mo, typically present in the resonator stack can be compensated by placing an oxide layer inside the stack which presents a positive temperature coefficient [56].

Regarding the electrode structure, heavy conductor materials such as W or Mo are preferred for metallization in order to increase the electromechanical coupling coefficient. However, their electrical conductivity is not as favorable as other materials such as Al. In this way, as commented above, combinations of heavy materials in the inner electrode layers and good conductor materials in the outer electrode layers can be used to get the best of both kinds of materials [57].

Silicon nitride layers may also be found as a passivation layer like in semiconductor manufacturing [58] and in membrane type-resonators as a supporting membrane [36].

Another important part in the BAW CRF structure is the set of coupling layers implemented between resonators that acoustically connect them and control the degree of acoustic coupling.

Lastly but no less important, the device can lie on a free-standing membrane manufactured following the FBAR approach or on a multilayered Bragg reflector following the SMR approach.

As can be seen from the described CRF layer configuration, there can be a considerable amount of layers in the stack. This level of complexity causes a difficult situation at the moment of analyzing the behavior of the structure and its different parts. It also complicates the design of the filter to fulfill a prescribed response.

The main objective of this work is to offer a procedure that provides a way to analyze the filtering mechanisms and to design a CRF handling with layer structures of any complexity. Relying only on optimization techniques to size a CRF can lead to local solutions that may not make best use of the characteristics of the device, and they may even not converge on a desired point due to bad starting points of solutions. More importantly, a design process focused only on optimization can lead the designer to an obscure process that is far from understanding the mechanisms and effects that take place in the structure. Meanwhile, a clear understanding of those mechanisms can help the designer to choose the best configurations, starting points or even substantial device modifications to improve the overall behavior or to obtain new characteristics.

As a BAW technology device, the CRF works both in the acoustic and in the electromagnetic plane and as a device based on coupled resonators, the way in which its behavior matches the type of coupled resonator circuits developed in electromagnetic filter theory will be demonstrated. A fully electrical circuit will be developed to gather the filter behavior along with its internal coupling and resonating mechanisms. An electrical circuit representation of the device can connect it to the mature electromagnetic filter design theory exploiting its techniques to analyze and synthesize a pure CRF and more complex devices based on CRFs.

This dissertation proposes a set of filter synthesis techniques that have not been applied so far to BAW technology and that facilitate the analysis and design of CRF devices. The strength of the technique is that it can deal with complex multi-layered structures in the same way that it can simple ones. Behavior trends can be obtained to predict how structural changes can modify the device's characteristics and performance limits can be reached. Moreover, a full design and sizing of BAW CRFs can be performed to meet specifications.

Another objective of this work is to propose new devices based on acoustically coupled resonators that are able to synthesize more advanced filter responses than the conventional CRF in terms of obtaining a steeper roll-off for high performance applications.

## 1.5 Outline of the Dissertation

Chapter 1 introduces the BAW technology and reviews its background. The BAW resonator is presented as the fundamental element of this technology and the main BAW filter configurations are explained. The objectives and research contributions of this work are presented.

In Chapter 2, the principles of BAW devices are reviewed paying special attention to the one-dimensional approximation of bulk propagation in thin film plates which is widely extended in BAW device analysis and design.

Chapter 3 develops the equivalent electrical model of the most basic CRF device composed of two mechanically coupled BAW resonators and shows its correspondence to a bandpass filter prototype based on impedance inverters. Therefore, the link between the electro-mechanical device and a fully electrical circuit is created. The model is extended to CRFs composed of a higher number of mechanically coupled resonators and also to asymmetrical CRFs that present different mechanical boundary conditions in different zones of the plate propagation area. Then, the coupling layers mechanism is investigated establishing relationships between the physical slabs that implement it and the coupling levels between resonators.

Chapter 4 uses the theory of couplings for filter design to analyze the coupling and resonance mechanisms that take place in a CRF. A filter of order 4 composed of two basic CRFs has been selected to illustrate the analysis because it gathers the most representative possible couplings that can take place in CRF devices: port-to-resonator coupling, inter-resonator pure acoustic coupling and inter-resonator coupling by means of electric connection. The limits on the achievable couplings set the limits on the response performances that can be obtained in terms of bandwidth and return losses inside the passbands. The couplings technique has been used to fully synthesize bandpass filters with classical Chebyshev responses. Then, the coupling matrix has enabled the synthesis of more advanced responses with CRFs introducing transmission zeros close to the passband and thus, improving the selectivity.

In Chapter 5, two functionalities of CRFs are presented beyond the bandpass one: stopband filters and single-ended to balanced mode conversion. The use of CRFs allows the implementation of bandstop coupling matrixes with a direct source-load coupling providing the advantages of advanced Chebyshev responses. The way in which the

coupling theory can be used to design filters with mode conversion is also demonstrated.

Finally, Chapter 6 ends this Ph.D. dissertation with a summary of the work and the conclusions.

Appendix A gathers the properties of the materials used to obtain the results presented in this work.

Appendix B presents a brief summary of the coupling matrix generation to fulfill prescribed filtering responses. The coupling matrix generation software developed in this work has been an essential tool for the implementation of advances filtering responses.

## 1.6 Research Contributions

This dissertation collects the work that has been carried out during the Ph.D. program. Most of the results have been published in international journals, international conference papers and national conferences. Some results are still pending publication. Next, a list of the contributions in each chapter are presented.

### Chapter 3

- Corrales, E.; Verdu, J.; De Paco, P.; Menendez, O.; , "Analysis technique for asymmetrically coupled resonator structures," *Ultrasonics, Ferroelectrics and Frequency Control, IEEE Transactions on*, vol. 56, no. 8, pp. 1703 - 1707, Aug. 2009
- Corrales, E.; de Paco, P.; Menendez, O.; Verdu, J.; , "Bulk acoustic wave CRF design," *New developments in Micro Electro Mechanical systems for radio frequency and millimeter wave applications.*, pp. 239 - 248, 2009.
- Corrales, E.; de Paco, P.; Menendez, O.; Verdu, J.; , "Design of three-Pole bulk acoustic wave coupled resonator filters," *Microwave Conference, 2008. EuMC 2008. 38th European*, pp. 357 - 360, 27-31 Oct. 2008
- de Paco, P.; Menendez, O.; Corrales, E.; , "Equivalent circuit modeling of coupled resonator filters," *Ultrasonics, Ferroelectrics and Frequency Control, IEEE Transactions on* , vol. 55, no. 9, pp. 2030-2037, Sept. 2008

- Corrales, E.; de Paco, P.; Menendez, O.; Verdu, J.; , "Modelo circuital de un filtro BAW basado en resonadores acoplados acústicamente," *XXIII Simposium Nacional de la Unión Científica Internacional de Radio (URSI 2008)*., 22-24 Sep. 2008.
- Corrales, E.; de Paco, P.; Menendez, O.; , "Closed-form expressions for the design of BAW CRF acoustic inverters," *Journal of Electromagnetic Waves and Applications (JEMWA)*, vol. 23, no. 17-18, pp. 2251 - 2259, 2009

## Chapter 4

- Corrales, E.; de Paco, P.; Menendez, O.; Verdu, J.; , "Design of a WLAN 802.11 b/g RF filter based on electrically connected bulk acoustic wave coupled resonator filter," *10th International symposium on RF-MEMS and RF Microsystems.*, 6 - 8 Jul. 2009.
- Corrales, E.; de Paco, P.; Menendez, O.; , "W-CDMA RF filter with 60 MHz bandwidth based on parallel connected BAW stacked crystal filters," *Progress In Electromagnetics Research Letters*, vol. 14, 171-179, 2010.
- Corrales, E.; de Paco, P.; Menendez, O.; Verdu, J.; , "Analysis and design of coupled resonator filters with a single coupling layer," *Microwave Conference (EuMC), 2010 European*, pp. 300-303, 28-30 Sept. 2010
- Corrales, E.; de Paco, P.; Menendez, O.; , "Analysis of the filtering mechanisms of a bulk acoustic wave coupled resonator filter," submitted.

## 1.7 Other Research Contributions

The author of this Ph.D. dissertation has made other research contributions during the Ph.D. program whose content is not included in the present document. These contributions are:

- Corrales, E.; Menendez, O.; de Paco, P.; Ramirez, M.; Verdu, J.; , "Microstrip dual-band bandpass filter based on the cul-de-sac topology," *Microwave Conference (EuMC), 2010 European* , pp. 549-552, 28-30 Sept. 2010

- de Paco, P.; Verdu, J.; Menendez, O.; Corrales, E.; , "Branch-Line coupler based on edge-Coupled parallel lines with improved balanced response," *Microwave Theory and Techniques, IEEE Transactions on* , vol.56, no.12, pp.2936-2941, Dec. 2008
- Menendez, O.; de Paco, P.; Ramirez, M.; Verdu, J.; Corrales, E.; , "Design, fabrication and measurement of a GPS-Galileo dual-passband filter," *Wireless and Microwave Technology Conference, 2009. WAMICON '09. IEEE 10th Annual* , pp.1-4, 20-21 April 2009
- Verdu, J.; Menendez, O.; de Paco, P.; Corrales, E.; , "Dual bandpass ladder-type filter," *Microwave Symposium Digest (MTT), 2010 IEEE MTT-S International* , pp.1728-1731, 23-28 May 2010
- Menendez, O.; de Paco, P.; Gemio, J.; Verdu, J.; Corrales, E.; "Methodology for designing microwave acoustic filters with Butterworth/Chebyshev response," *International Journal of Microwave and Wireless Technologies* , vol. 1, 11 - 18, 2009.
- Menendez, O.; Verdu, J.; Corrales, E.; de Paco, P.; "A review of recent patents on bulk acoustic wave resonators and filters," *Recent Patents on Electrical Engineering* , vol. 2, 92-108, 2009.
- Menendez, O.; de Paco, P.; Corrales, E.; Verdu, J.; "Procedure for the design of Ladder BAW filters taking electrodes into account," *Progress in Electromagnetics Research Letters* , vol. 7, 127-137, 2009.
- Verdu, J.; de Paco, P.; Menendez, O.; Corrales, E.; "Acoustical structures based on the thickened edge load solution," *New developments in Micro Electro Mechanical systems for radio frequency and millimeter wave applications.*, pp. 221-230, 2009.
- Menendez, O.; de Paco, P.; Corrales, E.; Verdu, J.; "A novel bulk acoustic wave duplexer based on stacked crystal filters for WCDMA handset applications," *New developments in Micro Electro Mechanical systems for radio frequency and millimeter wave applications* , pp. 231-238, 2009.
- Verdu, J.; de Paco, P.; Menendez, O.; Corrales, E.; "Simulation of electromechanical resonators using the finite element method," *10th International symposium on RF-MEMS and RF Microsystems* , 2009.

- Verdu, J.; Menendez, O.; de Paco, P.; Corrales, E.; , "Low order ladder-type filter including reactive elements," *Metamaterials Week* , 2008.
- Corrales, E.; de Paco, P.; Menendez, O.; Verdu, J.; Parron, J.; Villarino, R.; Junkin, G.;, "Implementation of a dual-band mixer using comnposite right/left handed transmission lines," *Metamaterials Week* , 2008.
- Verdu, J.; Menendez, O.; de Paco, P.; Corrales, E.; , "Simulación 3D de estructuras compuestas por resonadores acústicos," *XXIII Simposium nacional de la unión científica internacional de radio* , 2008.
- Menendez, O.; de Paco, P.; Ramirez, M.; Verdu, J.; Corrales, E.; , "Diseño, fabricación y medida de un filtro paso-banda dual GPS-Galileo," *XXIII Simposium nacional de la unión científica internacional de radio* , 2008.



## Chapter 2

# Bulk Acoustic Wave Device Basics

In this chapter, the propagation of an acoustic wave through the bulk of a non-piezoelectric plate will be analyzed. Then, the results will be extended to include piezoelectric plates which combine the effects of acoustic and electric fields. A set of definitions of variables and relationships will be established in three dimensions and the assumptions to proceed with a one-dimensional approximation will be stated. Using the one-dimensional approximation, the plates are considered to be infinite in their lateral dimensions, which means that only waves propagating in the thickness direction are present. This approximation is especially useful in BAW technology where the layers that compose the devices are thin films which can be approximated by infinite lateral dimension slabs related to the thickness dimension.

The analysis of the slabs will show the analogy that exists between the electromagnetic and the acoustic planes, and it will bring about acoustic behavior by means of electric circuits using acoustic variables. A set of tools will be developed to model each layer in a BAW resonator and to gather the behavior of the thickness mode of propagation. The transmission line model for non-piezoelectric slabs and the Mason model for piezoelectric slabs will be developed and they can be considered two relevant tools throughout this work. The development of the one-dimensional mechanical wave, as well as the derived electrical models, comes from the works in [59], [60], [61] and [62].

Then, the Bragg mirror behavior will be analyzed using the propagation expres-

sions. The shear mode of propagation will be shown to be an important loss mechanism in SMRs, and how a proper design of the mirror can correct it improving the quality factor of the resonators will also be demonstrated.

## 2.1 Types of Acoustic Waves

In solid materials there are two basic types of acoustic waves: longitudinal and shear waves [63]. In a longitudinal wave, see Fig. 2.1(a), the particle displacement is parallel to the wave vector (i.e., along the x-direction here). The velocity depends on the material, but is typically in the range of 5000 to 11000 m/s. The second basic wave type is the shear wave, shown in Fig. 2.1(b), in which the displacement is in any direction normal to the wave vector, and this generally has a lower velocity of typically 3000 to 6000 m/s.

## 2.2 Device Physics

### 2.2.1 Stress

Stress is defined as the intensity of internal forces acting between particles of a body across imaginary internal surfaces [64]. It is a measure of the force per unit area of a surface within a deformable body on which internal forces act. Fig. 2.2 shows a cubic particle as a volume element in an orthogonal coordinate system. Each surface of the particle is subject to internal forces. If the stress vectors on three mutually perpendicular planes are known, the stress vector on any plane containing this point can be found from equilibrium conditions at this point.

The stress vector is broken down into two kinds of components: one normal to the plane of the surface that receives its effect, called the normal stress, and the other parallel to this plane, called the shearing stress. The stress vectors associated with the planes x, y and z are also broken down into components in the direction of the three coordinate axes. In this way the stress vector associated with each plane is composed of one normal stress and two shearing stresses:

$$\vec{T}_x = \hat{x}T_{xx} + \hat{y}T_{yx} + \hat{z}T_{zx} \quad (2.1)$$

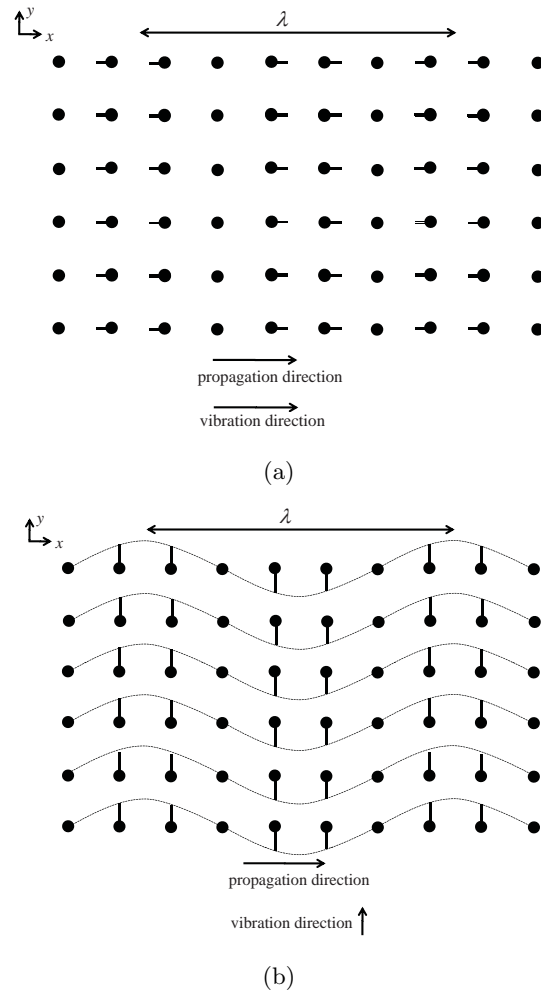


**Figure 2.1:** Types of acoustic waves in solid materials. (a) Longitudinal wave and (b) shear wave.

$$\vec{T}_y = \hat{x}T_{xy} + \hat{y}T_{yy} + \hat{z}T_{zy} \quad (2.2)$$

$$\vec{T}_z = \hat{x}T_{xz} + \hat{y}T_{yz} + \hat{z}T_{zz} \quad (2.3)$$

The nine quantities required to define the three stress vectors are called the components of the stress tensor. From the equilibrium condition that the sum of the moments in any axis must be zero [60], the stress can be expressed with only six independent elements  $T_1=T_{xx}$ ,  $T_2=T_{yy}$ ,  $T_3=T_{zz}$ ,  $T_4=T_{yz}$ ,  $T_5=T_{xz}$ ,  $T_6=T_{xy}$ , and  $T_{xy}=T_{yx}$ ,  $T_{yz}=T_{zy}$ ,  $T_{xz}=T_{zx}$ .

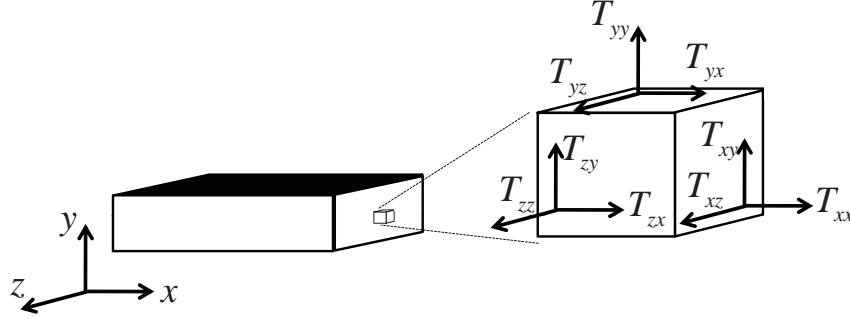


**Figure 2.2:** Cubic particle in an orthogonal coordinate system subjected to stresses

### 2.2.2 Strain

Strain, also known as deformation, is the response of the particle of the body to the stresses in terms of the change in the metric properties in the displacement from an initial position to a final position. If the particle at  $\vec{r}$  from the origin is displaced to position  $\vec{r}'$  by the force then the deformation  $\vec{u} = \vec{r}' - \vec{r}$  is called the displacement vector. Taking into account the cubic particle, the displacement is defined in each of its surfaces in the orthogonal coordinate system  $\{\vec{u}_x, \vec{u}_y, \vec{u}_z\}$ . And the strain is [59]

$$S_{ik} = \frac{1}{2} \left( \frac{\partial u_i}{\partial x_k} + \frac{\partial u_k}{\partial x_i} \right) \quad (2.4)$$

As with stresses, strains are also classified as normal strain and shear strain (i.e. acting normal to or along the surface of the particle respectively). For a normal strain in direction  $i$  the strain expression is simplified

$$S_{ii} = \frac{\partial u_i}{\partial x_i} \quad (2.5)$$

The strain can also be expressed with only six independent elements  $S_1=S_{xx}$ ,  $S_2=S_{yy}$ ,  $S_3=S_{zz}$ ,  $S_4=2S_{yz}$ ,  $S_5=2S_{xz}$ ,  $S_6=2S_{xy}$ , and  $S_{xy}=S_{yx}$ ,  $S_{yz}=S_{zy}$ ,  $S_{xz}=S_{zx}$ .

### 2.2.3 Stiffness

The relationship between the stress and strain is given by Hooke's law:

$$T_{ij} = c_{ijkl}S_{kl} \quad (2.6)$$

where  $c$  is the stiffness. The stiffness matrix puts the generalized Hooke's law for three dimensions in matrix form:

$$\begin{bmatrix} T_1 \\ T_2 \\ T_3 \\ T_4 \\ T_5 \\ T_6 \end{bmatrix} = \begin{bmatrix} c_{11} & c_{12} & c_{13} & c_{14} & c_{15} & c_{16} \\ c_{21} & c_{22} & c_{23} & c_{24} & c_{25} & c_{26} \\ c_{31} & c_{32} & c_{33} & c_{34} & c_{35} & c_{36} \\ c_{41} & c_{42} & c_{43} & c_{44} & c_{45} & c_{46} \\ c_{51} & c_{52} & c_{53} & c_{54} & c_{55} & c_{56} \\ c_{61} & c_{62} & c_{63} & c_{64} & c_{65} & c_{66} \end{bmatrix} \begin{bmatrix} S_1 \\ S_2 \\ S_3 \\ S_4 \\ S_5 \\ S_6 \end{bmatrix} \quad (2.7)$$

### 2.2.4 One-dimensional Approximation

Three-dimensional equations derived from the above expressions can be extremely difficult to solve when the propagation of the acoustic wave is analyzed. Their solutions require numerical techniques and will not be considered here. Instead, a useful and simplifying one-dimensional approximation is assumed when the lateral dimensions are much greater than the thickness dimension. A practical minimum lateral to thickness dimension ratio 50:1 was proposed by Lakin in [65] to fulfill the one-dimensional approximation. Then, the lateral dimensions are approximated by infinite and only the thickness mode of propagation is assumed. When dealing with a one-dimensional geometry, shear and longitudinal waves are treated identically. However, we will be focusing on longitudinal waves, the dominant ones in BAW devices.

The above described physical quantities such as stress, strain and displacement depend only on the thickness dimension. Under the one-dimensional approximation and with the z-axis in the orthogonal coordinates system being the thickness direction, the stress and the strain become  $T_3$  and  $S_3$  respectively and can be expressed as:

$$T = \frac{dF}{dA} \quad (2.8)$$

$$S = \frac{du}{dz} \quad (2.9)$$

where  $F$  is the force applied to a surface of area  $A$ .

Hooke's law can be simplified:

$$T = cS \quad (2.10)$$

where  $c$  is the stiffness component  $c_{33}$ .

## 2.3 Bulk Acoustic Wave Propagation in Non-piezoelectric Slabs

### 2.3.1 Acoustic Wave Equation

Next, the equation for an acoustic wave that propagates through a non-piezoelectric material slab will be presented.

The particle velocity is the time derivative of particle displacement:

$$v = \frac{\partial u}{\partial t} \quad (2.11)$$

Newton's second law states that the net force on a particle is equal to the time rate of change of its linear momentum in an inertial reference frame:

$$F = m \frac{\partial v}{\partial t} \quad (2.12)$$

where  $F$  is the net force applied and  $m$  is the mass of the body. Assuming the particle with volume  $dV$  and surface  $dA$

$$F = \int_{\partial A} T \cdot \hat{\mathbf{n}} dA \quad (2.13)$$

and

$$\int_{\partial A} T \cdot \hat{\mathbf{n}} dA = \int_{\partial V} \rho \frac{\partial^2 u}{\partial t^2} dV \quad (2.14)$$

where  $\rho$  is the density in  $\text{kg}/\text{m}^3$ .

For very small volumes, the integrands of the volume integration are approximately constant

$$\frac{\int T \cdot \hat{\mathbf{n}} dA}{\partial A} = \rho \frac{\partial^2 u}{\partial t^2} \quad (2.15)$$

and when  $dV \rightarrow 0$  the left side of the equation becomes the divergence of  $T$ :

$$\nabla \cdot T = \lim_{dV \rightarrow 0} \frac{\int T \cdot \hat{\mathbf{n}} dA}{dV} \quad (2.16)$$

and writing the divergence for the one-dimensional situation that we are analyzing:

$$\frac{\partial T}{\partial z} = \rho \frac{\partial^2 u}{\partial t^2} \quad (2.17)$$

and combining it with (2.9) and Hooke's law (2.10) the wave equation is obtained

$$\frac{\partial^2 u}{\partial z^2} = \frac{\rho}{c} \frac{\partial^2 u}{\partial t^2} \quad (2.18)$$

for the sinusoidal steady-state condition:

$$\frac{\partial^2 u}{\partial z^2} - \frac{\rho}{c} \omega^2 u = 0 \quad (2.19)$$

In a similar way, combining (2.9) and (2.10) into (2.17) for the sinusoidal steady-state condition, the following can be obtained:

$$\frac{\partial^2 T}{\partial z^2} - \frac{\rho}{c} \omega^2 T = 0 \quad (2.20)$$

It can be seen that (2.19) and (2.20) are analogous to wave propagation equations on a transmission line where electromagnetic fields are propagated expressed by currents and voltages. The transmission line equations can be found in [23]:

$$\frac{\partial^2 V}{\partial z^2} - \gamma^2 V = 0 \quad (2.21)$$

$$\frac{\partial^2 I}{\partial z^2} - \gamma^2 I = 0 \quad (2.22)$$

where  $V$  is the voltage,  $I$  the electric current and  $\gamma$  the propagation constant. The propagation constant in the acoustic wave equation  $k$  is given by:

$$k = \sqrt{\frac{\rho}{c}}\omega \quad (2.23)$$

The general definition of the wave equation depending on the frequency and the phase velocity is:

$$k = \frac{\omega}{v_p} \quad (2.24)$$

Then, the acoustic phase velocity of the wave is given by

$$v_p = \sqrt{\frac{c}{\rho}} \quad (2.25)$$

and the acoustic impedance of the medium

$$Z_m = \sqrt{\rho c} \quad (2.26)$$

the units of impedance are  $\text{kg}/(\text{s}\cdot\text{m}^2)$ .

### 2.3.2 Acoustic Transmission Line Model

The particle displacement is obtained from (2.19) and it can be written as follows suppressing the time variation:

$$u(z) = u^+ e^{-jkz} + u^- e^{+jkz} \quad (2.27)$$

where the  $e^{-jkz}$  term represents wave propagation in the  $+z$  direction and the  $e^{+jkz}$  term in the  $-z$  direction. The coefficients  $u^+$  and  $u^-$  depend on the impedance mismatch at the boundaries of the considered slab.

A slab of thickness  $d$  bounded by the planes  $z=z_1$  and  $z=z_2$  is considered. The particle velocities at the boundaries can be derived from the time derivative of (2.27) at  $z=z_1$  and  $z=z_2$ :

$$\frac{\partial u_1}{\partial t} = v_1 = j\omega \left( u^+ e^{-jkz_1} + u^- e^{+jkz_1} \right) \quad (2.28)$$

$$\frac{\partial u_2}{\partial t} = v_2 = j\omega \left( u^+ e^{-jkz_2} + u^- e^{jkz_2} \right) \quad (2.29)$$

Next, coefficients  $u^+$  and  $u^-$  will be solved. If (2.28) is multiplied by  $e^{jkz_2}$  we obtain:

$$j\omega u^+ e^{jkd} = v_1 e^{jkz_2} - j\omega u^- e^{jkz_1} e^{jkz_2} \quad (2.30)$$

And (2.29) is multiplied by  $e^{-jkz_2}$  obtaining:

$$j\omega u^- = v_2 e^{-jkz_2} - j\omega u^+ e^{-2jkz_2} \quad (2.31)$$

where  $d = z_2 - z_1$ . Then,  $u^+$  and  $u^-$  are obtained combining (2.30) and (2.31):

$$j\omega u^+ = \frac{v_1 e^{jkz_2} - v_2 e^{jkz_1}}{2j \sin(kd)} \quad (2.32)$$

$$j\omega u^- = \frac{v_2 e^{-jkz_1} - v_1 e^{-jkz_2}}{2j \sin(kd)} \quad (2.33)$$

From (2.9) and (2.10), the force  $F$  applied to an area  $A$  can be written as:

$$F = AT = Ac \frac{\partial u}{\partial z} \quad (2.34)$$

Replacing the space derivative of the particle displacement (2.27) in (2.34):

$$F = jkcA \left( u^+ e^{-jkz} - u^- e^{jkz} \right) \quad (2.35)$$

The impedance of the plate can be expressed as the product of the impedance of the medium and the area, and using (2.24), (2.25) and (2.26) it can be expressed as:

$$Z = Z_m A = \frac{ckA}{\omega} \quad (2.36)$$

Then, using (2.36) in (2.35):

$$F = Z \left( j\omega u^+ e^{-jkz} - j\omega u^- e^{jkz} \right) \quad (2.37)$$

and replacing  $j\omega u^+$  and  $j\omega u^-$  from (2.32) and (2.33) at  $z_1$ :

$$F_1 = Z \left( e^{-jkz_1} \left( \frac{v_1 e^{jkz_2} - v_2 e^{jkz_1}}{2j \sin(kd)} \right) - e^{jkz_1} \left( \frac{v_2 e^{-jkz_1} - v_1 e^{jkz_2}}{2j \sin(kd)} \right) \right) \quad (2.38)$$

that can be simplified as follows:

$$F_1 = Z \left( \frac{v_1}{j \tan(kd)} - \frac{v_2}{j \sin(kd)} \right) \quad (2.39)$$

and replacing  $j\omega u^+$  and  $j\omega u^-$  from (2.32) and (2.33) at  $z_2$  in (2.37):

$$F_2 = Z \left( \frac{v_1}{j \sin(kd)} - \frac{v_2}{j \tan(kd)} \right) \quad (2.40)$$

and the forces at the boundaries can be rewritten as:

$$F_1 = \frac{Z}{j \sin(kd)} (v_1 - v_2) + jZ \tan\left(\frac{kd}{2}\right) v_1 \quad (2.41)$$

$$F_2 = \frac{Z}{j \sin(kd)} (v_1 - v_2) - jZ \tan\left(\frac{kd}{2}\right) v_2 \quad (2.42)$$

where the next trigonometric identity has been used:

$$\tan\left(\frac{kd}{2}\right) = \frac{1}{\tan(kd)} - \frac{1}{\sin(kd)} \quad (2.43)$$

The following analogy is considered:

force  $F \longrightarrow$  voltage  $V$

particle velocity  $v \longrightarrow$  current  $I$

Finally, Fig. 2.3 shows the equivalent electrical circuit for the finite thickness slab. It can be seen as an acoustic transmission line with acoustic impedance and an acoustic constant of propagation. The electrical circuit fulfills (2.41) and (2.42); therefore it models the behavior of an acoustic slab by means of a T of impedances or a transmission line model.

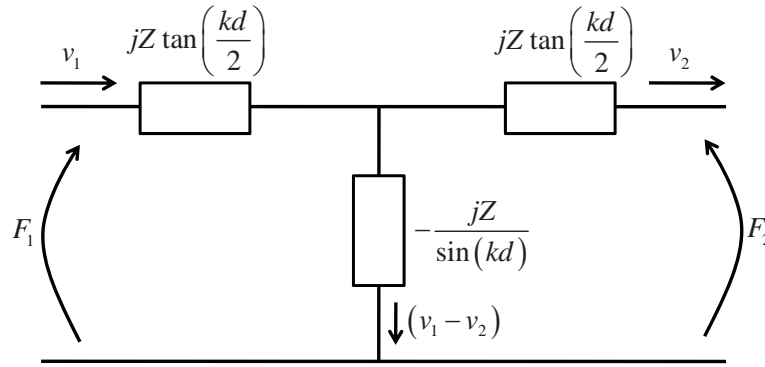


Figure 2.3: Transmission line model of a non-piezoelectric slab.

## 2.4 Piezoelectric Plates

### 2.4.1 Constitutive Relations

In the case of piezoelectric materials, the coupling between the electric and acoustic fields is taken into account by means of the piezoelectric constitutive relations [61]

$$T = c^E S - eE \quad (2.44)$$

$$D = eS + \varepsilon^S E \quad (2.45)$$

where  $E$  is the electric field,  $D$  the electric displacement,  $c^E$  is the stiffness measured at constant electric field,  $\varepsilon^S$  is the permittivity measured at constant strain and  $e$  is the piezoelectric constant with units C/m<sup>2</sup>. The piezoelectric constant modifies Hooke's law in (2.44) to include the emergence of stress associated with the presence of an external electric field due to the direct piezoelectric effect. In (2.45), the piezoelectric constant includes the inverse piezoelectric effect creating electric displacement when a strain is produced in the material.

From (2.44) and (2.45)

$$T = c^E \left( 1 + \frac{e^2}{c^E \varepsilon^S} \right) S - \frac{e}{\varepsilon^S} D = c^D S - \frac{e}{\varepsilon^S} D \quad (2.46)$$

where

$$c^D = c^E \left( 1 + \frac{e^2}{c^E \varepsilon S} \right) \quad (2.47)$$

is known as the piezoelectrically stiffened elastic constant because the piezoelectric effect is stiffening the material  $c^D > c^E$ . The acoustic velocity in a piezoelectric material is then

$$v^D = \sqrt{\frac{c^D}{\rho}} = \sqrt{\frac{c^E}{\rho}} \sqrt{1 + K^2} \quad (2.48)$$

where

$$K^2 = \frac{e^2}{c^E \varepsilon S} \quad (2.49)$$

is known as the electromechanical coupling factor and is a measure of how efficiently the piezoelectric material is converting energy between the electric and acoustic domains. Another parameter that is often used to measure this energy conversion efficiency is the piezoelectric coupling constant [60].

$$k_t^2 = \frac{e^2}{c^D \varepsilon S} = \frac{K^2}{K^2 + 1} \quad (2.50)$$

### 2.4.2 Mason Model

If the piezoelectric is dielectric, the current can be expressed as:

$$I = JA = \frac{\partial D}{\partial t} A = j\omega DA \quad (2.51)$$

where  $J$  is the current density.

The electric field can be expressed from (2.45) and (2.9) as:

$$E = \frac{D}{\varepsilon S} - \frac{e}{\varepsilon S} \frac{\partial u}{\partial z} \quad (2.52)$$

Therefore, the total electric field is composed of an external electric field and an internally generated electrical field generated by the piezoelectric effect.

The voltage between  $z = z_1$  and  $z = z_2$  is obtained integrating the electric field:

$$V = \int_{z_1}^{z_2} Edz = \frac{Dd}{\epsilon S} - h(u(z_2) - u(z_1)) \quad (2.53)$$

where

$$h = \frac{e}{\epsilon S} \quad (2.54)$$

using  $v = j\omega u$  and (2.51) in (2.53):

$$V = \frac{Id}{j\omega A \epsilon S} + \frac{h}{j\omega} (v_1 - v_2) \quad (2.55)$$

and solving for  $I$ :

$$I = j\omega C_0 V + hC_0 (v_1 - v_2) \quad (2.56)$$

The current is composed of a capacitance contribution and a contribution of the acoustic energy conversion coming from the piezoelectric effect.

If (2.34) is modified according to (2.46) and (2.51):

$$F = TA = c^D SA - \frac{eD}{\epsilon S} A = c^D SA + \frac{h}{j\omega} I \quad (2.57)$$

the left term of (2.57) corresponds to (2.41) and (2.42) at the boundaries  $z = z_1$  and  $z = z_2$ . Therefore, for the piezoelectric slab, the forces at the boundaries are:

$$F_1 = \frac{Z}{j \sin(kd)} (v_1 - v_2) + jZ \tan\left(\frac{kd}{2}\right) v_1 + \frac{h}{j\omega} I \quad (2.58)$$

$$F_2 = \frac{Z}{j \sin(kd)} (v_1 - v_2) - jZ \tan\left(\frac{kd}{2}\right) v_2 + \frac{h}{j\omega} I \quad (2.59)$$

It can be seen that (2.56), (2.58) and (2.59) occur in the Mason model of Fig. 2.4. The Mason model is a complete electrical circuit model for a piezoelectric slab; it is named after Warren Mason, who performed much of the pioneering work in crystal acoustics. The Mason model is composed of:

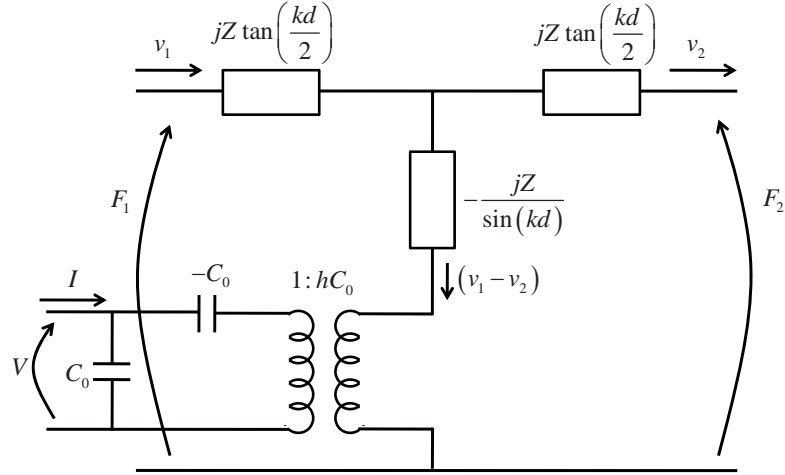


**Figure 2.4:** Mason model of a piezoelectric slab.

- a shunt capacitor  $C_0$  modeling the capacitive effect between the boundaries of the plate.
- a transformer and a negative series capacitor  $-C_0$  representing the electro-acoustic conversion in the piezoelectric material. On one side, the acoustic domain takes place with an acoustic current and on the other the electric domain with an electric current.
- a non-piezoelectric transmission line modeling the mechanical wave propagation across the plate.

The voltage on the right side of the transformer is obtained from (2.58) or (2.59):

$$V_{t,right} = \frac{h}{j\omega} I \quad (2.60)$$

The transformer ratio is obtained from (2.56):

$$t = hC_0 \quad (2.61)$$

Therefore, the voltage on the left side of the transformer is:

$$V_{t,left} = \frac{I}{j\omega C_0} \quad (2.62)$$

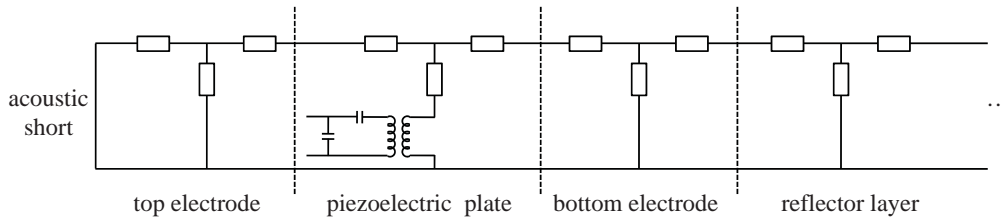


**Figure 2.5:** Mason model and transmission line models combined to represent a multilayered model.

The series negative capacitor on the electric side enables fulfilling (2.62). The reactance of the negative capacitor varies inversely like the frequency but its magnitude has a positive value like an inductor.

The transmission line model and the Mason model for non-piezoelectric and piezoelectric slabs have been presented respectively. The two models are of huge importance in the BAW technology community and also for this work. Their ability to gather the mechanical and piezoelectric behavior in simple models composed of transmission lines and lumped elements enables a practical one-dimensional analysis of BAW devices and their implementation in CAD tools.

As presented in the introduction of this work, in a practical case, a BAW resonator is composed of multiple layers including a piezoelectric plate, metallic electrodes, Bragg reflector... The simulation of the whole stack of layers is carried out by means of cascading the acoustic transmission lines as shown in Fig. 2.5. Devices with multiple acoustic ports such as SCF or CRF can also be constructed with the Mason model adding conveniently placed sections. The effects of the acoustic losses can be included by means of complex propagation constants.

## 2.5 Closed-form Expression for the Input Impedance of a BAW Resonator

In this section, the input impedance of a piezoelectric slab acoustically loaded with acoustic loads  $Z_1$  and  $Z_2$  at the boundaries  $z = z_1$  and  $z = z_2$  respectively, as shown in Fig. 2.6, will be obtained. Forces  $F_1 = Z_1 v_1$  and  $F_2 = -Z_2 v_2$  are considered at the boundaries.

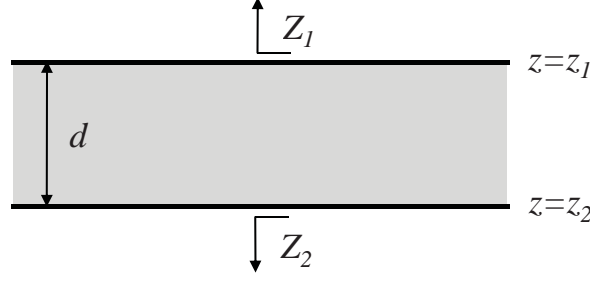


**Figure 2.6:** Piezoelectric slab loaded with  $Z_1$  and  $Z_2$ .

Then, (2.58), (2.59) and (2.56) can be written as follows:

$$Z_1 x = Z \left( \frac{x}{j \tan(kd)} - \frac{y}{j \sin(kd)} \right) + \frac{h}{j\omega} \quad (2.63)$$

$$-Z_2 y = Z \left( \frac{x}{j \sin(kd)} - \frac{y}{j \tan(kd)} \right) + \frac{h}{j\omega} \quad (2.64)$$

$$Z_{in} = \frac{V}{I} = \frac{1}{j\omega C_0} + \frac{h}{j\omega} (x - y) \quad (2.65)$$

where  $x = v_1/I$  and  $y = v_2/I$ .

The electrical input impedance of the slab  $Z_{in}$  is obtained solving the system formed by (2.63), (2.64) and (2.65):

$$Z_{in} = \frac{1}{j\omega C_0} \left( 1 - k_t^2 \frac{\text{tg}(\phi)}{\phi} \frac{\left( \frac{Z_R + Z_L}{Z_p} \right) \cos^2(\phi) + j \sin(2\phi)}{\left( \frac{Z_R + Z_L}{Z_p} \right) \cos(2\phi) + j \left( 1 + \frac{Z_R Z_L}{Z_p^2} \right) \sin(2\phi)} \right) \quad (2.66)$$

where  $\phi = kd/2$ .  $Z_1$  and  $Z_2$  can be calculated recursively by means of the input impedance equation of a transmission line loaded with a known impedance, starting with the outermost layer and moving towards the layer closest to the piezoelectric plate.

If a resonator with infinitesimal electrodes is assumed and  $Z_1 = Z_2 = 0$ , (2.66) is simplified:

$$Z_{in} = \frac{1}{j\omega C_0} \left( 1 - k_t^2 \frac{\tan(\phi)}{\phi} \right) \quad (2.67)$$

the maximum value of  $Z_{in}$  is reached when  $kd/2 = \pi/2$ , taking into account the fundamental mode, which is produced at the anti-resonance frequency:

$$f_a = \frac{v_p}{2d} \quad (2.68)$$

The minimum value of  $Z_{in}$  is reached when  $1 = k_t^2 \tan(\phi)/\phi$  which is produced at the resonance frequency,  $f_r$ .

the distance between the two resonances depends on the piezoelectric coupling constant as anticipated in the introduction:

$$k_t^2 = \frac{\pi f_r}{2 f_p} \frac{1}{\tan\left(\frac{\pi f_r}{2 f_p}\right)} \quad (2.69)$$

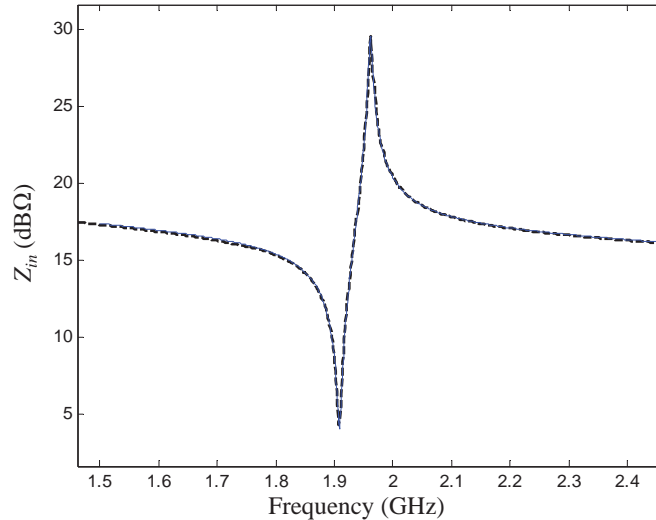
When a practical BAW resonator is considered, it presents multiple additional layers including non-infinitesimal electrodes and the distance between the two resonances in the practical case depends on the effective piezoelectric coupling,  $k_{eff}^2$ , constant which has a different value from  $k_t^2$ . While  $k_t^2$  is a parameter of the piezoelectric material,  $k_{eff}^2$  depends on the whole resonator stack and its boundary conditions.

Fig. 2.7 shows the measure of the electrical input impedance of a BAW-SMR resonator provided by Triquint Semiconductor which is composed of multiple layers with the input impedance calculated using the Mason model for the piezoelectric plate and the transmission line model for the non-piezoelectric plates. The model response shows good agreement with the measure throughout the entire fundamental resonance range of frequencies.

## 2.6 Bragg Reflectors

### 2.6.1 Quarter-wave Reflector

The SMR concept comes from the field of optics in which an optic reflector is implemented and is known as the Bragg mirror or reflector. In thin film SMR technology, the basic Bragg mirror is a structure that consists of an alternating high and low acoustic impedance sequence of layers of two different materials. The Bragg mirror can be straightforwardly analyzed by means of the transmission line models presented in section 2.3 and section 2.4.

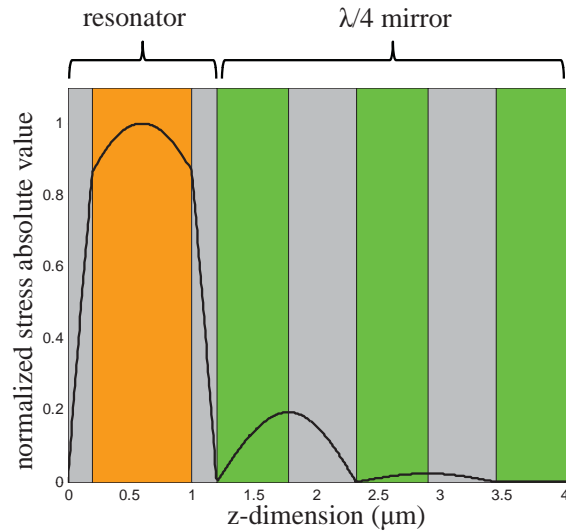


**Figure 2.7:** Electrical input impedance of a measured BAW-SMR resonator (dashed line) and the corresponding Mason model (continuous line)

The initially used configuration was composed of a quarter-wave mirror, where each layer thickness corresponds to one quarter of the wavelength for which the mirror is designed. Several SMR designs following this approach can be found in [66], [67] and [68].

The principle of operation can be understood as follows. Each interface between the two materials contributes a reflection. For the design wavelength, the acoustic path length difference between reflections from subsequent interfaces is half the wavelength; in addition, the reflection coefficients for the interfaces have alternating signs. Therefore, all reflected components from the interfaces interfere constructively, which results in a strong reflection. The reflectivity achieved is determined by the number of layer pairs and by the acoustic impedance ratio between the layer materials.

Fig. 2.8 shows a SMR that has been designed in this work with a Bragg mirror composed of  $\lambda/4$  layers at a design frequency of 2.4 GHz. The reflector is composed of SiO<sub>2</sub>/W/SiO<sub>2</sub>/W/SiO<sub>2</sub> and the resonator of W/AlN/W. The properties of the materials can be found in Appendix A. The stress distribution along the propagation direction shows good confinement of the acoustic wave inside the resonator layers because of the good reflectivity of the mirror. The acoustic wave vanishes as it travels to the substrate presenting a slight longitudinal wave leakage.



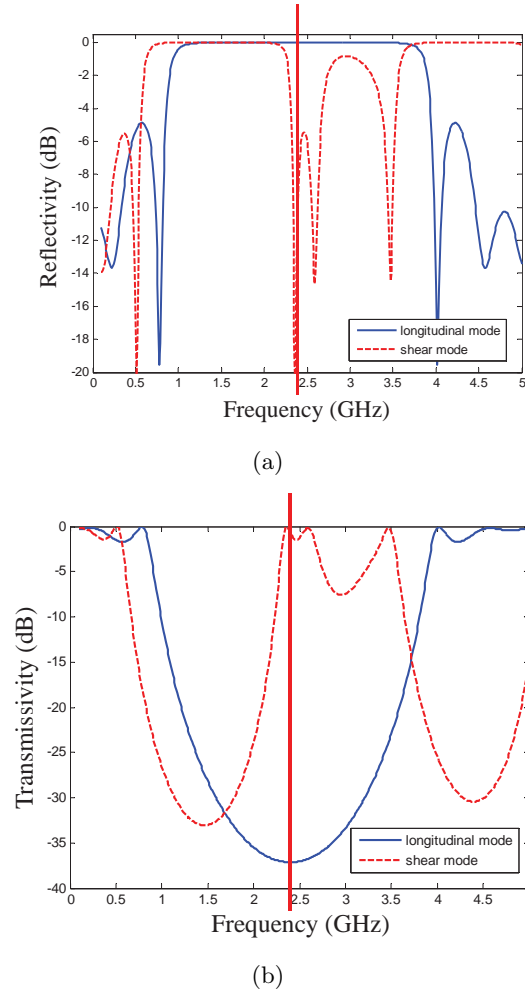
**Figure 2.8:** BAW resonator on top of a Bragg mirror composed of  $\lambda/4$  layers and the absolute value of the normalized stress in each layer at the operation frequency  $f_0=2.4$  GHz.

Fig. 2.9(a) and Fig. 2.9(b) show the longitudinal mode reflectivity and transmissivity of the reflector respectively. It presents the minimum level of transmissivity at the design frequency where it reaches -37.1 dB. The reflectivity is high over some bandwidth, depending on the acoustic impedance contrast of the materials used and on the number of layers of the reflector.

## 2.6.2 Shear Wave Leakage

SMRs were initially designed following the quarter-wave configuration which only takes into account the longitudinal mode of propagation. That configuration provides the best confinement of the longitudinal wave for a set of mirror layers. However, modes other than the longitudinal wave are not taken into account at the time of containing the mechanic energy inside the resonator structure. In [20], the shear wave leaks across the reflector structure are presented as an important loss mechanism that significantly reduces the  $Q$  factor of a SMR. Shear waves can be created by the reflection or refraction of longitudinal waves at non-perpendicular angles of incidence to a material interface.

The shear wave velocity of typical materials is about half of the longitudinal wave velocity. Therefore, for the design frequency of the mirror the set of layers of the



**Figure 2.9:** (a) Reflectivity and (b) transmissivity of the SMR with quarter-wave layers.

reflector are approximately  $\lambda/2$  for the shear mode of propagation and the reflector becomes a stack with good transmissivity of the shear wave to the substrate. Those shear wave leaks reduce the amount of contained energy inside the resonator at the resonance.

Fig. 2.9(a) and Fig. 2.9(b) also show the shear mode reflectivity and transmissivity of the quarter-wave reflector respectively. The transmissivity at the design frequency is -0.7 dB which proves the shear wave leaks.

A way to calculate the effects of the shear losses on the overall  $Q$  of the resonator

was proposed in [20]:

$$\frac{1}{Q} = \frac{\Delta E_{tot}}{E_{tot}} = \left( \frac{E_{long}}{E_{tot}} \right) \frac{1}{Q_{long}} + \left( \frac{E_{shear}}{E_{tot}} \right) \frac{1}{Q_{shear}} \quad (2.70)$$

where  $Q_{long}$  and  $Q_{shear}$  are the individual  $Q$  values for the longitudinal and shear loss processes respectively.  $E_{tot}$  is the total energy composed of the longitudinal and shear wave components  $E_{long}$  and  $E_{shear}$  respectively.  $\Delta E_{tot}$  are the total losses in the system and are assumed to be composed of longitudinal and shear wave losses through the mirror.

Calculating a possible case can offer an idea of how dramatic the  $Q$  drop can be when there are shear leaks. A distribution of 99% of the energy in the longitudinal mode and 1% converted to shear waves is assumed. A resonator with a value of  $Q_{long}=10000$  can seem to be a very good resonator if only the longitudinal mode is considered during simulations. However, if the shear losses are included with  $Q_{shear}=10$ , the quality factor of the resonator drops to  $Q=910$ .

The shear wave loss mechanism explains the fact that calculations of the acoustic reflectance of a standard quarter-wavelength mirror stack leads to theoretical  $Q$  factors well above 10000 while experimental SMR devices with this type of quarter-wavelength mirror show values of typically well below 1000. Initially, this discrepancy was explained by lateral waves which leaked out of the resonator active area and mechanical losses. However, the shear wave loss mechanism is much more important than those former explanations.

### 2.6.3 Optimized Reflectors for Longitudinal and Shear Modes

The shear wave leaks can be reduced by means of a proper design of the reflector layers. The thicknesses of the reflector layers can be found by means of an optimization procedure on the transmission of the longitudinal and shear waves through the mirror stack. The thicknesses are the set of variables to optimize and the goal is to minimize the transmissivity of both modes at the design frequency. The weight assigned to the transmissivity of each mode in the optimization function can be adjusted depending on the assumption on the distribution of energy between the two modes of propagation.

After applying the optimization routine, the set of mirror layers has been modified in this work regarding the original situation presenting the thicknesses  $[0.171/0.830/0.601/0.830/0.942] \times \lambda/4$ , where  $\lambda$  is the wavelength of the longitudinal

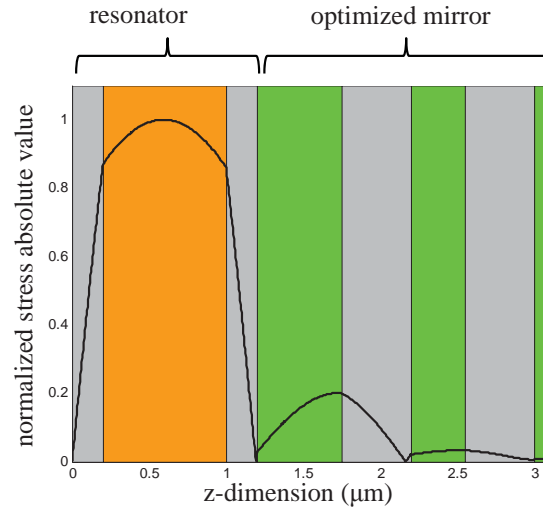
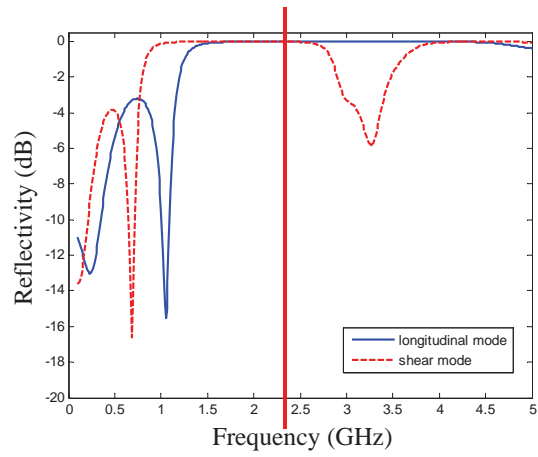


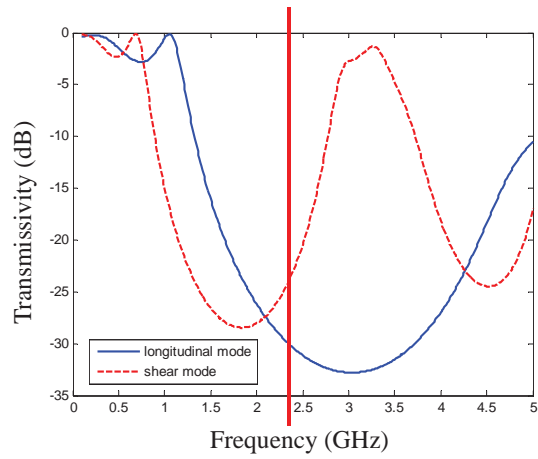
**Figure 2.10:** BAW resonator on top of a Bragg mirror composed of optimized layers to present good reflectivity in both the longitudinal and shear mode and the absolute value of the normalized stress in each layer at the operation frequency  $f_0=2.4$  GHz.

mode at the design frequency and the layers are arranged from left to right ascending from the substrate to the resonator. Fig. 2.10 shows the SMR with an optimized Bragg mirror and the stress distribution in the longitudinal mode along the propagation direction.

Fig. 2.11(a) and Fig. 2.11(b) show the simulated longitudinal and shear mode reflectivity and transmissivity of the optimized reflector respectively. The value of the transmissivity of the longitudinal mode at the operating frequency is -30.5 dB. Thus, the reflectivity is slightly worse than the reference quarter-wave case. However, the transmissivity of the shear mode has considerably improved to a value of -23 dB. The longitudinal mode reflectivity has been sacrificed a bit in order to better trap the shear wave in the resonator.



(a)



(b)

**Figure 2.11:** (a) Reflectivity and (b) transmissivity of the SMR with layers thicknesses optimized to offer good reflector behavior in both the longitudinal and the shear mode.

## 2.7 Summary

In this chapter, the basic physics of BAW devices have been reviewed. The set of variables and laws that govern the acoustic wave propagation and the piezoelectric effects have been stated. Two types of materials have been considered: non-piezoelectric and piezoelectric materials. The assumption of one-dimensional propagation in the thin film layers has been taken into account which is valid in typical BAW technology devices and simplifies the analysis.

First, the acoustic wave propagation in a non-piezoelectric slab was analyzed. A transmission line can accurately model the behavior of the slab. The acoustic transmission line model is analog to the well-known electrical transmission line model but using acoustic impedance and propagation constant instead of electrical.

Then, the analysis was extended to include piezoelectric slabs which are governed by the constitutive relations. The piezoelectric slab can be considered as a non-piezoelectric slab modeled by means of the acoustic transmission line with the addition of a circuit that includes the piezoelectric transduction between the electric and the acoustic fields. The resulting model is the Mason model.

The transmission line model and the Mason model were combined to analyze BAW technology devices in a one-dimensional approach. These models have been used throughout this work and are of great importance in the analysis and design of BAW filters. The general expression for the electrical input impedance of BAW resonators was derived and described.

Finally, the Bragg reflector of SMRs was analyzed by means of the above presented propagation relationships. The longitudinal and the shear mode of propagation were considered. Both of them can be analyzed using the one-dimensional approach and the corresponding acoustic velocities of each mode. The way in which the shear mode can be an important mechanism of losses in quarter-wavelength mirrors was demonstrated as well as how the mirror losses can be improved by means of an optimized design that takes into account both modes of propagation.

## Chapter 3

# Equivalent Electrical Models for Acoustically Coupled Resonators

The aim of this work is to synthesize BAW filters, in particular Coupled Resonator Filters (CRFs). BAW filters formed by acoustically coupled BAW resonators present a transmission response where the signal path is affected in both the electrical and the acoustic fields and also by the piezoelectric transduction between them. Considering the thickness extensional mode of propagation, the Mason model presented in the previous chapter can fully describe the effects that take place in every thin layer that makes up the structure. It is unquestionable that the Mason model is a very valuable structure analysis tool and it has been widely validated for several decades. However, the resulting network complexity that arises when the Mason model is applied to complex multilayered structures such as CRFs does not facilitate the linking of the physical model with filter design systematic tools.

In [45], Lakin proposes a lumped equivalent electrical circuit model for the SCF. It is developed from the Mason model for single mode plane wave propagation in a piezoelectric plate. This model offers the advantage of evaluating the device behavior combining the electrical and acoustical fields in a purely electrical circuit. More importantly, the model provides a valuable tool for use with standard filter synthesis techniques as shown in [69].

The purpose of this chapter is to provide a set of equivalent electrical models for a CRF and its variants in order to link the physical device with filter synthesis procedures that will be developed in the next chapters. The models will be used as tools that gather

the behavior of the devices and also channel the circuit into device design techniques.

This chapter extends the contribution of [45] proposing a novel electrical model for the Coupled Resonator Filter, the natural evolution of the SCF, where a set of coupling layers allows the existence of 2 effective resonators instead of one as with SCFs. Then, a second evolution on the CRF which includes additional non-transducer resonators is also electrically modeled. Furthermore, a CRF composed of resonators with different active areas is considered and a general approach to analyze asymmetrical structures is presented.

Finally, a set of closed-form expressions for the design of the CRF coupling layers will be presented. The expressions will relate the geometry of the layers with the value of the inverter that is part of the CRF models. A new coupling mechanism approach consisting of a single very low acoustic impedance layer will be assessed as well.

### 3.1 CRF Equivalent Electrical Model

The most basic CRF is composed of two BAW resonators piled on top of each other and separated by means of a set of coupling layers as shown in Fig. 3.1. The interaction between the resonators takes place in the acoustic plane by means of the physical contact between layers which allows the propagation of the longitudinal wave across the structure.

A set of assumptions can be taken to simplify and clarify the steps to obtain an electrical equivalent model for the CRF without loss of generality:

- A symmetrical structure is considered with identical top and bottom resonators in terms of material parameters and geometry. The modelling of the structure can be extended to asymmetrical structures as shown in section 3.3, where different size resonators are taken into account.
- The electrode thickness of the resonators is considered infinitesimal and the resonator is approximated to a pure piezoelectric plate. This assumption facilitates the illustration of a clear process to obtain the CRF model with neat networks and sequential transformations. Moreover, a set of closed-form expressions that relate the circuit model to the physical parameters in terms of geometry and material parameters are obtained. Those relationships link the filtering behavior

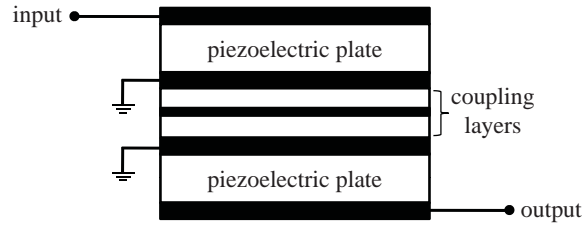


**Figure 3.1:** Coupled resonator filter cross section.

with the structure of the device. The resulting model is completely general and it could be derived taking into account an elevated number of layers for each resonator including complex electrodes. However, when multiple layers for the resonators are taken into account, the networks become cumbersome and the closed-form expressions are too long and recursive. For this reason, the use of numerical methods is more convenient to find the values of the elements of the proposed model when complex sets of layers are considered in such a way that the model behavior fits the CRF behavior.

- The set of coupling layers is modeled by means of an impedance inverter. The goal of the coupling layers is to control the degree of acoustic coupling between resonators, and this function can be modeled by means of an impedance inverter which performs this role in a bandpass filter.
- The boundaries at the outer faces of the resonators are considered perfect acoustic short-circuits. The upper boundary is generally air and its low acoustic impedance is quite close to an acoustic short-circuit. The lower boundary can be air or a Bragg reflector, depending on the manufacturing approach, and has also been approximated to a short-circuit.

### 3.1.1 Definitions and Network Transformations

In order to model the CRF, the Mason model is applied to each piezoelectric resonator and the network is organized as shown in Fig. 3.2(a). The input and output ports of the equivalent circuit are the electric ports of each resonator.

The values of the impedances are:

$$Z_1 = jZ_p \tan\left(\frac{\theta}{2}\right) \quad (3.1)$$

$$Z_2 = -jZ_p \operatorname{cosec}(\theta) \quad (3.2)$$

where  $\theta = kd$  is the acoustic length,  $k$  is the acoustic wave propagation constant and  $d$  is the thickness of the piezoelectric plate. The mass loading effect caused by the electrode thickness is omitted for the sake of simplicity and so, the piezoelectric thickness is:

$$d = v_p/2f_a \quad (3.3)$$

where  $v_p$  is the acoustic wave propagation velocity of the piezoelectric and  $f_a$  is the anti-resonance frequency at which the input electrical impedance of a single resonator reaches its maximum value.

The characteristic impedance of the equivalent acoustic transmission line,  $Z_p$ , is the acoustic impedance, and depends on both the area  $A$  and the acoustic impedance per unit area of the piezoelectric material ( $Z_{0p}$ ).

The piezoelectric effect is included in the model by the impedance transformer, representing the conversion of electric energy to acoustic energy, and the negative capacitance. In turn, the dielectric effect is modeled by the shunt capacitor at the input of the electric port. The transformer ratio is given by:

$$t = \frac{e}{\varepsilon} C_0 \quad (3.4)$$

where  $e$  (C/m<sup>2</sup>) is the piezoelectric constant,  $\varepsilon$  is the material dielectric permittivity and the value of the static capacitor is given by:

$$C_0 = \frac{\varepsilon A}{d} \quad (3.5)$$

The two resonators interact by means of the interconnection of one of their respective acoustic ports. The remaining acoustic port of each resonator is grounded because a perfect acoustic short-circuit is assumed at the outer boundaries of the device. Unlike an SCF, in a CRF the link takes place by means of the coupling layers modeled with an impedance inverter of value  $K_{coupling}$ .

Since the two resonators are assumed to be identical, the technological parameters are the same for both, as well as the circuit elements of the model, resulting in a symmetrical topology.

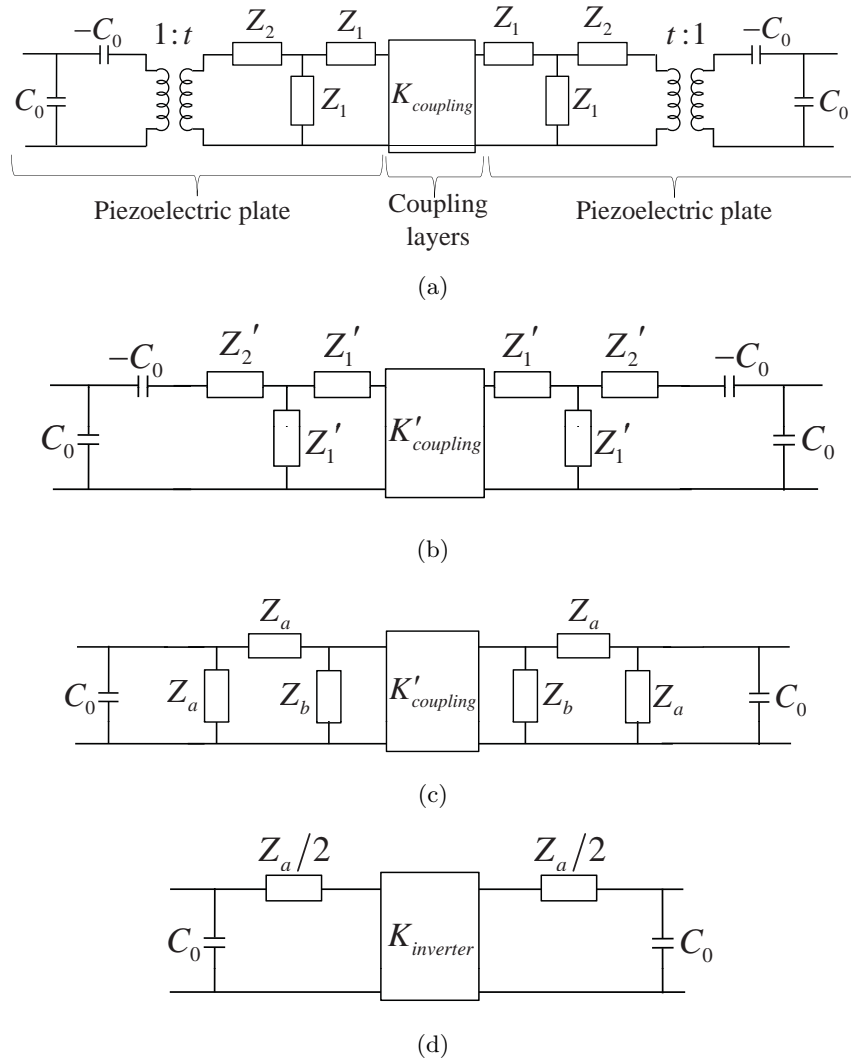


**Figure 3.2:** Set of network transformations to obtain the CRF electrical equivalent model. (a) Original network where the Mason model is applied to each piezoelectric plate. (b) Absorption of the transformers. (c) T to II transformation. (d) Network simplification around the anti-resonance

In order to simplify the network the impedance transformers are shifted to the same node circuit, so that the effect of the transformers is mutually cancelled out due to symmetry, obtaining the network shown in Fig. 3.2(b). The circuit elements must be modified according to the transformation rules caused by the displacement of the transformers. The values of the impedances that compose the acoustic transmission line and the inverter are scaled in the form:

$$Z_1' = j \frac{Z_p}{t^2} \tan\left(\frac{\theta}{2}\right) \quad (3.6)$$

$$Z_2' = -j \frac{Z_p}{t^2} \operatorname{cosec}(\theta) \quad (3.7)$$

$$K'_{coupling} = \frac{K_{coupling}}{t^2} \quad (3.8)$$

The network in Fig. 3.2(b) can be reduced by network analysis applying a T to  $\Pi$  transformation and obtaining the Fig. 3.2(c) network, where:

$$Z_a = Z_1' + 2Z_2' - \frac{2}{j\omega C_0} \quad (3.9)$$

$$Z_b = \frac{Z_1' Z_a}{Z_2' - 1/j\omega C_{01}} \quad (3.10)$$

For the sake of simplicity, it is interesting to show a compact relation between (3.9) and (3.10):

$$Z_b = Z_1' \left( 2 + \frac{Z_b}{Z_a} \right) \quad (3.11)$$

Now, if we suppose that the device operates in a frequency range around the anti-resonance frequency,  $f_a$ , the impedance  $Z_1'$  reaches a very high value and we can apply an interesting approximation for  $Z_b$  to (3.11):

$$Z_b = 2 \left( \frac{1}{Z_1'} - \frac{1}{Z_a} \right)^{-1} \Bigg|_{(Z_1')^{-1} \rightarrow 0 @ f_a} \cong -2Z_a \quad (3.12)$$

By means of this approximation, the behavior of the Fig. 3.2(c) and Fig. 3.2(d) networks can be easily matched calculating the resulting ABCD matrixes of the elements between the shunt capacitors in both networks and equating their results:

$$\begin{aligned}
 & \begin{bmatrix} 1 & 0 \\ Y_a & 1 \end{bmatrix} \begin{bmatrix} 1 & Z_a \\ 0 & 1 \end{bmatrix} \begin{bmatrix} 1 & 0 \\ -Y_a/2 & 1 \end{bmatrix} \begin{bmatrix} 0 & jK'_{coupling} \\ j(K'_{coupling})^{-1} & 1 \end{bmatrix} \\
 & \begin{bmatrix} 1 & 0 \\ -Y_a/2 & 1 \end{bmatrix} \begin{bmatrix} 1 & Z_a \\ 0 & 1 \end{bmatrix} \begin{bmatrix} 1 & 0 \\ Y_a & 1 \end{bmatrix} = \begin{bmatrix} j\frac{2Z_a}{K'_{coupling}} & j\frac{K'^2_{coupling} + 4Z_a^2}{4K'_{coupling}} \\ j\frac{4}{K'_{coupling}} & j\frac{2Z_a}{K'_{coupling}} \end{bmatrix} \quad (3.13)
 \end{aligned}$$

$$\begin{aligned}
 & \begin{bmatrix} 1 & Z_a/2 \\ 0 & 1 \end{bmatrix} \begin{bmatrix} 0 & jK_{inverter} \\ j(K_{inverter})^{-1} & 0 \end{bmatrix} \begin{bmatrix} 1 & Z_a/2 \\ 0 & 1 \end{bmatrix} \\
 & = \begin{bmatrix} j\frac{Z_a}{2K_{inverter}} & j\frac{4K_{inverter}^2 + Z_a^2}{4K_{inverter}} \\ j\frac{1}{K_{inverter}} & j\frac{Z_a}{2K_{inverter}} \end{bmatrix} \quad (3.14)
 \end{aligned}$$

The value of the central inverter,  $K_{inverter}$ , models the degree of electrical coupling between resonators, and it is directly related to the design parameters of the CRF structure: the degree of acoustic coupling that implements the set of coupling layers and the transformer ratio.

$$K_{inverter} = \frac{K'_{coupling}}{4} = \frac{K_{coupling}}{4t^2} \quad (3.15)$$

Finally, the impedance  $Z_a$ , as we will analyze in the next section, presents equivalent behavior to a series inductance-capacitance (LC) resonator near the anti-resonance frequency. The elements of the LC resonator will be determined by the technological parameters of the material and the geometry of the piezoelectric resonator.

Furthermore, it is interesting to note that by means of the procedure followed we can arrive at the same result for an SCF as that in [45]. That is, if the SCF was analyzed, the only difference would be not considering the coupling layers and removing the inverter. For the SCF case, the product of the ABCD matrixes of Fig. 3.2(c) excluding the shunt capacitors and taking into account the approximation of (3.12) is:

$$\begin{bmatrix} 1 & 0 \\ Y_a & 1 \end{bmatrix} \begin{bmatrix} 1 & Z_a \\ 0 & 1 \end{bmatrix} \begin{bmatrix} 1 & 0 \\ -Y_a & 1 \end{bmatrix} \begin{bmatrix} 1 & Z_a \\ 0 & 1 \end{bmatrix} \begin{bmatrix} 1 & 0 \\ Y_a & 1 \end{bmatrix} = \begin{bmatrix} 1 & Z_a \\ 0 & 1 \end{bmatrix} \quad (3.16)$$

This results in the impedance  $Z_a$  in series between the shunt capacitors, corresponding perfectly with the model proposed in [45].

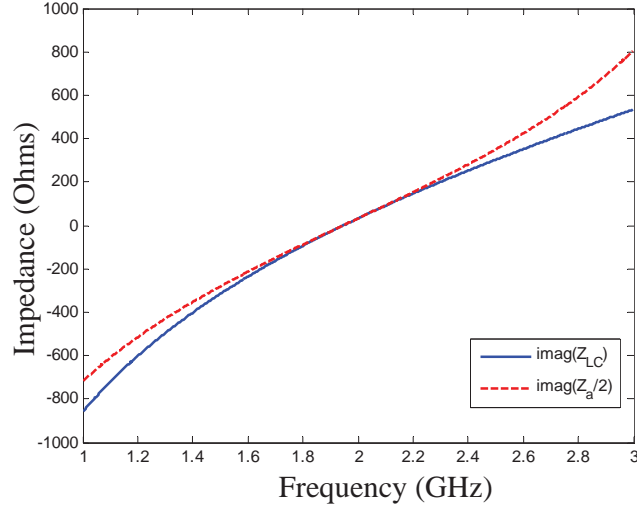


**Figure 3.3:** Comparison between the impedance  $Z_a/2$  and the impedance of the series LC resonator,  $Z_{LC}$ .

### 3.1.2 Synthesis of the Series Impedance $Z_a/2$

In order to synthesize the series impedance  $Z_a/2$  in (3.9) and the impedance of a series LC resonator,  $Z_{LC}$ , with inductance  $L$  and capacitance  $C$ , were expanded in first order Taylor series for frequencies around  $f_a$ , achieving good agreement between them. The values of  $L$  and  $C$  can be obtained by equating the coefficients of the two resulting Taylor expansion series

$$L = \frac{1}{8} \left( \frac{\pi}{k_t} \right)^2 \frac{1}{C_{01} \omega_a^2} \quad (3.17)$$

$$C = \frac{8}{\left( \frac{\pi}{k_t} \right)^2 - 8} C_{01} \quad (3.18)$$

where

$$k_t^2 = \frac{e^2}{Z_{0p} \varepsilon_0 \varepsilon_r v_p} \quad (3.19)$$

In Fig. 3.3,  $Z_a/2$  and  $Z_{LC}$  are compared showing good agreement close to the anti-resonance frequency. A piezoelectric plate of AlN with the properties detailed in Appendix A has been assumed as well as a geometry with an area of  $400 \times 400 \mu\text{m}^2$  and a thickness of  $2.75 \mu\text{m}$  that presents an anti-resonance frequency at 2 GHz.

The operation bandwidth of the model will be limited up to an anti-resonance

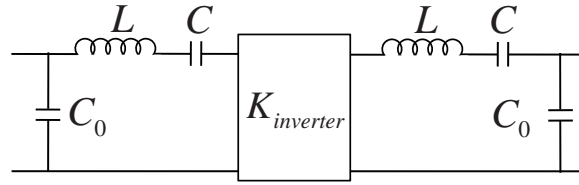


**Figure 3.4:** Equivalent circuit model of a Coupled Resonator Filter.

**Table 3.1:** Variables and Elements of the CRF model

Symbol	Value	Symbol	Value
$A$	$400 \times 400 \mu\text{m}^2$	$C_0$	5 pF
$d$	$2.75 \mu\text{m}$	$L$	24.5 nH
$t$	0.086	$C$	0.27 pF
$K_{coupling}$	0.277 kg/s	$K_{inverter}$	9.46

frequency span of 50%, a limitation caused by the validity range of the approximation of the impedance  $Z_a/2$  by means of a series LC resonator.

It is important to point out that by means of (3.17)-(3.19), the lumped element values of the electrical model can be directly related to the resonator geometry.

Indeed, replacing the impedance  $Z_a/2$  with the inductor  $L$  and the capacitor  $C$  in series, the equivalent circuit model of Fig. 3.4 is obtained. The proposed model captures the performance of any CRF at frequencies around  $f_a$ . It is composed of electrical elements: inductors, capacitors and an impedance inverter. It facilitates working with the CRF in a straightforward way from a completely electrical standpoint.

### 3.1.3 Validation of the Proposed Model of a CRF

In order to validate the proposed model, the transmission response of a two pole CRF is evaluated by means of the Mason model and the proposed all electrical lumped element model.

A stack of two resonators is considered, assuming AlN as piezoelectric material and neglecting the mass loading effect produced by the electrodes.

A set of coupling layers between the resonators is assumed that implement a coupling value of  $K_{coupling}=0.277$ . All the parameters to reproduce the simulation of the model are summarized in Table 3.1.

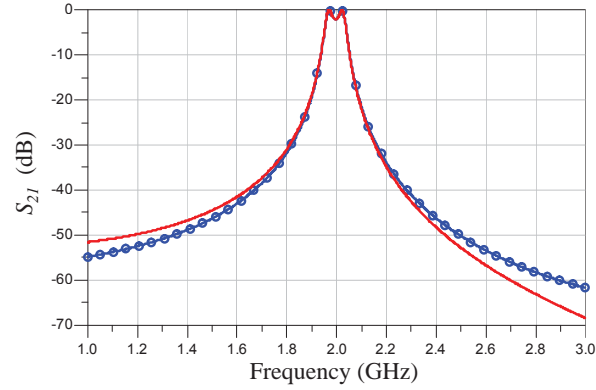


**Figure 3.5:** Simulated transmission response for the proposed equivalent circuit model of the Coupled Resonator Filter (circled line) and for the Mason model based Coupled Resonator Filter (continuous line).

From an acoustic point of view the coupling degree between resonators is  $K_{coupling}=0.277$  kg/s. Section 3.4 will show how the coupling layers can be modeled by means of an impedance inverter. From an electrical standpoint and in accordance with (3.15) an equivalent electrical inverter  $K_{inverter}=9.46$  is necessary.

The transmission response of the proposed model is shown in Fig. 3.5, along with the transmission response of the CRF device simulated by using the accepted Mason model to include the piezoelectric effect. The transmission responses in both cases are practically identical over the whole frequency span simulated in relation to the anti-resonance frequency.

Several simulations have been carried out with different material parameters, areas and frequency bands. All of them accurately fit the frequency spans of up to 50% of the transmission responses simulated by means of both the proposed model and the reference Mason model.

### 3.1.4 Bandpass Prototype Filter Analogy

The electrical equivalent model of the CRF presents a filtering behavior that can be linked to a bandpass prototype filter composed of impedance inverters and series LC resonators. In order to create this link, the network has been reconfigured as shown in Fig. 3.6(a). Two changes have been performed regarding the original model of Fig. 3.4:

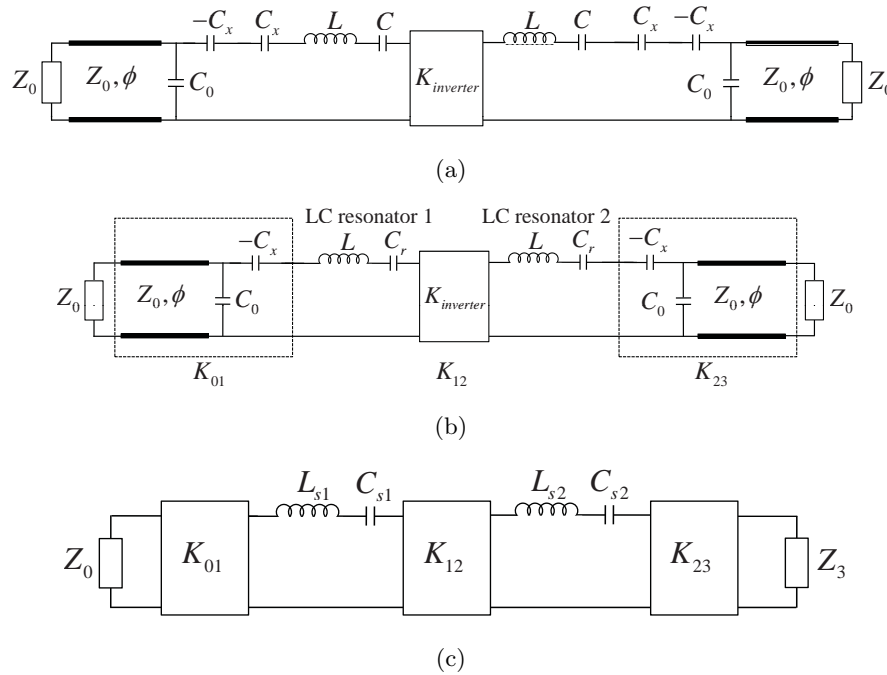


**Figure 3.6:** (a) Reconfigured network of the CRF model (b) Absorption of the transformers. (b) CRF network drawn in order to match the bandpass prototype filter. (c) General bandpass filters using impedance inverters.

- two series capacitors of identical absolute value  $C_x$  and opposite sign have been placed between the shunt parallel plate capacitors  $C_0$  and the series LC resonators. The two capacitors cancel each other out in such a way that no real elements are added to the network and its behavior is unchanged. The purpose of the inclusion of those capacitors is merely to identify the blocks of elements that implement purely impedance inverters and series LC resonators.
- a transmission line with a characteristic impedance equal to the port impedance  $Z_0$  and electrical length  $\phi$  is placed between the shunt parallel plate capacitor  $C_0$  and the port. The transmission line is innocuous because it presents the same impedance as the ports and it only represents a phase shift on the  $S_{21}$  and  $S_{11}$  responses. In this way, the transmission line is included to form an impedance inverter, but it can be removed causing only a phase shift. The inclusion of this innocuous transmission line is useful for analyzing the CRF filtering behavior.

Fig. 3.6(b) shows the model represented in such a way that the pure LC resonators and impedance inverters are identified. The LC resonator has been formed from the

lumped elements  $L$  and  $C$  and adding the series capacitor  $C_x$ . In this way, the LC resonator is formed by  $L$  and  $C_r = (C^{-1} + C_x^{-1})^{-1}$ . The negative capacitor  $-C_x$  and the transmission line contribute to form the impedance inverter along with  $C_0$  as shown in Fig. 3.7. This equivalence can be easily shown by means of ABCD matrixes. The ABCD matrix for the left block can be equated to the ABCD matrix of an impedance inverter as follows:

$$\begin{bmatrix} \cos(\phi) & jZ_0 \sin(\phi) \\ j \sin(\phi)/Z_0 & \cos(\phi) \end{bmatrix} \begin{bmatrix} 1 & 0 \\ j\omega C_0 & 1 \end{bmatrix} \begin{bmatrix} 1 & -j\omega C_x \\ 0 & 1 \end{bmatrix} = \begin{bmatrix} 0 & jK \\ j/K & 0 \end{bmatrix} \quad (3.20)$$

Solving the set of equations coming from each element of the resulting ABCD matrixes for a frequency  $\omega = \omega_0$ , the values of the variables  $C_x$  and  $\phi$  that implement an inverter of value  $K$ , naturally formed, are given by:

$$C_x = \frac{1 + Z_0^2 \omega_0^2 C_0^2}{Z_0^2 \omega_0^2 C_0} \quad (3.21)$$

$$\phi = \tan^{-1} \left( \frac{1}{Z_0 \omega_0 C_0} \right) \quad (3.22)$$

$$K = \frac{Z_0}{\sqrt{1 + Z_0^2 \omega_0^2 C_0^2}} \quad (3.23)$$

The three parameters depend on the impedance  $Z_0$  and the capacitor  $C_0$ . In this way, in a CRF, an inverter of value  $K$  given by (3.23) is naturally formed for a particular parallel plate capacitance of the resonator and port impedance. The capacitor  $C_x$  is very useful because it helps to determine the effective series LC resonator that is formed inside the bandpass filter structure. Having the impedance inverters and series resonators identified and represented will facilitate the full use of the classical coupling theory for microwave filter design in the following chapters.

The lumped elements  $L$  and  $C$  of the CRF model present a resonance frequency  $1/\sqrt{LC}$  that is generated from the mechanical resonance that takes place inside the plates of the resonator and the piezoelectric effect. It is thought to be from the Mason model, removing the shunt capacitor  $C_0$  and taking only into account the motional branch composed of the acoustic transmission lines and the transducing network which includes the impedance transformer and the negative capacitor. Or it can simply be seen as the motional branch of the BVD model for a single resonator. When the BAW resonator is part of the CRF device, the motional branch of the resonator is located in the series position and the electrical branch composed of the capacitor  $C_0$  is located

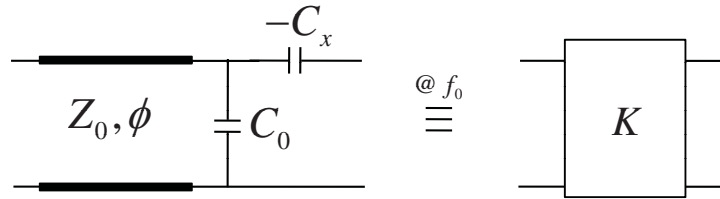


**Figure 3.7:** Impedance inverter equivalence at  $f_0$ .

in the shunt position. The impedance inverter is created between the port and the resonator. However, as a shunt capacitor cannot implement an impedance inverter by itself, the inverter is naturally formed absorbing part of the motional branch which is modelled by means of the capacitor  $-C_x$ . This fact has an effect on the effective motional resonance which is taken into account by means of the capacitor  $C_x$ . In this way, the effective resonator is composed of the series elements  $L$ ,  $C$  and  $C_x$ . The effective resonance can be calculated as  $1/\sqrt{LC_r}$ , where  $C_r$  is formed from the series capacitors  $C$  and  $C_x$ .

The CRF model represented in Fig. 3.6(b) can be easily related and equated to the general bandpass filter of order 2 composed of series resonators and impedance inverters of Fig. 3.6(c).

### 3.2 CRF with Multiple Acoustically Coupled Resonators

The previous section considered the most basic CRF composed of two acoustically coupled BAW resonators. It has been demonstrated that this basic CRF structure behaves essentially as a filter of order 2. The concept of CRF can be extended to include more complex structures having multiple acoustically coupled resonators where the order of the filter is determined by the number of acoustically resonating plates. For example, the near band rejection of a CRF response could be increased by adding a third acoustic resonator as shown in Fig. 3.8 resulting in a filter of order 3. Note that this additional resonator can be composed of a piezoelectric or a non-piezoelectric material because its function is solely resonating unlike the input and output resonators which present a double function as resonators and transducers between the electric and mechanic fields at the same time.

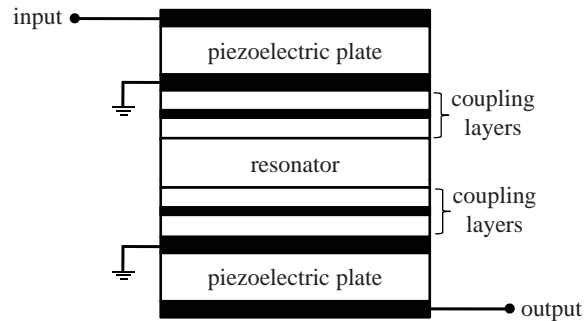


**Figure 3.8:** Cross section of a coupled resonator filter with an additional non-transducing resonator.

This structure contains more layers than the two-pole filter, so it is more difficult to design and to manufacture [70]. In this section, the electrical equivalent model of the previous section is extended for CRFs that include additional non-transducing resonators. An accurate electrical modeling of this structure facilitates a systematic design procedure to obtain the device geometry for a given technology and specifications.

### 3.2.1 CRF Equivalent Network

As observed in the previous section, the Mason model is applied to the input and output piezoelectric resonators with infinitesimal electrodes. The set of coupling layers are taken into account by impedance inverters and the device is considered symmetric. The middle resonator is represented by means of a transmission line as shown in Fig. 3.9(a).

The values of the impedances that implement the transmission lines for the piezoelectric plates ( $Z_{1,1}$  and  $Z_{2,1}$ ) and for the non-piezoelectric plate ( $Z_{1,2}$  and  $Z_{2,2}$ ) are given by (3.1) and (3.2). It is considered a piezoelectric plate of acoustic impedance  $Z_{0p}$  and velocity  $v_p$  and a non-piezoelectric plate of impedance  $Z_{0d}$  and velocity  $v_d$ .

The considered piezoelectric plate thickness is:

$$d = v_p/2f_a \quad (3.24)$$

the considered thickness for the non-transducing resonator plate is:

$$d_2 = v_d/f_d \quad (3.25)$$

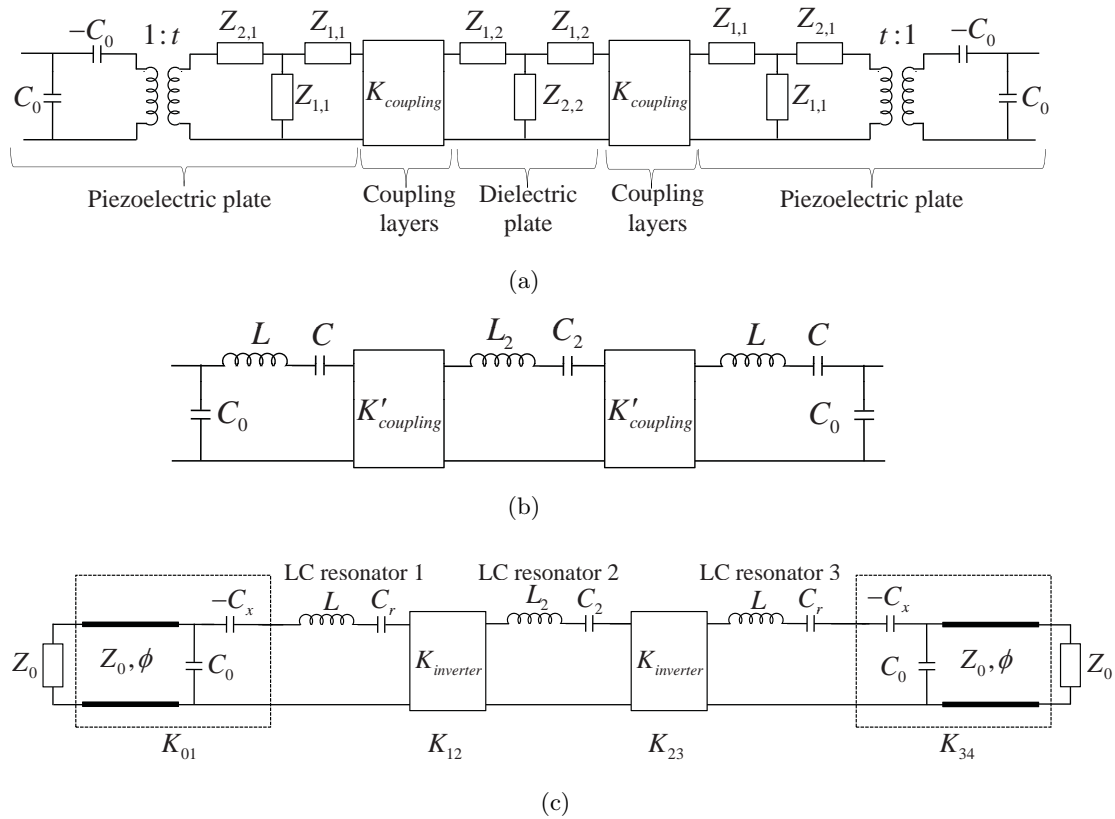


**Figure 3.9:** (c) Original network where the Mason and transmission line models are applied to each piezoelectric and non-piezoelectric plate respectively. (b) Electrical equivalent circuit. (c) CRF network in the form of bandpass filter

where  $f_d$  is the unique resonance that takes place in the pure resonator plate and a thickness of  $\lambda/2$  has been assumed for the middle plate.

### 3.2.2 Equivalent Electrical Model for the Multi-resonator CRF and Bandpass Filter Analogy

The network shown in Fig. 3.9(a) can be reduced to the network shown in Fig. 3.9(b) by means of similar network transformations and approximations as it has been done in the previous section for the CRF of order 2.

The resulting circuit elements are determined by the geometries and the material parameters. The values of lumped elements  $L$  and  $C$  are given by (3.17) and (3.18).

The value of the impedance inverters for this configuration is:

**Table 3.2:** Variables and Elements of the CRF of order 3 model

Symbol	Value	Symbol	Value
$A$	$400 \times 400 \mu\text{m}^2$	$C_0$	5 pF
$d$	$2.75 \mu\text{m}$	$L$	24.5 nH
$d_2$	$2.81 \mu\text{m}$	$L_2$	67.6 nH
$t$	0.086	$C$	0.27 pF
$K_{inverter}$	18.92	$C_2$	0.09 pF
$K_{coupling}$	0.277 kg/s	-	-

$$K_{inverter} = \frac{K_{coupling}}{2t^2} \quad (3.26)$$

The values of the lumped elements that model the behavior of the middle non-transducer resonator are given by

$$L_2 = \frac{Z_{0d}A}{2f_d t^2} \quad (3.27)$$

$$C_2 = \frac{t^2}{2Z_{0d}A\pi^2 f_d} \quad (3.28)$$

Using the same approach as in section 3.1.4, an input and an output inverter can be formed to equate the CRF network to a bandpass filter prototype of order 3 as shown in Fig. 3.9(c). In this way, CRFs of higher orders can be implemented by means of adding additional resonating layers in the structure.

Fig. 3.10 shows the response of a CRF of order 3 with input and output resonators composed of piezoelectric plates and a middle resonator composed of SiO<sub>2</sub> with the properties shown in the Appendix A. The geometries and variables considered are given in Table 3.2.

### 3.3 Asymmetrically Coupled Resonator Structures

In most cases, coupled resonator structures are assumed to be symmetrical in terms of area, that is, the top and bottom BAW resonators are stacked and aligned, and are assumed to have the same area. In this case, the mechanical load condition in the whole area of the structure is the same and can be modeled by means of cascading Mason models of each BAW resonator only approximating a propagation of the thickness mode. The electrical response of these structures presents a wide bandwidth and a very

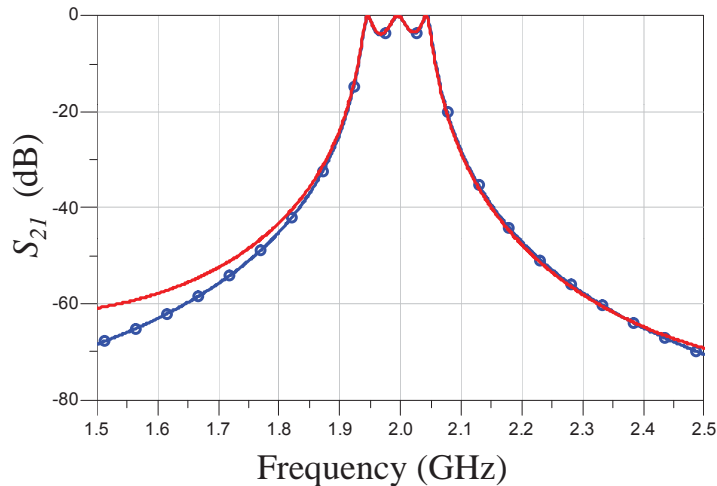


**Figure 3.10:** Simulated transmission response for the proposed equivalent circuit model of the Coupled Resonator Filter of order 3 (circled line) and for the Mason model based Coupled Resonator Filter (continuous line).

good out-of-band rejection, but unlike ladder or lattice filters, transmission zeros in the transmission response are not achievable. However, forcing different load conditions in the structure, a transmission zero can be obtained as found experimentally in [71].

The analysis of this kind of asymmetrical structure has to take into account all the load conditions over the considered plates. Due to the continuity conditions in terms of electrical field and mechanical displacement, each of the regions of the structure under the same load conditions will be modeled with an independent Mason model. The significance of this consideration is based on the possibility of using the one dimensional Mason model in modeling two dimensions, and the chance of applying this to a more general case.

### 3.3.1 Structure Definition

The most basic CRF structure is composed of two stacked BAW resonators and a set of coupling layers. Each resonator is defined by thickness  $d_i$ , and area  $A_i$  with  $i = 1, 2$  for the upper and bottom resonator, as shown in Fig. 3.11. Infinitesimal electrodes are assumed to simplify the structure and to illustrate the process of obtaining the model. Note that when  $A_1 = A_2$  and  $d_1 = d_2$  the structure corresponds to the standard symmetrical CRF and also that by removing the acoustic coupling layers a SCF section

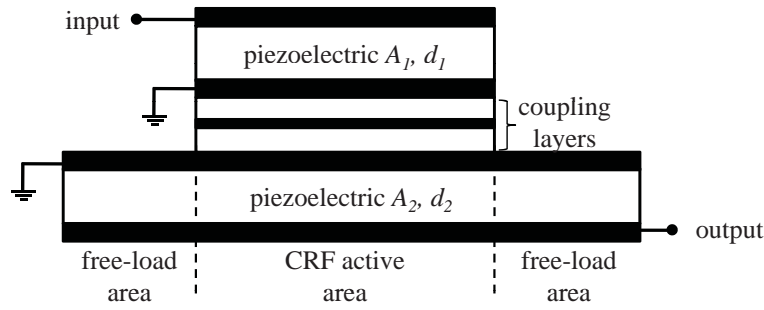


**Figure 3.11:** Basic scheme of an acoustically coupled resonator asymmetrical structure.

can be revealed. Taking into account the different areas of both resonators, two different regions must be distinguished in the structure: a common active area, given by  $A_1$ , shared by all the layers in the stack; and a free-load area in the bottom resonator that corresponds to the area given by  $\Delta A = A_2 - A_1$  in which the mechanical load is air, which behaves like an acoustic short-circuit.

The one dimensional Mason model comes from the analysis of the propagation of the acoustic wave through the structure. This means that this model can only be applied to that region or area which has the same mechanical load conditions. In this case, it is straightforward to state that each area of the structure, the active and the free-load area, must be modeled with an independent Mason model. Of course, both areas must fulfill the one dimensional conditions [60]. Taking this into account, both the active and free-load area will be modeled with the Mason model setting an area  $A_1$  in the first case and  $\Delta A$  in the second.

Although the load condition in each region is different, continuity from the electrical and mechanical point of view must be accomplished. Since there is electrical continuity in the bottom resonator, the Mason model of each region must be connected in shunt configuration, accurately modeling the longitudinal mode response of the whole structure. Taking all these considerations into account, the electrical model can be developed, as well as the electrical equivalent circuit, which presents a useful electrical network.

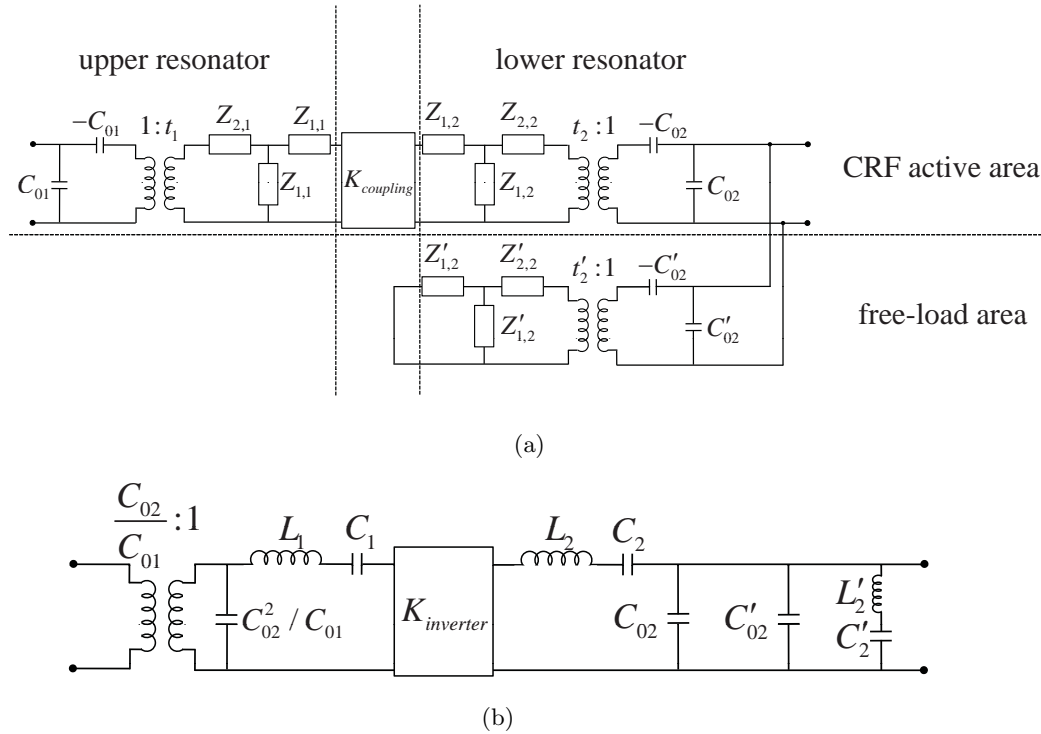


**Figure 3.12:** (a) Network of the asymmetrical structure using the Mason model. (b) Electrical equivalent circuit.

### 3.3.2 Electrical Equivalent Circuit

In Fig. 3.12(a), the complete asymmetrical structure by means of the Mason model is shown. Here, the active area is modeled like the classical symmetrical CRF structure, while the free-load area is electrically connected in a shunt configuration with its corresponding Mason model.

The network is made up of two parallel branches for each region of propagation. The input and output ports of the equivalent circuit are the electric ports of each resonator. In the region corresponding to the active area, the two resonators are connected to each other by means of one of their respective acoustic ports. In a CRF, the mechanical coupling takes place by means of the coupling layers. The degree of acoustic coupling is modeled with the impedance inverter ( $K_{coupling}$ ).

The values of the impedances in the applied Mason models can be expressed as:

$$Z_{1,i} = jZ_{0p}A_1 \tan\left(\frac{\theta_i}{2}\right) \quad (3.29)$$

$$Z_{2,i} = -jZ_{0p}A_1 \operatorname{cosec}(\theta_i) \quad (3.30)$$

$$Z'_{1,2} = jZ_{0p}\Delta A \tan\left(\frac{\theta_2}{2}\right) \quad (3.31)$$

$$Z'_{2,2} = -jZ_{0p}\Delta A \operatorname{cosec}(\theta_2) \quad (3.32)$$

with  $i=1, 2$ , where  $Z_{0p}$  is the acoustic impedance per unit area of the piezoelectric material and  $\theta$  is the acoustic length.

The value of the static capacitors is given by:

$$C_{0i} = \frac{A_1\varepsilon}{d_i} \quad (3.33)$$

$$C'_{02} = \frac{\Delta A\varepsilon}{d_2} \quad (3.34)$$

In order to model the asymmetrical CRF in such a way that the device's behavior can be easily understood, the same approach of section 3.1 is followed taking into account the new geometry variables of the asymmetric structure to obtain the circuit presented in Fig. 3.12(b).

The model obtained consists of a part belonging to the active area, which is similar to the symmetrical CRF but contains different element values and the presence of a transformer due to the asymmetry of the device, and a part belonging to the free-load area of the CRF which performs like a single resonator. The device behaves in the same way as a CRF, where asymmetric thickness can be assumed, connected to an independent resonator in parallel at one port. The lumped element values of the equivalent circuit are:

$$L_1 = \frac{1}{8} \left(\frac{\pi}{k_t}\right)^2 \frac{C_{01}}{C_{02}^2 \omega_{a1}^2} \quad (3.35)$$

$$C_1 = \frac{8}{\left(\frac{\pi}{k_t}\right)^2 - 8} \frac{C_{02}^2}{C_{01}} \quad (3.36)$$

$$L_2 = \frac{1}{8} \left(\frac{\pi}{k_t}\right)^2 \frac{1}{C_{02}\omega_{a2}^2} \quad (3.37)$$

$$C_2 = \frac{8}{\left(\frac{\pi}{k_t}\right)^2 - 8} C_{02} \quad (3.38)$$

$$L_2' = \frac{1}{8} \left(\frac{\pi}{k_t}\right)^2 \frac{1}{C_{02}'\omega_{a2}^2} \quad (3.39)$$

$$C_2' = \frac{8}{\left(\frac{\pi}{k_t}\right)^2 - 8} C_{02}' \quad (3.40)$$

The inverter value is:

$$K_{inverter} = \frac{K_{coupling}}{4t_2^2} \quad (3.41)$$

From Fig. 3.12(b) it can be predicted that the ground derived LC resonator will introduce a transmission zero at its resonance frequency because here it behaves like a short-circuit. In this way, a one-dimensional analysis approach can be extended to several regions on a two-dimensional plane. The model presented in Fig. 3.12(b) is useful to understand the behavior of the structure.

The Mason model has been extensively validated in literature as a tool to model 3D structures in which the boundaries of the plates share the same boundary conditions on all their surfaces. However, our proposal involves the parallel connection of one-dimensional Mason models to gather the behavior of 3D structures with different load conditions on different parts of the surface in some boundaries. Therefore, in order to validate the proposal, the next section includes a 3D simulation of the acoustic structure.

### 3.3.3 Validation of Asymmetrical Structures Using 3D Simulations

In the previous section, the electrical equivalent circuit for an asymmetrical structure was developed, in which the presence of a free-load area was modeled by a shunt

**Table 3.3:** Definition of Asymmetrical CRF Geometry

	Layer	Dimension ( $\mu\text{m} \times \mu\text{m} \times \mu\text{m}$ )
Top resonator	Top electrode	$60 \times 60 \times 0.2$
	Piezoelectric plate	$60 \times 60 \times 1.06$
	Bottom electrode	$60 \times 60 \times 0.2$
Coupling layers	SiO2	$60 \times 60 \times 0.525$
	W	$60 \times 60 \times 0.785$
	SiO2	$60 \times 60 \times 0.525$
Bottom resonator	Top electrode	$180 \times 180 \times 0.2$
	Piezoelectric plate	$180 \times 180 \times 1.06$
	Bottom electrode	$180 \times 180 \times 0.2$

resonator. From the electrical point of view, we can state that the shunt resonator will contribute a transmission zero placed at its own resonance frequency  $f_r$ . The model has been developed from the parallel connection of Mason models to gather the effect of different boundary conditions on the same surface of a plate. In order to demonstrate the validity of the proposed Mason models connection, a 3D simulation has been carried out using ANSYS software.

The proposed structure is composed of two BAW resonators that are acoustically coupled by a set of coupling layers SiO2/W/SiO2. The upper resonator has been centered over the lower resonator and both BAW resonators are square shaped. The dimensions of the layers of the asymmetric structure are listed in Table 3.3. As discussed previously, the lateral dimensions should be much greater than the thickness to ensure the resonator mainly operates in the thickness mode. In [65], a lateral-to-thickness ratio of 50:1 is preferred. In general, the higher the ratio, the better the one-dimensional approximation of the thickness mode.

In Fig. 3.13, the asymmetrical CRF transmission response is shown. Both the 1D simulation by means of the equivalent electrical circuit and the 3D simulation agree. Unlike the 1D simulation, some ripple due to the lateral modes of the structure appears in the 3D simulation. These modes cannot be predicted by the 1D simulation since it only takes into account the propagation of longitudinal acoustic waves through the structure. However, the most important fact lies in the presence of a transmission zero, which is a contribution from the free-load area of the structure. When the acoustic waves propagate from the top to the bottom BAW resonator, not only the active area must be considered. The mechanical displacement at the bottom resonator generates a longitudinal electrical field. Due to the electrical continuity, the electrical field

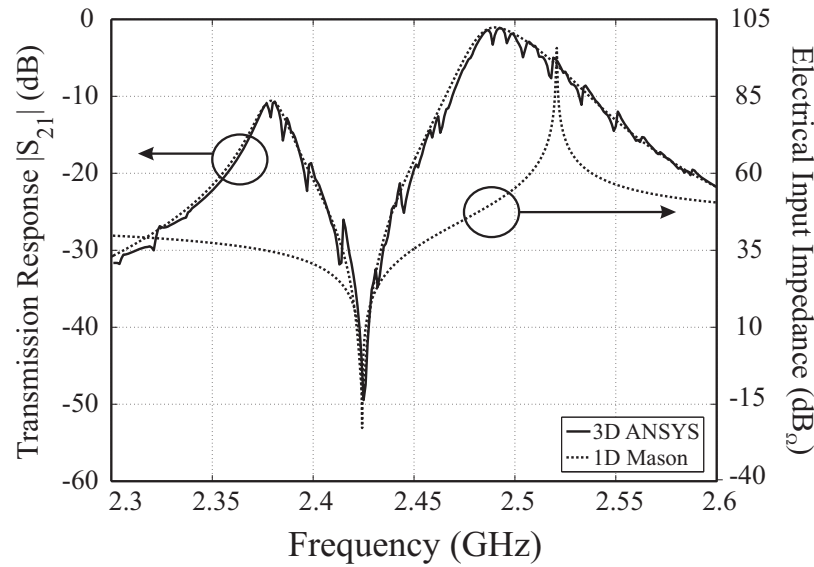


**Figure 3.13:** Transmission response for the asymmetrical CRF structure by means of 1D Mason model (dashed line) and 3D simulation (solid line) including the electrical input impedance of the free-load area..

will be distributed in the whole area of the electrodes. In this case, the free-load area will behave like a single BAW resonator, with a certain resonance and anti-resonance frequency. At the resonance frequency, the free-load behaves like a short circuit, contributing a transmission zero, whereas at the anti-resonance frequency, the bandpass response of the structure is not degraded since the free-load area behaves like an open circuit. In Fig. 3.13, the electrical impedance of the free-load area is also shown in order to confirm the previous statement.

In Fig. 3.14(a), the mechanical displacement at the frequency of maximum transmissivity of the filter response is shown. It can be seen that the mechanical displacement is mainly concentrated in the active area, being almost negligible in the free-load area. In the same way, an examination of the mechanical displacement at the frequency of the transmission zero, which is shown in Fig. 3.14(b), reveals that the mechanical displacement is mainly concentrated in the free-load area, whereas it is almost negligible in the active area. This situation confirms the previous statement that the free-load area should be modeled as an independent BAW resonator that is electrically connected in a shunt configuration with the bottom resonator of the active area.

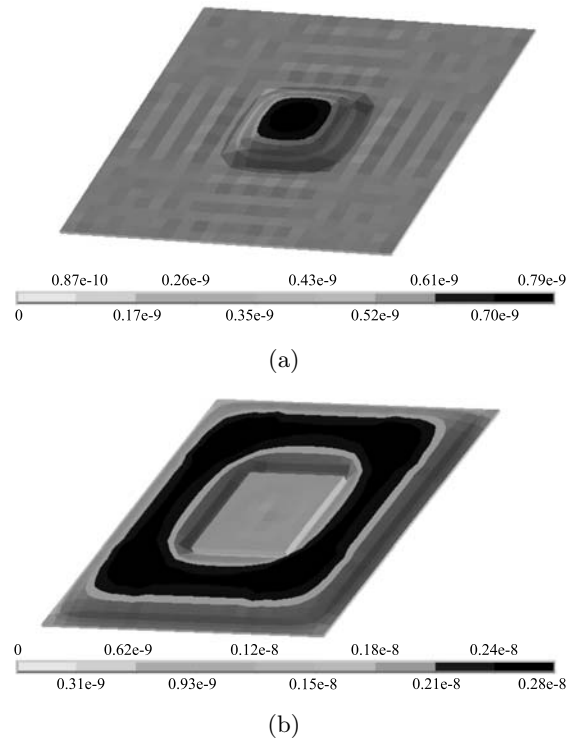


**Figure 3.14:** Mechanical displacement vector sum for: (a) frequency of maximum transmission and (b) free-load area resonance frequency.

## 3.4 Coupling Layers Mechanism

The sections presented above have modeled the set of coupling layers in a CRF as an impedance inverter. This section will demonstrate that model and will establish a set of closed form expressions that relate the geometry and the material parameters of the coupling layers with the inverter value.

### 3.4.1 Multiple Coupling Layers as a Coupling Mechanism

From the microwave engineering perspective, a coupling between resonators can be implemented by means of several mechanisms that can be modelled by impedance inverters at a frequency of operation [72]. From the thin film bulk acoustic wave technology perspective, the only acoustic coupling mechanism between resonators that can be implemented at the moment is by means of thin film layers. A thin film layer is analog to a transmission line, and it is well-known that one of the most basic impedance

inverters is a  $\lambda/4$  transmission line which presents an inverter value  $K$  equal to its characteristic impedance. Therefore, it could be thought that the most logical way to couple the two resonators is by means of a thin film layer of  $\lambda/4$  thickness assuming the acoustic wavelength in such a way that the longitudinal wave will travel an acoustic length of  $\pi/2$  across the coupling layer, and the value of the acoustic impedance of the transmission line will be the desired inverter value  $K$ .

However, the main obstacle to implementing this approach is the impossibility of fulfilling a desired coupling value, or in other words, a required impedance inverter value. The coupling value that only one layer of a conventional material can implement is too high to fulfill the typical bandwidths required by applications to which BAW filters are targeted such as UMTS, ISM or GPS. That is to say, the impedance of the material is too high regarding the desired impedance inverter value  $K$ . Moreover, the acoustic impedance  $Z_a$  is given by the product of the intrinsic acoustic impedance of the material  $Z_{a0}$  and the active area of propagation of the longitudinal wave  $A$ . The active area is determined by the resonators which transduce the signal between the electrical and the mechanical fields. There is no control on the intrinsic acoustic impedance of a material and the set of available materials is limited to those used in the thin film and semiconductor industry. In this way, there is no control on the acoustic impedance of the coupling layer.

The first issue was solved using the Bragg reflector approach which is based on the combination of a set of alternatively placed high and low impedance layers to achieve a mechanism block that presents an effective, very low impedance. This mechanism block is called coupling layers. Initially, those layers had a thickness corresponding to  $\lambda/4$  [73]. However, as the number of available practical materials in the industry is limited, the number of coupling values that can be implemented is very limited as well. Currently, research on materials with very low impedance is being carried out in the BAW industry. For example in [50], a thin polymer film is investigated as unique coupling layer due to its very low acoustic impedance  $< 0.5 \cdot 10^7$  kg/s/m<sup>2</sup>, compared to materials like SiO<sub>2</sub> which has a value of  $1.2 \cdot 10^7$  kg/s/m<sup>2</sup>. Other materials such as organic films and certain oxides are possible candidates to act as a single coupling layer. The main drawback of some of these materials is that they are relatively lossy. Porous silicon (PS) dioxide is investigated in [74] where a large mismatch between the acoustic impedances of a Bragg mirror is needed to broaden the bandwidth of the mirrors. Acoustic impedances of  $0.95 \cdot 10^7$  kg/s/m<sup>2</sup> are reported for PS layers. In this

way, PS could also be a suitable candidate for single layers CRFs.

Then, the second issue was solved using the thickness of the coupling layers as a design variable, not restricting them to a thickness of  $\lambda/4$  [49]. This additional degree of freedom in the designing of the coupling layers brings a wide range of coupling values that can be implemented.

In general, the design of the coupling layers has been performed by means of optimization procedures together with other layers that implement the CRF, including the resonators, to achieve a required acoustic transmissivity trying to find an optimal coupling to fulfill the filter specifications. Those optimization procedures are time-consuming because of the high number of design parameters to be optimized and their convergence on local solutions can avoid the use of the full potential of CRFs. Moreover, a loss of understanding about the coupling and resonance mechanisms that take place in the structure happens when just one optimization process is carried out.

In this section, the coupling layers mechanism is analyzed in such a way that the coupling trends are shown and the implementable coupling value limits are stated. In addition, a set of closed-form expressions to fulfill a desired coupling value is presented. This approach is useful to implement the coupling theory of filter design that will be developed in next chapters.

### 3.4.2 Generalized Impedance Inverter

Next, the set of coupling layers will be analyzed and the way in which they can implement an impedance inverter will be demonstrated. The coupling layers can be treated as acoustic transmission lines with their associated acoustic impedance and velocity. Two types of materials are considered herein: high and low acoustic impedance materials, because their high acoustic impedance ratio offers the widest range of possible coupling values as can be observed below. Taking into account the acoustic impedance of the selected materials, it is possible to find the acoustic transmission line (TL) lengths that will fulfill the desired coupling value between resonators. If we consider the transmission matrix for the  $i$ -th lossless TL as [23]:

$$ABCD_{L_{i-th}} = \begin{pmatrix} \cos(\phi_i) & jZ_i \sin(\phi_i) \\ \frac{j \sin(\phi_i)}{Z_i} & \cos(\phi_i) \end{pmatrix} \quad (3.42)$$

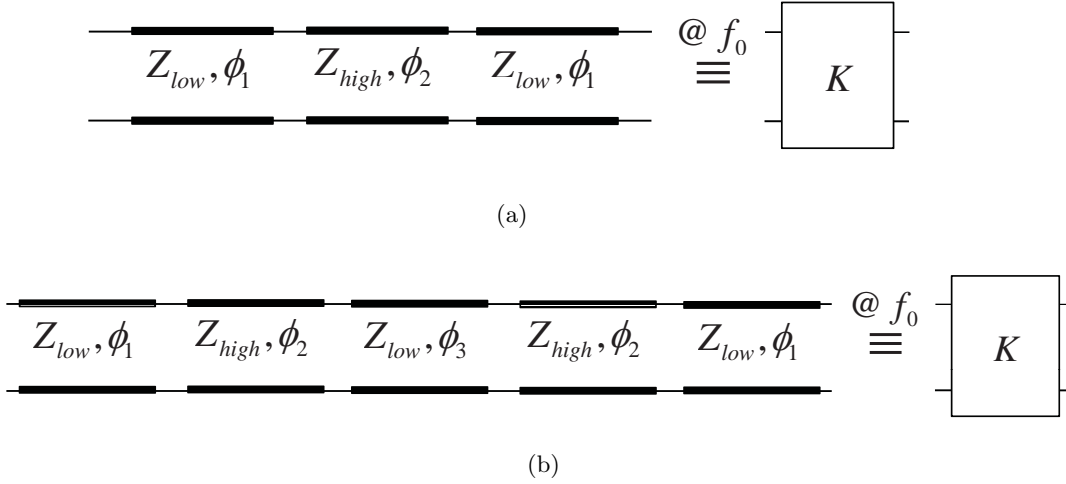


**Figure 3.15:** (a) Three coupling layers behaving as impedance inverter and (b) five coupling layers behaving as impedance inverter.

where  $\phi_i$  is the acoustic TL-length and  $Z_i$  is the acoustic characteristic impedance of the  $i$ -th layer. The transfer matrix for the layer structure will be an impedance inverter by definition if the hereafter equality is given at a determined frequency:

$$ABCD_{L1} \cdot ABCD_{L2} \cdots ABCD_{Ln} = ABCD_{inverter} = \begin{pmatrix} 0 & \pm jK \\ \pm j/K & 0 \end{pmatrix} \quad (3.43)$$

### 3.4.3 Closed-Form Expressions for the Coupling Layers Dimensions

As a first approach a three layer structure will be analyzed. Fig. 3.15(a) shows its equivalent transmission line circuit. The impedance and acoustic length sequence is summarized in Table 3.4. The layers placed in odd positions present a low impedance material ( $Z_1 = Z_3 = Z_{low}$ ) and the same acoustic length  $\phi_1 = \phi_3$ . The layer placed in the middle of the stack presents a high impedance material ( $Z_2 = Z_{high}$ ) and length  $\phi_2$ . Note that the contrariwise configuration can be implemented with high impedance in the odd layers and low impedance in the even ones. Solving the system of equations resulting from (3.43), it is possible to obtain the acoustic TL-lengths according to the desired coupling value  $K$  and the available material impedances  $Z_{low}$  and  $Z_{high}$ :

**Table 3.4:** Structure of the multi-layer inverter

Layer	Three-layer structure		Five-layer structure		Example structure	
	$Z_i$	$\phi_i$	$Z_i$	$\phi_i$	Thickness ( $\mu\text{m}$ )	Material
Layer 1	$Z_{low}$	$\phi_1$	$Z_{low}$	$\phi_1$	0.270	SiO <sub>2</sub>
Layer 2	$Z_{high}$	$\phi_2$	$Z_{high}$	$\phi_2 = 90^\circ$	0.420	W
Layer 3	$Z_{low}$	$\phi_3 = \phi_1$	$Z_{low}$	$\phi_3$	0.270	SiO <sub>2</sub>
Layer 4			$Z_{high}$	$\phi_4 = 90^\circ$		
Layer 5			$Z_{low}$	$\phi_5 = \phi_1$		

$$\tan(\phi_1) = \sqrt{\frac{K^2 - Z_{high}^2}{Z_{low}^4 - K^2 Z_{high}^2}} Z_{low} \quad (3.44)$$

$$\tan(\phi_2) = \frac{\sqrt{Z_{low}^4 - K^2 Z_{high}^2} \sqrt{K^2 - Z_{high}^2} (K^2 - Z_{low}^2)}{Z_{low}^4 Z_{high}^2 - K^2 Z_{low}^4 - K^2 Z_{high}^4 + K^4 Z_{high}^2} Z_{high} \quad (3.45)$$

Now a continuous range of values is available to implement the required inverter control. However, the range of feasible values for the inverter control is limited because the acoustic lengths must be a real number. The upper and lower limits are:

$$\frac{Z_{low}^2}{Z_{high}} < K < Z_{high} \quad (3.46)$$

The contrariwise configuration extends the range in the upper limit but reduces it in the lower limit. The analyzed configuration is more appropriate because of the small typical required inverter values.

As stated above, in some cases the required inverter control value could be outside the feasible value range using three layers. However, this situation rarely occurs for typical applications where CRFs are used. A way to extend this range is using five symmetrical stacked coupling layers. The transmission line equivalence is shown in Fig. 3.15(b). The full coupling structure is summarized in Table 3.4. For the sake of simplicity, layers placed in even positions will have a quarter-wave length and the acoustic lengths of the remaining layers are:

$$\tan(\phi_1) = \sqrt{\frac{K^2 Z_{low}^2 - Z_{high}^2}{Z_{low}^6 - K^2 Z_{high}^4}} Z_{low} \quad (3.47)$$

$$\tan(\phi_3) = \frac{(K^2 - Z_{low}^2) \sqrt{K^2 Z_{low}^2 - Z_{high}^4} \sqrt{Z_{low}^6 - K^2 Z_{high}^4}}{Z_{low}^6 Z_{high}^4 - K^2 Z_{low}^8 - K^2 Z_{high}^8 + K^4 Z_{low}^2 Z_{high}^4} Z_{high}^2 Z_{low} \quad (3.48)$$

In this case, the range of feasible values has been increased:

$$\frac{Z_{low}^3}{Z_{high}^2} < K < \frac{Z_{high}^2}{Z_{low}} \quad (3.49)$$

### 3.4.4 Coupling Layers Frequency Behavior

The inverter implementation by means of transmission lines has an inherent limited bandwidth. The multi-layer approach is considered at a single frequency at which the set of layers presents a total acoustic length of  $90^\circ$  and the desired inverter value. In this way, the multi-layer inverter presents good behavior in narrowband.

In order to exemplify the coupling layers' behavior, the inverter that models the coupling layers in section 3.1 of value  $K_{inverter}=0.277$  kg/s is implemented with the three-layer inverter solution. It has to be noted that in section 3.1, for the sake of simplicity, the simulation of the acoustic inverter was implemented by means of an ideal acoustic inverter having an impedance that does not exist in conventional materials. Herein, the acoustic inverter is implemented by means of a set of real conventional materials.

The thicknesses of the layers summarized in Table 3.4 can be obtained from (3.44) and (3.45), using silicon dioxide,  $\text{SiO}_2$ , as low impedance material, tungsten, W, as high impedance material and an acoustic propagation active area,  $A$ , of  $400 \times 400 \mu\text{m} \times \mu\text{m}$  determined by the filter synthesis procedure. In this way,  $Z_{low} = Z_{\text{SiO}_2} A$  and  $Z_{high} = Z_W A$ , where  $Z_{\text{SiO}_2}$  and  $Z_W$  are the acoustic impedances per area unit of each material in  $\text{kg}/(\text{m}^2\text{s})$ . The acoustic impedances of W and  $\text{SiO}_2$  are given in Appendix A.

Fig. 3.16 shows the acoustic lengths that must be implemented using the 3-layer solution for a specific inverter value between resonators. Note that one of the solutions presents a negative sign, meaning that an angle of  $\pi$  rad needs to be added to that solution to obtain an implementable layer. The minimum coupling takes place when all the layers have an angle of  $\pi/2$ , the quarter-wave layers solution. Therefore, any

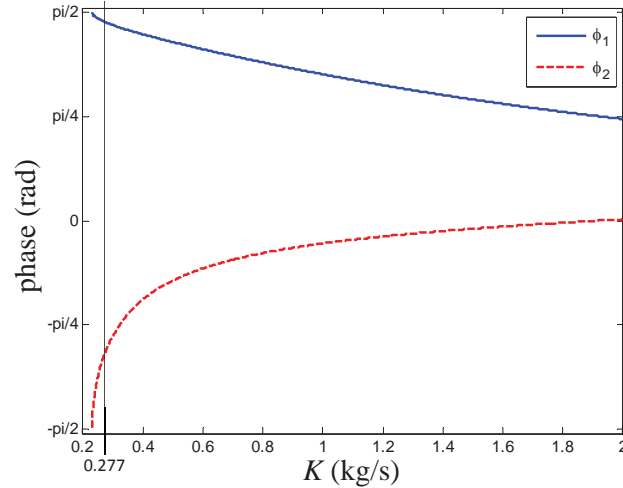


**Figure 3.16:** Required acoustic lengths to fulfill a particular inverter value using the 3-layer inverter solution.

coupling value obtained by modifying the thickness of the layers will be higher than the quarter-wave reference.

The magnitude and phase responses of the proposed inverter are shown in Fig. 3.17. In order to evaluate this behavior, the inverters have been simulated with the ports matched to the ideal inverter value. In this way, we can check the transmission coefficient both in magnitude and phase and thus, we can assess the quality of the multi-layer inverter that is implemented. The transmissivity deviation is better than 0.1 dB inside the passband of the filter. The phase response is between the range of  $80^\circ$  and  $100^\circ$ , being  $90^\circ$  at the center frequency of the filter. The phase slope makes the layers' behavior move away from the ideal inverter behavior at frequencies far from the design frequency. Fig. 3.17 also shows the response of the filter once the coupling layers have been implemented, compared to the response obtained using an ideal inverter modeling the coupling layers that show good agreement, close to the center frequency of the filter. The presented example filter has been simulated and validated using the Mason model. A slight reduction of the bandwidth occurs due to the narrowband behavior of the coupling layers around the design frequency.

Fig. 3.18 shows the filter response in a wider span of frequencies to illustrate the presence of spurious peaks stemming from the resonances of the structure caused by the

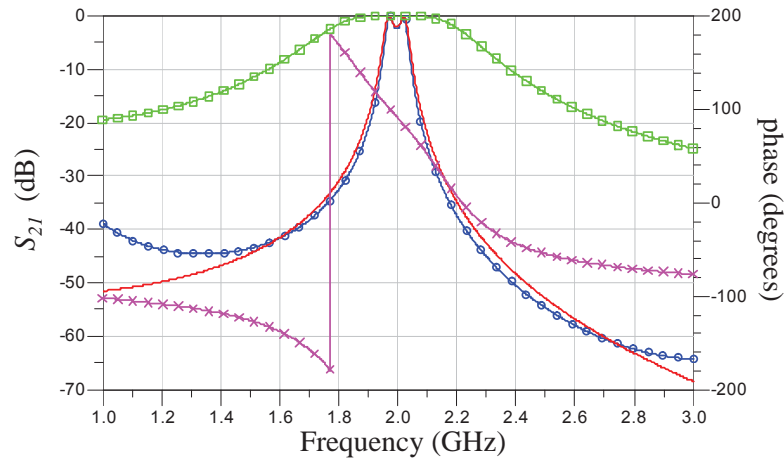


**Figure 3.17:** Filter response implemented with an ideal inverter such as coupling layers (continuous line) and with real coupling layers (circled line). Evaluation of the implemented multi-layer inverter by means of the magnitude (squared line) and the phase (crossed line) when its ports present the impedance of the desired coupling value, 0.277 kg/s.

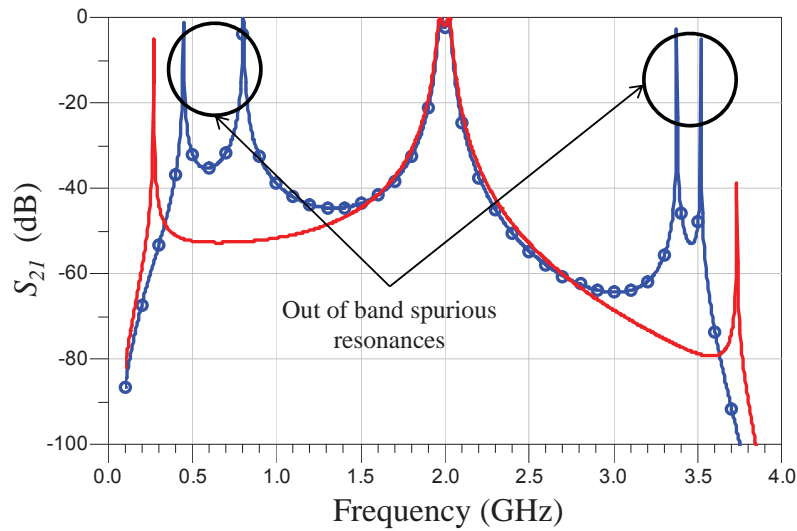


**Figure 3.18:** Out-of-band spurious resonances originated from the multi-layer structure in a CRF with an inverter modeling the coupling layers (continuous line) and with real coupling layers (circle line).

multi-layer coupling structure. Depending on the chosen solution for the inverter, the spurious peaks are placed at different frequencies. The resonance periodicities depend on the number of layers used to implement the inverter, their thicknesses and the reflection coefficients between the several layers.

### 3.5 Single Coupling Layer

[51] demonstrates that there are materials with sufficiently low acoustic impedance, that the two resonators in a CRF can also be sufficiently decoupled with only one layer as shown in Fig. 3.19(a). In this case, a single coupling layer is placed between resonators. Some organic materials present acoustic impedances of around  $2.8 \text{ kg/s/m}^2$  and can be used as the single coupling layer. However, the drawback to using these materials is that they are relatively lossy, between 1000 and 2000 dB/cm.

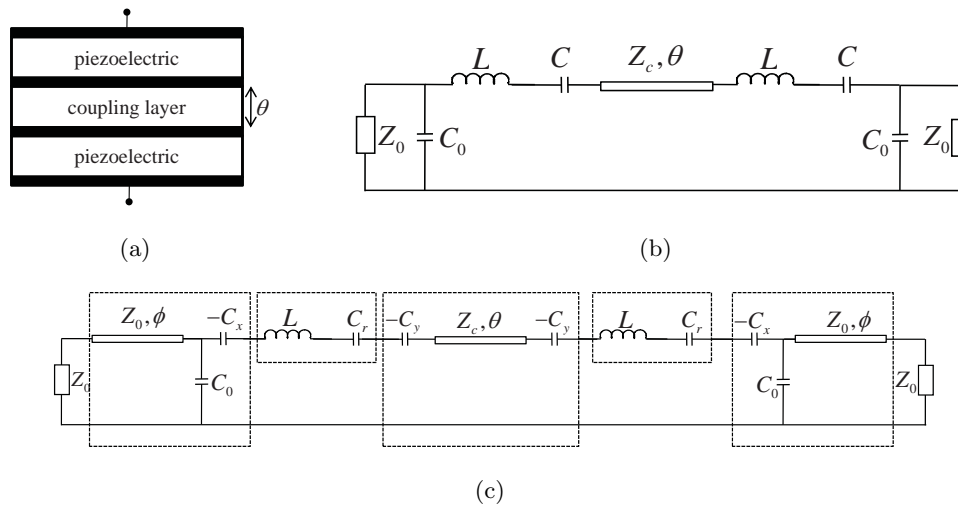


**Figure 3.19:** (a) CRF layered structure, (b) CRF with Single Coupling Layer Model and (c) redrawn model to identify resonators and impedance inverters.

The coupling degree between resonators may be controlled by means of the thickness of the single coupling layer. This section will present how to modify the equivalent electrical model for the coupled resonator filter in order to include the effects of having a non-quarter-wave coupling layer as a coupler.

A model can be obtained for the CRF with a single coupling layer as shown in Fig. 3.19(b) based on the equivalent circuit model proposed in section 3.1. In this case, the

coupling layer is not represented by means of an impedance inverter but a transmission line of acoustic length  $\theta$ . This is so, because it does not assume the role of inverter by itself, since it does not have an acoustic length of  $90^\circ$ . Actually, part of the BAW resonator contributes to creating the inter-resonator impedance inverter and also the input/output inverters.

As can be observed in Fig. 3.19(c), the fact that the resonators are contributing to the couplings is modeled by the capacitors  $C_x$  in the case of the external couplings as shown in section 3.1, and the capacitors  $C_y$  in the case of inter-resonator coupling. When the resonator contributes to the coupling with  $C_x$  and  $C_y$ , its resonance behavior is naturally modified and it will be modeled by modifying the capacitor  $C$  which absorbs the opposite sign capacitors  $-C_x$  and  $-C_y$ , and becomes  $C_r=1/(1/C+1/C_x+1/C_y)$ . That is to say, the effective resonance of the BAW resonator is being modified when a part of this resonator also contributes to the strength of the acoustic coupling. Using ABCD matrixes, it can be demonstrated that a transmission line with a characteristic impedance  $Z_c$  and acoustic length  $\theta$  placed between two series negative capacitors of value  $-C_y$  behave as an impedance inverter at a frequency  $f_0$ . The value of  $C_y$  that makes the structure behave as an impedance inverter  $K$  for a value of  $\theta$  can be obtained:

$$C_y = \frac{\tan(\theta)}{\omega_0 Z_c} \quad (3.50)$$

$$K = \frac{Z_c}{\sin(\theta)} \quad (3.51)$$

Thus, a modification of the effective resonators in a CRF takes place when a non-quarter-wave single coupling layer is used as a coupling mechanism besides the modification that comes from the static capacitor.

### 3.6 Summary

This chapter proposes an equivalent electrical model for the electro-acoustic device studied in this dissertation, the CRF. The model and its extensions are a link between the physical device and the filter prototypes. The component values of the models are related to the geometries of the device and the material parameters of the layers. Closed-form expressions have been derived for the component values following a set of simplifying assumptions without loss of generality. Complex multilayered structures

match the proposed models and the component values can be easily extracted matching the response of the model and the structure. Equivalent electrical models have been derived for the most common CRF structure composed of 2 resonators, and it has been derived to variations such as CRFs with 3 resonators and asymmetrical CRFs, that is to say CRFs with resonators of different geometries both in thickness and area.

This chapter has also demonstrated the behavior of a typical CRF as a filter of order 2, and it has also shown that adding acoustically coupled resonators to the stack leads to higher order filters. However, the behavior of a CRF is significantly modified when resonators of different areas are considered. A transmission zero appears in the transmission response due to acoustic boundary conditions.

The coupling layers of CRF structures can be modeled by means of impedance inverters. The inverter values have a relation with the properties and geometries of the layers. A single coupling layer with very low acoustic impedance as a coupling mechanism between resonators is being investigated in the BAW community. The control of the coupling degree in single layers is carried out by means of modifying of its thickness, and when it occurs, the CRF model must be modified in order to take into account the effects of the coupling layer on the resonances.

More importantly, for the purpose of this dissertation, the models draw a clear picture of the filter mechanisms that take place inside the structure: resonances and couplings.

## Chapter 4

# Design of Acoustically Coupled Resonator Filters

The aim of this chapter is the synthesis of bulk acoustic wave (BAW) coupled resonator filters (CRFs) from a set of filtering specifications. The geometries of the BAW structures and the values of other possible external elements will be determined when needed. Therefore, the physical dimensions of the filter for fabrication can be obtained. The techniques presented in this chapter can deal with the complex multilayered structures typically present in BAW technology discussed in the introduction of this work.

The design of CRFs has typically been based on optimization procedures on the geometries of the device in order to obtain a response that fits the required filter specifications. The thickness of the layers and the active area of the structure are common design variables. The input data in the design process are material properties such as density, acoustic velocity, permittivity or electromechanical coupling constant in piezoelectric layers. The Mason model presented in section 2 is the workhorse of BAW resonator design and analysis [75]. It provides an accurate modelling of the acoustic longitudinal mode wave propagation thorough the stack of thin film layers of BAW devices and also of the piezoelectric effects. In this way, optimization procedures on the 1D Mason model are far more rapid and convenient than 3D simulations and also provide accurate results of the main mode of propagation. However, a BAW filter design process which only relies on optimization procedures skips information and understanding of the behavior of the structure and its parts.

There is a general technique for designing coupled resonator filters in the sense that

it can be applied to any type of resonator despite its physical structure. The coupling theory for coupled resonator circuits was developed extensively in [72] by Hong and Lancaster. The technique has already been applied to a variety of electromagnetic filters such as waveguide filters, dielectric resonator filters or microstrip filters. In this chapter, the basics of the technique will be reviewed for their application to CRFs. The design process will take into account the particularities of BAW technology which presents a particular case of resonator and operates in both the electrical and mechanical fields. The coupling theory will also provide a deep understanding of the behavior of the filter structure.

The coupling theory is very useful for the design of coupled resonator circuits, in particular the narrow-band bandpass filters. This design approach is based on coupling coefficients of inter-coupled resonators and the external quality factors of the input and output resonators. The procedure to obtain the couplings and the external quality factors to fulfill a set of specifications implementing advanced filtering responses is based on the coupling matrix. The coupling matrix gathers all the possible couplings in a coupled resonator filter. The full process to obtain the coupling matrix is described in [76]. In this chapter, the relationships between the coupling matrix and the transmission and reflection responses of filters will be established, as well as the relationships between the coupling matrix and the coupling between resonators and the external quality factors. Appendix B briefly reviews the principles of the coupling matrix generation and presents the program that was developed in MATLAB software in this work for this purpose.

The most common and extended CRF topology will be analyzed and its synthesis methodology will be presented. This topology consists of two identical basic CRF stages electrically connected by the electrodes of the lower resonators and having the input and the output at the upper resonators. The performance limits of this topology in terms of bandwidth and return losses will be presented from the analysis of the structure and using the coupling theory. The equivalent electrical model for a CRF presented in Chapter 3 will be the enabling tool to understand the behavior of the different parts of the structure. The Mason model presented in Chapter 2 will be the tool used to simulate any multilayered structure that arises from the filter design steps and any final filter structure.

Then, the synthesis technique will be extended in order to obtain advanced responses based on CRFs. In this work, the advanced responses considered refer to fil-

tering responses with transmission zeros to increase the selectivity of the filter. Three topologies with improved selectivity will be presented: parallel connected CRFs, CRFs in folded canonical configuration and parallel connected SCFs.

## 4.1 Coupling Matrix of Coupled Resonator Circuits

### 4.1.1 The $N + 2$ Coupling Matrix

A nodal representation of a filter network is shown in Fig. 4.1 where the different types of couplings are drawn. Each filled node represents a resonator of the filter, where there is a total of  $N$  resonators. An empty node represents a source or load port. The coupling between resonators is represented by means of a line of union between nodes. The coupled resonator circuit can be represented by means of the coupling matrix in 4.1. That is known as the normalized  $N+2$  coupling matrix  $\mathbf{M}$ .

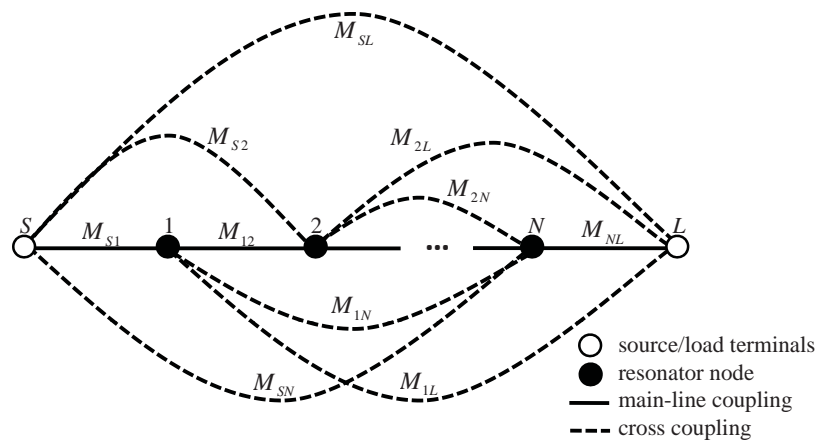


**Figure 4.1:** Nodal representation of a multicoupled resonator network.

$$\mathbf{M} = \begin{bmatrix} M_{SS} & M_{S1} & M_{S2} & M_{S3} & \cdots & M_{SN} & M_{SL} \\ M_{S1} & M_{11} & M_{12} & M_{13} & & M_{1N} & M_{1L} \\ M_{S2} & M_{12} & M_{22} & M_{23} & & M_{2N} & M_{2L} \\ M_{S3} & M_{13} & M_{23} & M_{33} & & M_{3N} & M_{3L} \\ \vdots & & & & \ddots & & \vdots \\ M_{SN} & M_{1N} & M_{2N} & M_{3N} & & M_{NN} & M_{NL} \\ M_{SL} & M_{1L} & M_{2L} & M_{3L} & \cdots & M_{NL} & M_{LL} \end{bmatrix} \quad (4.1)$$

The order of the matrix is  $N+2$  and the order of the filter is  $N$ . If the coupling

is between sequentially numbered nodes  $M_{i,i+1}$  and also  $M_{S,1}$  and  $M_{N,L}$ , it is referred to as *mainline coupling*. The elements of the main diagonal  $M_{i,i}$  are the *self-couplings* and they basically involve a resonance frequency of the resonator  $i$  different from the center frequency of the filter  $f_0$ . The self-couplings are only  $M_{i,i} \neq 0$  for asymmetric response filters. The rest of the couplings between nonsequentially numbered nodes are *cross-couplings*.

The passive network presents the property of reciprocity  $S_{21} = S_{12}$  and then the coupling matrix is symmetrical regarding the main diagonal  $M_{ij} = M_{ji}$ . In the case of all-pole synchronous filters, without transmission zeros in the stopbands, its elements are all equal to zero except those in the first two subdiagonals  $M_{i,i+1}$ .

The impedance matrix of the network can be calculated from the  $N+2$  coupling matrix [72]:

$$\mathbf{z} = \mathbf{R} + j(\mathbf{M} + \mathbf{W}) \quad (4.2)$$

where  $\mathbf{R}$  is the termination  $N+2$  impedance matrix which contains the normalized source and load impedances in the  $R_{SS}$  and  $R_{LL}$  positions and all the other entries are zero:

$$\mathbf{R} = \begin{bmatrix} R_S & 0 & 0 & \cdots & 0 \\ 0 & 0 & & & \\ 0 & & \ddots & & \\ \vdots & & & \ddots & 0 \\ 0 & & & 0 & R_L \end{bmatrix} \quad (4.3)$$

and  $\mathbf{W}$  is the lowpass prototype frequency variable matrix with elements different than 0 only in its diagonal:

$$\mathbf{W} = \begin{bmatrix} 0 & 0 & 0 & \cdots & 0 \\ 0 & \omega & & & \\ 0 & & \ddots & & \\ \vdots & & & \omega & 0 \\ 0 & & & 0 & 0 \end{bmatrix} \quad (4.4)$$

The admittance matrix can be obtained from the inverse of impedance matrix:

$$\mathbf{y} = \mathbf{z}^{-1} \quad (4.5)$$

The transmission response can be calculated from the elements of the admittance matrix  $y_{N+2,1}$ ,  $y_{11}$  and  $y_{N+2,N+2}$  as follows:

$$S_{21} = 2\sqrt{R_S R_L} y_{N+2,1} \quad (4.6)$$

and the reflection responses:

$$S_{11} = 1 - 2R_S y_{11} \quad (4.7)$$

$$S_{22} = 1 - 2R_L y_{N+2, N+2} \quad (4.8)$$

and for symmetrical networks  $S_{11} = S_{22}$ .

In this way, a coupled resonator filter has an associated coupling matrix that provides a determined filter response. The synthesis of the  $N+2$  coupling matrix from polynomial functions that implement a desired response can be found in [77]. The  $N+2$  coupling matrix is an extension of the  $N \times N$  coupling matrix that can be found in [78] and [79]. The advantages of the  $N+2$  coupling matrix regarding the  $N \times N$  coupling matrix are: 1) Multiple couplings between resonators and source or load can be accommodated (e.g.  $M_{S1}$ ,  $M_{S2}$ ,  $M_{1L}$ ,  $M_{2L}, \dots$ ). 2) Fully canonical functions can be implemented, that is  $N$  degree filters with  $N$  transmission zeros. And 3) it makes some synthesis processes that make similarity transforms easier.

The topology of the  $N+2$  coupling matrix  $\mathbf{M}$  that emerges from the synthesis procedure is called the transversal topology. However, it may be necessary to apply a further series of rotations or similarity transforms to the matrix, to transform it into a more convenient or more practical form for the application in hand. The use of similarity transforms ensures that the eigenvalues and eigenvectors of the matrix  $\mathbf{M}$  are preserved, to such an extent that under analysis, the transformed matrix will yield exactly the same transfer and reflection characteristics as the original matrix. Two specific topologies will be taken into account to implement advanced responses with CRFs: 1) the folded canonical and 2) the parallel connected topology.

For further information about the coupling matrix, the reader is referred to [76].

#### 4.1.2 Relationships between Coupling Matrix Elements and External Quality Factors, Coupling Coefficients and Resonance Frequencies

Once the coupling matrix has been synthesized, suitable parameters characterizing the filter in the original band-pass frequency domain must be evaluated. Microwave filter designers are usually more familiarized with the external quality factor  $Q_e$  and the coupling value  $k$  to express the coupling levels between a port and a resonator and between two resonators respectively. Those parameters can be seen as a way of representing the couplings of the coupling matrix in a frequency denormalized way.

The relationships between the external quality factor and the elements of the coupling matrix are [80]:

$$Q_{e,Sk} = \frac{1}{M_{Sk}^2 W} \quad (4.9)$$

$$Q_{e,kL} = \frac{1}{M_{kL}^2 W} \quad (4.10)$$

where  $k$  is the index of the considered resonator connected to the source or load port and  $W$  is the relative bandwidth.

The relationship between the coupling value  $k$  and the elements of the coupling matrix is [80]:

$$k_{i,j} = WM_{i,j} \text{ with } i \neq j \quad (4.11)$$

The elements in the diagonal of the coupling matrix  $M_{ii}$  produce a shift in the resonance frequency in the denormalized resonators [80]:

$$f_{0i} = f_0 \left( \sqrt{\left( \frac{M_{ii}W}{2} \right)^2 + 1} - \frac{M_{ii}W}{2} \right) \quad (4.12)$$

### 4.1.3 Extraction of Coupling Coefficients and External Quality Factors

Once the denormalized bandpass coupling parameters are obtained for the desired filtering characteristic, a relationship between the value of every required coupling coefficient and the physical structure of coupled resonators must be established. In this way, the physical dimensions of the filter for fabrication can be obtained.

In order to measure the coupling value  $k$  between resonators, they are decoupled from the rest of the filter network, see Fig. 4.2(a), and the transmission response is measured. Fig. 4.2(b) shows a typical transmission response obtained from two coupled resonators. Two resonances are present in the response located at the resonance frequencies  $f_{p1}$  and  $f_{p2}$ . When the resonators interact, the coupling effect splits the original resonances of a single resonator. The coupling coefficient for synchronous resonators, which both of them resonate at the same frequency  $f_0$ , can be calculated from the resonances frequencies  $f_{p1}$  and  $f_{p2}$  [72]:

$$k = \pm \frac{f_{p2}^2 - f_{p1}^2}{f_{p2}^2 + f_{p1}^2} \quad (4.13)$$

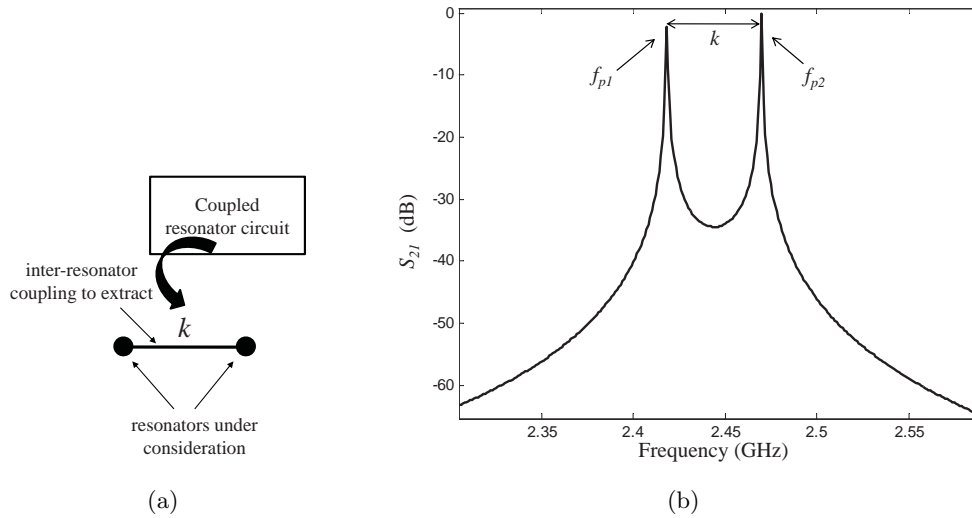


**Figure 4.2:** (a) Two resonators and their coupling are treated independently to extract the coupling value. (b) Transmission response of the two coupled resonators with their ports decoupled.

and for asynchronous resonators, which independently resonate at different frequencies  $f_{01}$  and  $f_{02}$  [72]:

$$k = \pm \frac{1}{2} \left( \frac{f_{02}}{f_{01}} + \frac{f_{01}}{f_{02}} \right) \sqrt{\left( \frac{f_{p2}^2 - f_{p1}^2}{f_{p2}^2 + f_{p1}^2} \right)^2 - \left( \frac{f_{02}^2 - f_{01}^2}{f_{02}^2 + f_{01}^2} \right)^2} \quad (4.14)$$

The external quality factor can be extracted from the response of the resonators connected to the ports. In this case the considered port and resonator are decoupled from the rest of the network (see Fig. 4.3(a)) and the reflection response  $S_{11}$  is measured. Then, the  $Q_e$  can be extracted by means of different ways. It can be calculated from the absolute bandwidth between the  $\pm 90^\circ$  points of the phase of  $S_{11}$ ,  $\Delta\omega_{\pm 90^\circ}$  [72]:

$$Q_e = \frac{\omega_0}{\Delta\omega_{\pm 90^\circ}} \quad (4.15)$$

Alternatively, the  $Q_e$  may be extracted from the group delay of  $S_{11}$  at resonance [72]:

$$Q_e = \frac{\omega_0 \tau_{S_{11}}(\omega_0)}{4} \quad (4.16)$$

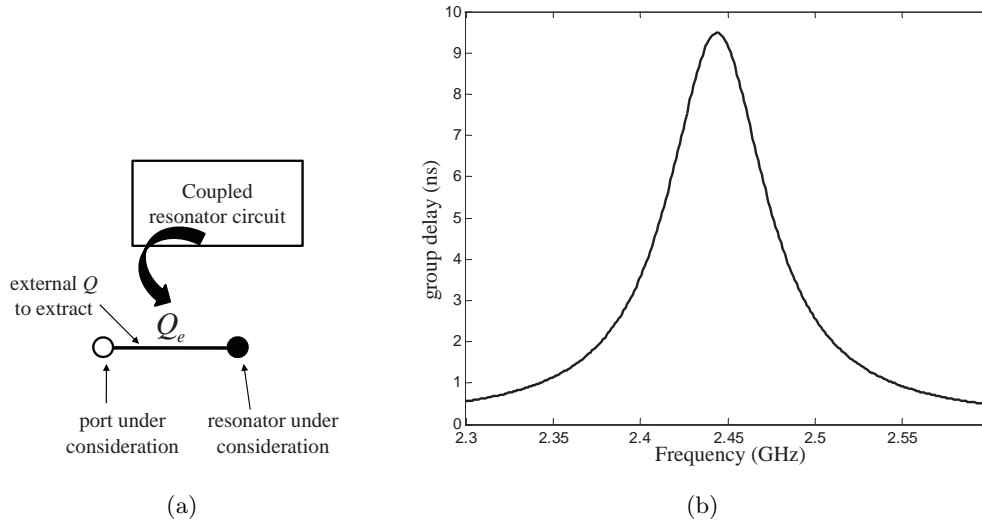


**Figure 4.3:** (a) A resonator connected to a port and their coupling are treated independently to extract the external quality factor. (b) Group delay response of  $S_{11}$ .

where  $\tau_{S_{11}}$  is the group delay of  $S_{11}$ . Fig. 4.3(b) shows a typical response of the group delay of  $S_{11}$  where the maximum value takes place at its resonance frequency  $f_0$ .

For further knowledge about the extraction of coupling coefficients and external quality factors, the reader is referred to [72].

## 4.2 The Coupling Technique in Bulk Acoustic Wave Coupled Resonator Filters

In this section, the coupling technique presented in section 4.1 is applied to the particular case of a CRF. The theory of couplings can involve complex multilayered thin film structures because it can be applied to any type of resonator despite its physical structure. It is highly advantageous for BAW filters composed of an elevated number of layers.

To exemplify the process, one of the most used CRF configurations is considered. It consists of 2 basic CRF stages connected in series by their lower resonators, while the upper resonators are the input and output ports as shown in Fig. 4.4(a). Although no external elements are included in the BAW structure in this analysis, they could be added and the analysis procedure would be identical. Source and load impedance  $Z_0=50 \Omega$  is considered as well as a symmetrical Chebyshev filter response which will

result in a symmetrical filter structure. In this way, the two CRF single stage stacks are identical and can be processed at the same time. Nevertheless, any asymmetrical filter structure could be implemented with the proposed approach.

This configuration corresponds to a mainline type because it is composed exclusively of mainline couplings as described in subsection 4.1.1. The nodal diagram is represented in Fig. 4.4(b). Its performance is analyzed in such a way that the resonance and coupling mechanisms involved in the filtering process are identified and interpreted below a general filter synthesis procedure. The analysis, assuming the fundamental mode of operation of BAW devices, is interpreted by means of the electrical equivalent circuit of the device and a suitable arrangement of the network to obtain a circuit composed of series LC resonators and impedance inverters in order to identify a bandpass filter topology. The relationships established between the electrical equivalent model and the physical device explain how the different parts of the structure contribute to the operative filter mechanisms which have both a mechanic and an electric origin.

Once the resonance and coupling mechanisms are identified, the design filter steps to obtain an arbitrary Chebyshev filter response based on the filter coupling theory are presented. Furthermore, each design step is related to one coupling mechanism in the CRF and it determines the operational limits of the involved coupling in terms of return losses and bandwidth. The combined constraints of all the couplings present in the structure set the limits on the response that can be achieved with the CRF.

### 4.2.1 Electrical Equivalent Circuit

The electrical equivalent circuit of the whole CRF considered is shown in Fig. 4.4(c) and it is obtained by cascading the electrical equivalent model of two CRF basic stages which were presented in Chapter 3, taking into account that both the upper and the lower resonators can be composed of different thicknesses and/or layer configuration. The capacitance between electrodes in the input and output upper resonators is modeled by the capacitor  $C_{01}$  and the capacitance of the lower resonator by the capacitor  $C_{02}$ . The set of coupling layers placed between the BAW resonators in both stages are modeled by means of an impedance inverter of value  $K$ .

The resonance that is produced in the BAW resonators in the mechanical field is modeled by means of the series LC resonator with values  $L_1$  and  $C_1$  for the upper

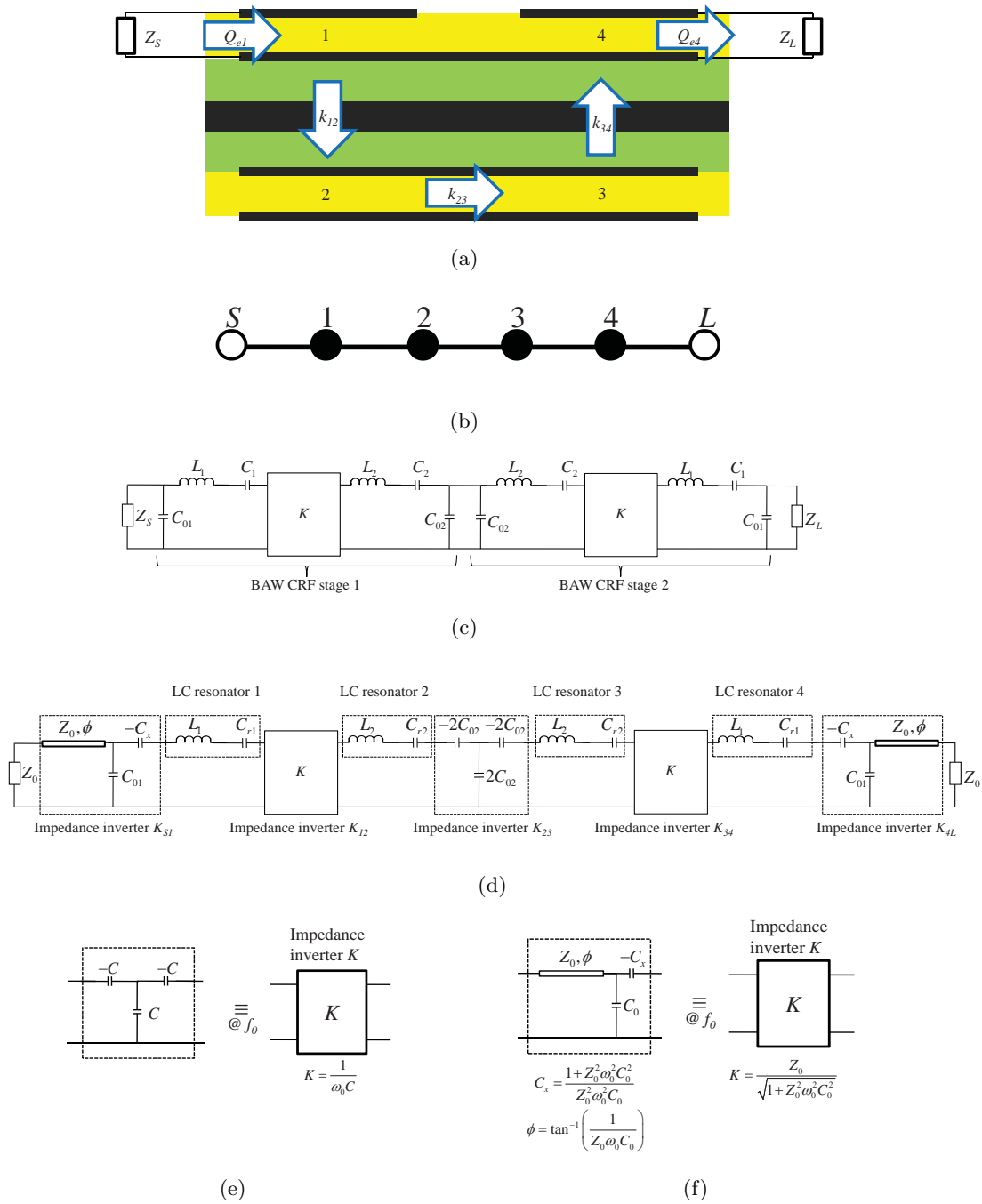


**Figure 4.4:** (a) CRF structure of order 4 and set of couplings that take place. (b) Nodal representation of a bandpass filter of order 4 in mainline configuration. (c) Equivalent electrical circuit composed of two cascaded CRF basic stages. (d) Reconfigured network to identify the coupling and resonance mechanisms. (e) and (f) impedance inverter equivalences.

resonators and  $L_2$  and  $C_2$  for the lower resonators.

Fig. 4.4(d) shows the resulting network after some network arrangements on the circuit of Fig. 4.4(c). The network has been reconfigured to obtain an impedance inverter based bandpass filter prototype of order 4. This network provides a clear identification of impedance inverters and LC series resonators that present a pure coupling and resonance behavior respectively.

It is well-known that a T of capacitors can implement an impedance inverter as shown in Fig. 4.4(e) [72], and it was demonstrated in Chapter 3 by means of ABCD matrixes that a transmission line, a shunt capacitor and a series negative capacitor with proper values can also implement an inverter as shown in Fig. 4.4(f). Note that in a mainline configuration such as the topology that is being managed, the transmission line element is added to help the analysis which only entails a phase shift and does not affect either the magnitude of the transfer response or the group delay of the filter. That happens because the impedance of the transmission line is the same as the port at which it is connected.

The impedance inverters in the circuit in Fig. 4.4(d) are formed by two series capacitors with the same value and opposite sign. They have been used in such a way that the negative capacitor is part of the inverter and the positive capacitor modifies the center frequency of the adjacent LC resonator. In the case of the input and output inverters,  $K_{S1}$  and  $K_{4L}$  respectively, the negative capacitor  $-C_x$  becomes part of the formed inverter and the positive capacitor  $C_x$  modifies the resonance by means of the final capacitance of the LC series resonator  $C_{r1} = (C_1^{-1} + C_x^{-1})^{-1}$ . In the case of the inverter  $K_{23}$ , the negative capacitors  $-2C_{02}$  are part of the inverter and the series positive capacitors  $2C_{02}$  modify the resonance of the adjacent LC series resonators by means of  $C_{r2} = (C_2^{-1} + (2C_{02})^{-1})^{-1}$ . Note that the use of series capacitors with the same value and opposite sign does not change the circuit behavior but only the topology representation.

It is also important to note that at this point two kinds of resonators must be distinguished: the physical BAW resonators and the effective series LC resonators. The effective resonators can be directly related to those in a bandpass prototype filter composed of impedance inverters and they provide the effective resonance that is produced in the CRF. Although there is no doubt that mechanical resonances are produced inside the structure, the effective resonances that take place in the filter are not exclusively

mechanical in origin. The effective resonance consists of a contribution of both the mechanical and electrical fields. The BAW resonator is *de facto* a loaded resonator which includes resonance behavior and coupling behavior. The coupling behavior comes from the intrinsic capacitance of the resonator which has an electrical origin. The fact that a BAW resonator does not present pure resonance behavior leads to, when it forms part of a filter structure, part of the resonator being included inside the coupling elements (impedance inverters) and part of the resonator being included inside the resonance elements (LC resonators). The intrinsic electrical capacitance contributes to the effective resonance frequency modifying the pure acoustic resonance. This phenomenon is well modeled in the series negative-positive resonators.

#### 4.2.2 Analysis and Design of a CRF

In this section, a complete design of a conventional 4-degree CRF is carried out using the coupling theory. The design problem can be split into several independent steps corresponding to the different couplings involved in the structure, and are labeled in Fig. 4.4(a): the coupling between the source and load ports to the input and output resonators respectively ( $Q_{e1}$  and  $Q_{e4}$ ), the coupling between the lower resonators which takes place by means of a direct electric connection ( $k_{23}$ ) and the pure acoustic coupling between the upper and the lower resonators which takes place by means of the set of coupling layers ( $k_{12}$  and  $k_{34}$ ).

The design output variables are the geometries of the device in terms of the thicknesses of the layers and active area of the device. The design inputs are the configuration of the layers, their material parameters (e.g. dielectric permittivity, mechanical impedances, velocities, piezoelectric constants) and the filter specifications. The configuration of the layers refers to the predefined sequence of materials that will implement the stack of the structure.

The design will be carried out by means of the Mason model which gathers all the design variables for any complex multilayered thin film structure. It is important to emphasize that although the design process is carried out by means of the Mason model, the equivalent electrical circuits presented above help to understand how to apply the Mason model in each design step. For that reason, each step will show the Mason model as a simulation tool and the equivalent electric circuit that describes the filter elements that are taken into account.

During the design process, an analysis of the different parts of the structure is carried out. Its aim is to establish their contribution and limits to the overall filter response. The design procedure is carried out in 3 steps that can be summarized as follows:

1. *Sizing of the active area of each CRF and the piezoelectric thickness of the input and output BAW resonators (resonators 1 and 4) to fulfill the required  $Q_e$ .* In this step, the area is used to obtain the desired  $Q_e$ . The piezoelectric thickness is used to center the resonance frequency of the effective resonator  $L_1C_{r1}$  to the center frequency,  $f_0$ , of the filter response. The electrode thicknesses are assumed to be an input parameter in the design process. Note that they could be optimized to maximize the electro-mechanical coupling in the case of stringent filter requirements in terms of return losses or bandwidths. In any case, most important is that this step is carried out with any kind of resonator configuration regardless of the additional layers that form it and their function.
2. *Sizing of the piezoelectric thickness of the lower resonators (resonators 2 and 3) and their electrode thickness to fulfill the required coupling  $k_{23}$ .* It is important to point out that the active area has been already defined in the previous step and it is not used as a design variable in this step because it does not affect the coupling value between resonators 2 and 3. A suitable combination of the piezoelectric and electrode thickness centers the resonator at the center frequency of the filter and fulfills the coupling value at the same time by means of a direct connection of the lower resonators without the necessity of adding external elements. Note that in this case, the degree of freedom provided by the electrode thickness is necessary here.
3. *Sizing of the coupling layers' thicknesses to fulfill  $k_{12}$  ( $k_{34}=k_{12}$ ).* The thickness of the coupling layers is calculated in such a way that the set of layers implements an impedance inverter that provides the desired degree of acoustic coupling between the upper and the lower resonators defined in the previous steps. Typically, the set of coupling layers is composed of one layer of high acoustic impedance material such as W between two layers of low acoustic impedance material such as SiO<sub>2</sub>.

These design steps are detailed below. To exemplify the design process, a CRF formed by resonators composed of a piezoelectric plate of AlN and electrodes of W

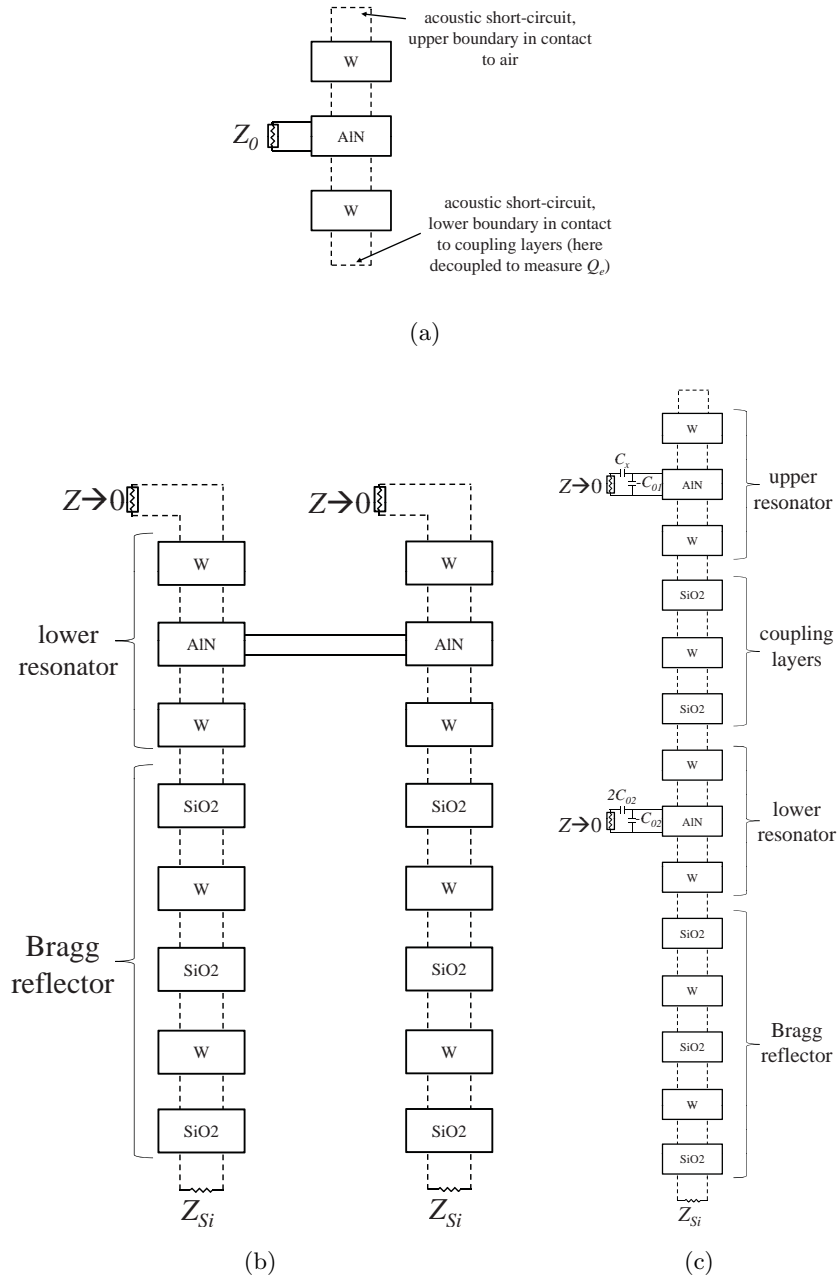


**Figure 4.5:** Simulation circuits implemented with the Mason model to calculate the couplings that take place in the CRF of order 4. Discontinuous lines refer to acoustic connections between acoustic ports and continuous lines refer to electric connections between electric ports. Note that boxes for piezoelectric plates are composed of 3 ports of the Mason model (2 acoustic ports and 1 electric port) while non-piezoelectric plates are composed of 2 acoustic ports. (a) Circuit to obtain the external quality factor  $Q_e$ , (b) the coupling between the lower resonators  $k_{23}$  and (c) the coupling between an upper and a lower resonator  $k_{12}$ .

**Table 4.1:** Requirements for the example filter and associated couplings

Passband frequency range	2.40-2.48 GHz
Relative bandwidth	3.28 %
Center frequency	2.44 GHz
$Z_S=Z_L$	50 $\Omega$
RL	15 dB
$Q_{e1}=Q_{e4}$	36.5
$k_{12}=k_{34}$	0.026
$k_{23}$	0.021

and a set of 3 coupling layers of SiO<sub>2</sub>/W/SiO<sub>2</sub> has been considered. The properties of the considered materials can be found in Appendix A. The resulting filter can be implemented using a SMR or FBAR technology approach. In this example, the SMR option has been chosen because it presents some peculiarities that must be taken into account during the design process. First, the electrode thickness of the upper resonators will be considered an input parameter and later, a study will be carried out to show how a suitable choice of its thickness may be useful to implement stringent specifications.

Table 4.1 summarizes the filter specifications for this example working at a WiFi band and the associated required couplings obtained by applying (4.9) and (4.11). The values of the normalized couplings of the coupling matrix can be obtained following the design procedure explained in [76]:  $M_{S1}=M_{4L}=0.9146$ ,  $M_{12}=M_{34}=0.8021$  and  $M_{23}=0.6426$ .

**Step 1. External quality factor** The aim of this step is to obtain an active area and thicknesses of the piezoelectric layers that fulfill the required  $Q_e$ . In order to measure the  $Q_e$ , a practical simulation can be performed as shown in Fig. 4.5(a), where the BAW resonator 1 can be simulated by means of the Mason model. Note that at this point, any layer stack that forms the resonator can be taken into account. Regardless of the complexity of its configuration, the resonator is treated in the same way. Electrodes composed of multiple materials, passivation layers or other layers designed to solve other questions are assumed to form part of the resonator. Any effect caused by the layers would therefore be included.

The calculation of the  $Q_e$  is carried out using (4.16) from the electric port while the acoustic ports of the BAW resonator are acoustically short-circuited according to its electrical analog schematic in Fig. 4.6. Note that the simulation circuit in Fig. 4.5(a)

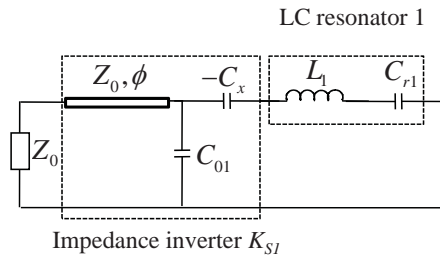


**Figure 4.6:** Electrical equivalent circuit for the  $Q_e$  measurement

corresponds to its analog in Fig. 4.6.

The electrical analog schematic includes: the series resonator, in this case formed by  $L_1$  and  $C_{r1}$ , and the impedance inverter which couples the port and the resonator. The resonator must be decoupled from the rest of the network by means of a short-circuit which induces its resonance behavior.

The dimensions of resonator 1 must be determined in order to obtain a simulated  $Q_e$  from (4.16) that is the same as the required  $Q_e$  in (4.9) and given in Table 4.1. Both the variation of the area of the resonator and the variations in thickness of the layers involved lead to variations in the resonance frequency and the  $Q_e$ .

For the sake of simplicity, in this example, a thickness of  $t_e=200$  nm for the electrodes is assumed. Fig. 4.7 shows the curve of the resonator external quality factor for each value of its active area expressed by means of the side–length of a square–shaped area as reference. This curve has been calculated in such a way that for each value of the active area, the piezoelectric thickness is determined to have the effective resonance (formed by  $L_1C_{r1}$ ) centered just at the center frequency of the filter  $f_0$ . Note that a change in the area of the resonator leads to a change in the effective resonance frequency of the resonator because when the intrinsic capacitance forms the coupling element (the impedance inverter), it modifies the resonance frequency of the effective resonator, and in this way, the effective resonance does not only depend on the mechanical resonance generated inside the layers of the resonator stack.

The curve presents a minimum value for the external quality factor,  $Q_{e,min}$ , which represents the maximum coupling value between the source and the input resonator. According to (4.9) the maximum bandwidth that can be achieved for prescribed RL is

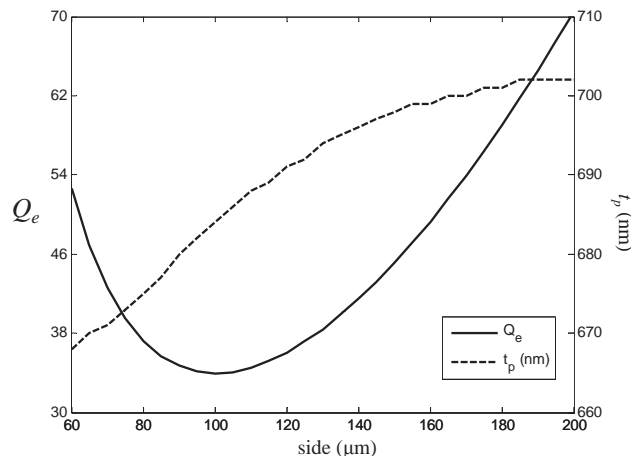


**Figure 4.7:** External quality factors versus the active area of the BAW resonator for an electrode of W and thickness of 200 nm and the corresponding AlN piezoelectric plate thickness to place the effective resonance at the center frequency of the filter  $f_0$ .

given by

$$W_{max} = \frac{1}{M_{S1}^2 Q_{e,min}} \quad (4.17)$$

or, alternatively, the maximum theoretical RL that can be achieved for a given bandwidth can be determined.

For this design example, two possible side length solutions, 82.5  $\mu\text{m}$  and 122  $\mu\text{m}$ , can be chosen to fulfill the required  $Q_e=36.5$ . The minimum side length solution has been chosen to minimize the consuming area of the device while the thickness mode ratio was acceptable.

Nevertheless, if more stringent specifications were required in terms of RL or the RL for the required passband had to be maximized, the electrode thickness could play an important role in minimizing the  $Q_{e,min}$ . In other words, a higher RL requires a higher coupling which implies a smaller  $Q_e$ . Note that a higher RL will also imply a lower selectivity of the response and therefore, it is generally convenient to obtain a balance between RL and selectivity. For any electrode thickness combination, a new curve  $Q_e$  vs side-length can be generated and so a new  $Q_{e,min}$  is associated. There is therefore an electrode-piezoelectric thickness combination that produces the minimum  $Q_{e,min}$ . This external coupling takes place when the effective piezoelectric coupling constant,  $k_{eff}^2$ , is maximized providing the best transduction between the electric and the mechanical fields for the structure and at the same time the area is properly chosen

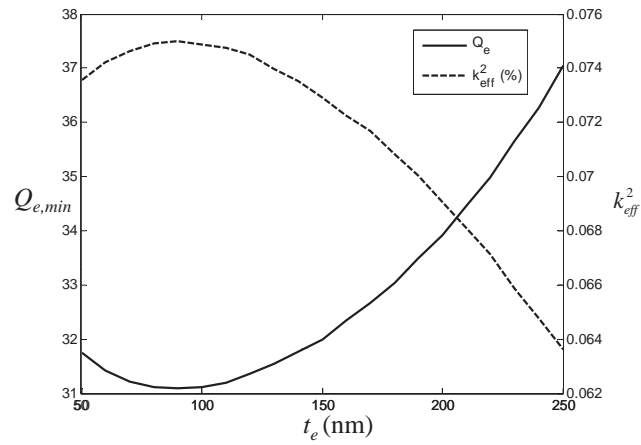
to also maximize the coupling.

Fig. 4.8(a) shows the  $Q_{e,min}$  and the related  $k_{eff}^2$  that can be achieved for any electrode thickness. The piezoelectric thickness is calculated for each situation to make the resonator resonate at the center frequency of the filter. Note here that, as predicted, the maximum  $k_{eff}^2$  takes place at the same point as the minimum  $Q_{e,min}$ . It is evident that by relaxing the RL requirements higher bandwidths can be implemented for the same BAW resonator configuration. Thanks to these curves the limits of the response that the input/output BAW resonator provides can be explored. Fig. 4.8(b) shows the maximum bandwidth that can be achieved for any resonator configuration and for different specified RL. For example, maximum relative bandwidths of 3.8% can be implemented for RL=15 dB. In this way, the limits that the input/output resonators establish on the final response can be obtained for a given technology and a combination of materials for the electrodes and piezoelectric and passive composite plate.

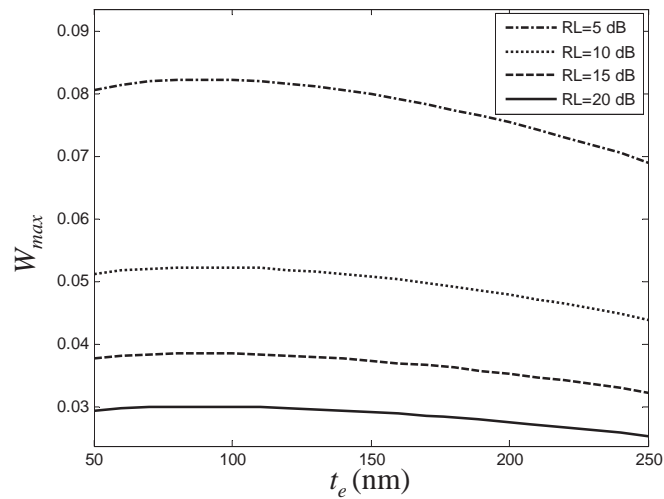
Moreover, this procedure is a useful way of analyzing how external elements such as lumped inductors can be conveniently placed at the electrical input of the resonator to get lower external quality factors and obtain higher bandwidths for a specific RL [81].

**Step 2. Coupling value between the lower resonators** The aim of this step is to obtain the piezoelectric thickness of the lower resonators and their electrode thickness to fulfill the required coupling  $k_{23}$ . A direct connection between the lower resonators is carried out and therefore, the thickness of the electrodes and the piezoelectric are the variables that enable the resonance frequency of the effective resonators to be centered and the desired level of inter-resonator coupling to be achieved. In this way, the desired coupling can be obtained without adding external elements to the BAW structure.

A practical simulation schematic circuit to obtain the coupling value between resonators 2 and 3 is shown in Fig. 4.5(b). The BAW resonators can be simulated again with the Mason model and the impedance inverter is formed implicitly in the electrical connection of both resonators. The transmission is obtained from one of the acoustic ports of the Mason model of the resonators and the remaining one is ended with the corresponding load. In the case of a SMR approach, for each resonator, one acoustic port is used as a port and the remaining acoustic port in the Mason model is loaded with the set of layers in the reflector stack including the substrate. The inter-resonator



(a)



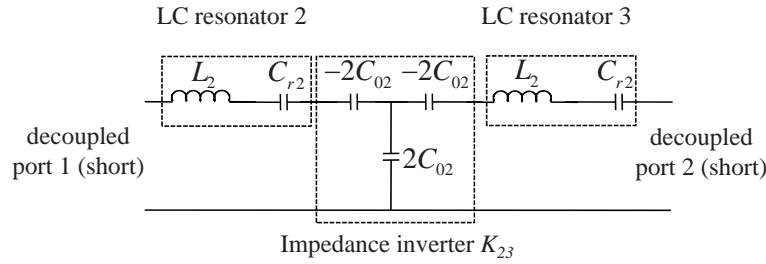
(b)

**Figure 4.8:** (a) Minimum external quality factor and the corresponding piezoelectric coupling constant that can be achieved for any BAW resonator configuration considering electrodes of W and a piezoelectric of AlN. For every electrode thickness, the piezoelectric thickness is calculated to center the resonator at  $f_0$  and the area is selected to minimize the external quality factor. (b) Maximum bandwidth that can be implemented for any BAW resonator configuration and for different RL.

**Table 4.2:** Layer thickness of the considered SMR configurations

Layers	SMR A Thickness (nm)	SMR B Thickness (nm)
SiO2	574	900
W	532	440
SiO2	574	900
W	532	440
SiO2	500	500

The uppermost layer of SiO2 has its upper boundary in contact with the lower BAW resonator and the lowermost layer of SiO2 has its lower boundary in contact with the substrate of Si.

**Figure 4.9:** Electrical equivalent circuit for the  $k_{23}$  measurement

coupling is obtained from the transmission and (4.13) that relates the resonances to the coupling value.

Fig. 4.9 shows the equivalent electrical circuit of the 2 considered coupled resonators. Note that the simulation circuit in Fig. 4.5(b) corresponds to its analog in Fig. 4.9. The coupling degree between the lower BAW resonators is controlled by means of their associated capacitance  $C_{02}$ . The measure of the coupling must take into account the two considered resonators formed by  $L_2$  and  $C_{r2}$  and the impedance inverter  $K_{23}$ . The considered block is decoupled from the rest of the network by short-circuiting the resonators. Note that in this case the short-circuit is produced in the acoustic plane. The ports from which the measure is taken are acoustic ports from the bottom BAW resonators 2 and 3; meanwhile the electric ports of those resonators are inter-connected.

Fig. 4.10(a) shows the coupling value  $k_{23}$  that is obtained for each bottom resonator configuration and the corresponding  $k_{eff}^2$  taking into account the SMR A configuration found in Table 4.2 which causes a small degradation of  $k_{eff}^2$ . The piezoelectric thickness, shown in Fig. 4.10(b), is again calculated so that each electrode thickness has the

resonance frequency of the effective resonator at  $f_0$ . It can be seen that the coupling values  $k_{23}$  are too high to implement the desired  $k_{23}=0.021$ . A situation with lower electro-mechanical coupling would be desired here, which can be accomplished with other electrode materials that present a lower  $k_{eff}^2$  such as for example Al or by means of an SMR which reduces the  $k_{eff}^2$  levels.

In this example, the latter solution has been chosen. Fig. 4.10(a) also shows the new curves for  $k_{23}$  and  $k_{eff}^2$  for the new SMR B configuration, which can be found in Table 4.2. This configuration can implement the desired coupling value with an electrode thickness of  $t_e=242$  nm and a piezoelectric thickness  $t_p=477$  nm obtained from Fig. 4.10(b).

The upper bound of the attainable bandwidth can be calculated from (4.11)

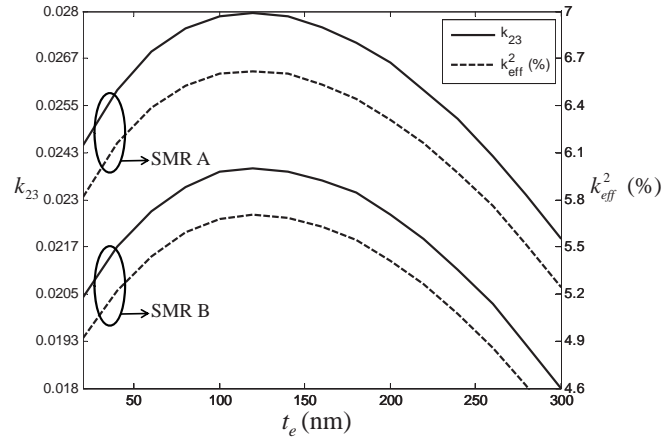
$$W \leq k_{23,\max} M_{23} \quad (4.18)$$

Fig. 4.11(a) and Fig. 4.11(b) show the bandwidths that can be implemented for either considered SMR configuration. It is shown that depending on the required RL that must be fulfilled, the coupling  $k_{23}$  can be a more limiting parameter than the source or load external coupling that occurs in the input/output resonator to source/load impedance. For the design example, where RL=15 dB are required, a maximum bandwidth of 4.35% could be implemented with the SMR A. Thus for a return loss of 15 dB the source/load external coupling is more limiting than the coupling  $k_{23}$  in terms of bandwidth. On the other hand, if configuration SMR B is used the maximum bandwidth is 3.7%, and  $k_{23}$  becomes the more limiting coupling.

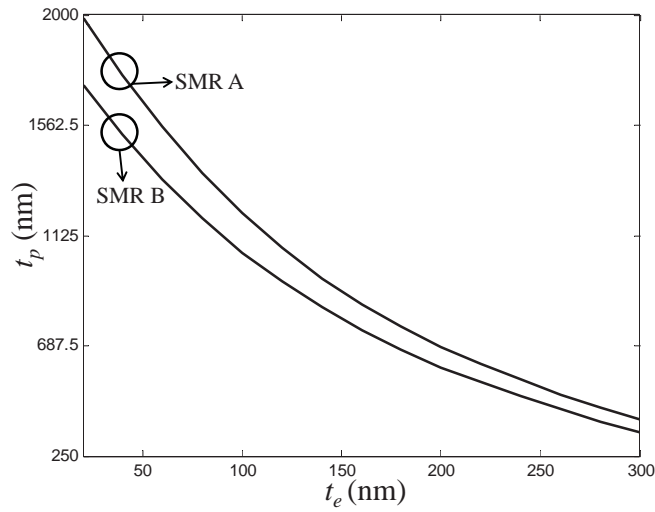
It is interesting to point out that this procedure allowed us to evaluate, for example, how an optimized SMR version devoted to confining the shear mode affects the filter response.

### Step 3. Acoustic coupling value between the upper and the lower resonator

In this step, the upper and lower resonators have been completely sized and the thicknesses of the set of coupling layers are the remaining parameters to be defined. When the set of coupling layers are properly sized, they can implement an impedance inverter by themselves as shown in Chapter 3 and the resonance of the BAW resonators will not be affected by them. Nevertheless, if they do not implement an ideal impedance

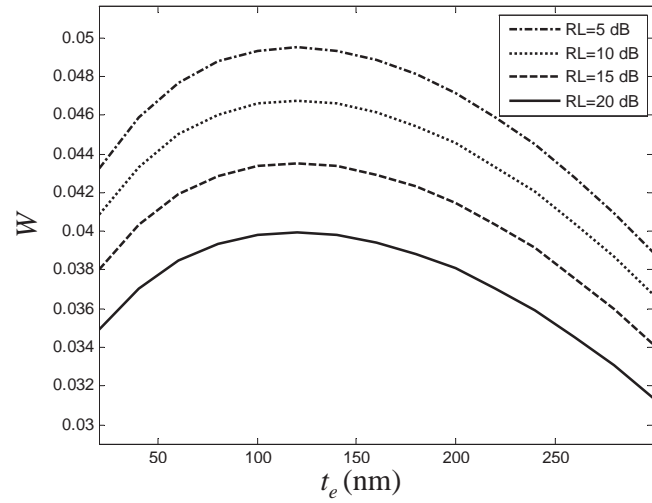


(a)

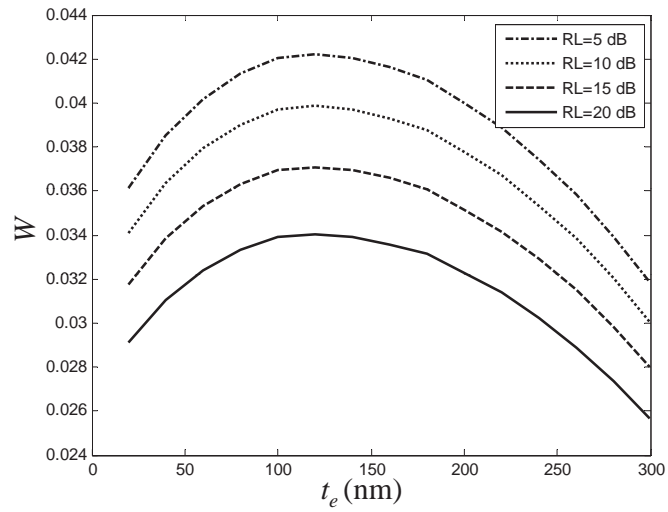


(b)

**Figure 4.10:** (a) Coupling values  $k_{23}$  and those associated for any lower BAW resonator configuration considering SMR A and SMR B and (b) the corresponding AlN piezoelectric plate thickness to place the effective resonance at the center frequency of the filter  $f_0$ .



(a)



(b)

**Figure 4.11:** (a) Bandwidths that can be implemented for any lower BAW resonator configuration considering SMR A and (b) SMR B.

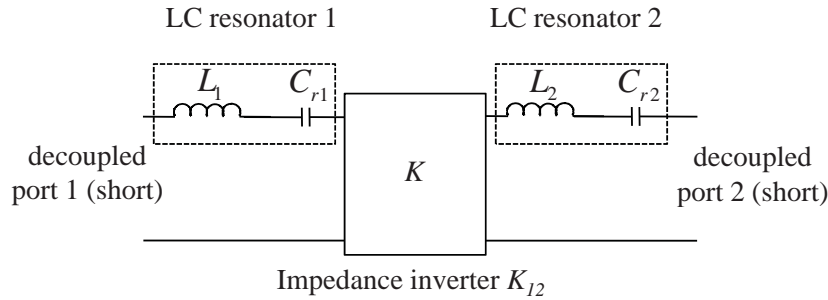


**Figure 4.12:** Electrical equivalent circuit for the  $k_{12}$  measurement

inverter by themselves, their contribution will modify the resonance frequency of the resonators by means of the added reactance. This frequency shift must be included in the model by means of series capacitors with the same value and opposite sign as shown for a single coupling layer in section 3.5.

In this case, the transmission is measured from the electric ports of the whole CRF single stage with a suitable simulation circuit at the input and output of the device as shown in Fig. 4.5(c). These circuits remove the effect of the intrinsic static capacitor formed in the BAW resonators by means of  $-C_{01}$  and  $-C_{02}$  and modify the resonance frequency to take into account the effects of the inverter formation on the effective series resonator by means of the series capacitors  $C_x$  and  $2C_{02}$ .

Fig. 4.12 shows the electrical equivalent circuit which is formed by the resonator composed of  $L_1$  and  $C_{r1}$ , the resonator composed of  $L_2$  and  $C_{r2}$  and the impedance inverter  $K_{12}$ . Note that the simulation circuit in Fig. 4.5(c) corresponds to its analog in Fig. 4.12. The frequency split that is measured in this step is perfectly centered at  $f_0$  because the two effective series resonators  $L_1C_{r1}$  and  $L_2C_{r2}$  are synchronous and have been designed in the two previous steps to resonate at  $f_0$ . When both resonators are acoustically coupled by the set of coupling layers that implement the impedance inverter, their resonances are split in frequency regarding  $f_0$ .

The required coupling value  $k_{12}=0.026$  for the design example can be obtained using an ideal impedance inverter to acoustically couple the resonators and adjusting its value to fulfill  $k_{12}$  that is calculated from the transmission response using (4.13). The value of the ideal impedance inverter is 0.023 kg/s. Then, in order to size a set of coupling layers of SiO<sub>2</sub>/W/SiO<sub>2</sub> that fulfil this inverter value, (3.44) and (3.45) of section 3.4 are used. The obtained thicknesses are 661/149/661 nm. The combination

**Table 4.3:** Layer thickness of the CRF

Structure part	Layer/boundary material	Thickness (nm)
Upper boundary	Air	-
	W	200
Upper BAW resonator	AlN	676
	W	200
Coupling layers	SiO2	661
	W	149
	SiO2	661
Lower BAW resonator	W	243
	AlN	477
	W	243
Bragg reflector	SiO2	900
	W	440
	SiO2	900
	W	440
	SiO2	500
Lower boundary	Si	-

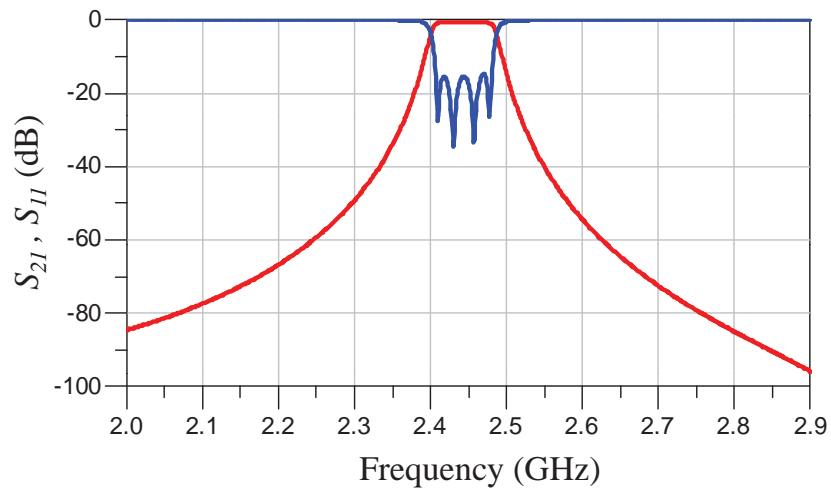
The active area of the CRF is  $82.5 \times 82.5 \mu\text{m}^2$ .

of high and low acoustic impedance layers provides a wide range of acoustic couplings  $k_{12}$ , less restrictive than the couplings presented in the previous steps.

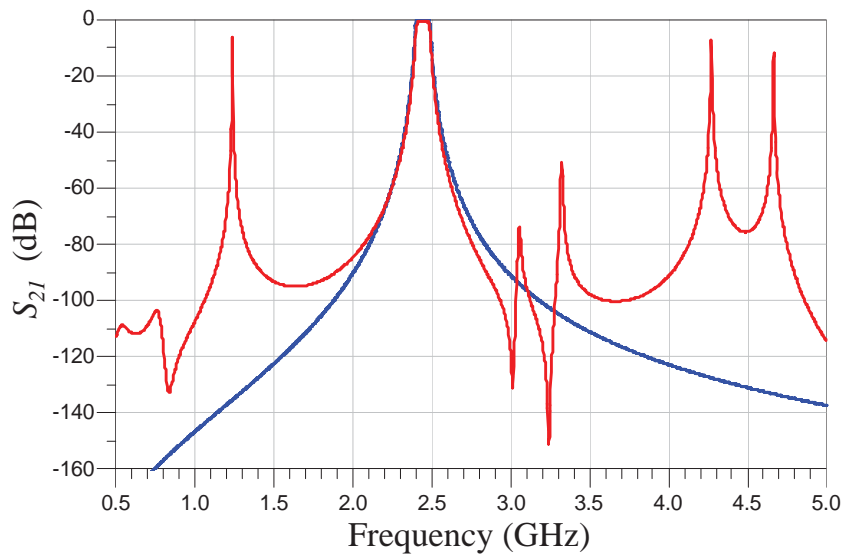
### 4.2.3 Example CRF Geometry and Response

The final geometry of the example filter is summarized in Table 4.3 where the whole stack of layers is described. Fig. 4.13(a) shows the filter response of the proposed example filter composed of two CRF basic stages connected in series.

The simulation was performed by means of the Mason model and transmission line models for the acoustic parts of the device as shown in Fig. 4.14. The simulation was performed taking into account BAW resonators with a quality factor of 1000. The response provides the required RL=15 dB and passband frequency range between 2.40-2.48 GHz. The filter selectivity coincides with a Chebyshev response of order 4 with the four poles perfectly split along the band. Fig. 4.13(b) shows the filter response in a wider frequency span compared to an ideal Chebyshev response. Spurious peaks appear far from the passband; their frequency distance to the passband is tied to the coupling layers configuration.



(a)



(b)

**Figure 4.13:** (a) Filter response of the CRF of order 4 and (b) comparison of the filter response (continuous line) to an ideal Chebyshev response (dashed line) in a wider frequency span.

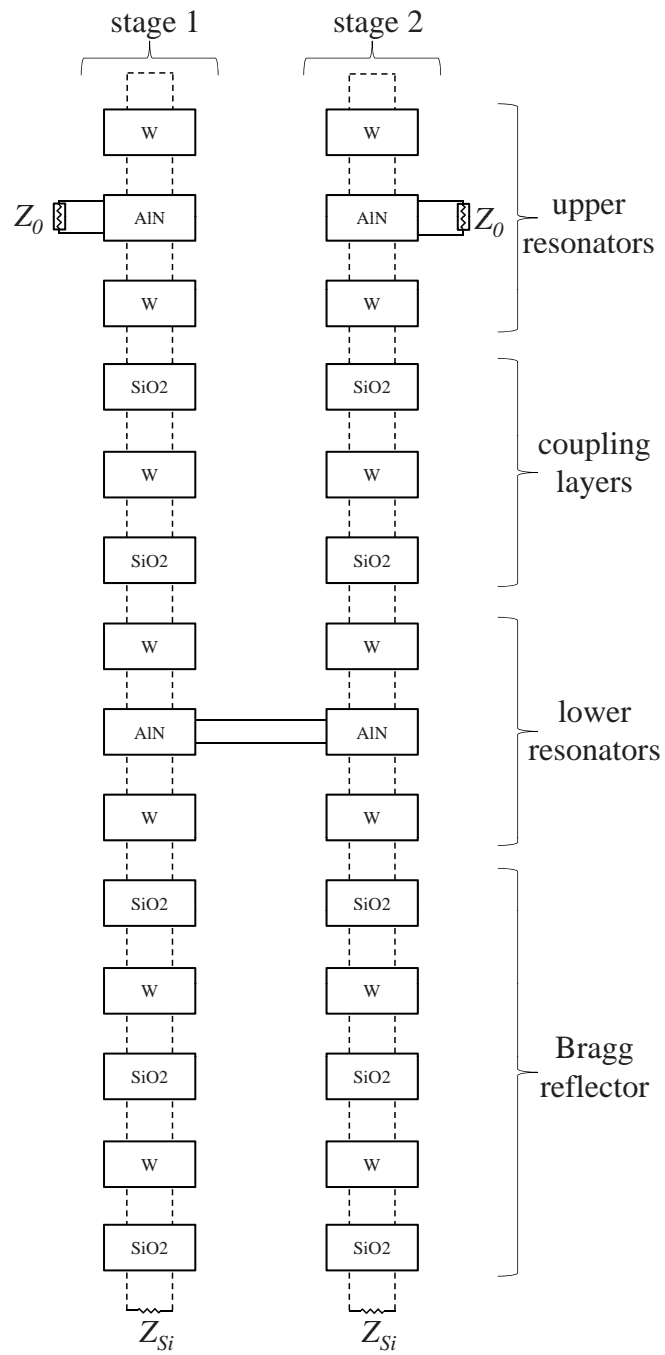


**Figure 4.14:** Circuit based on the Mason model to simulate the whole CRF of order 4.

## 4.3 Advanced Responses with CRFs

Filter responses with transmission zeros have been classically obtained by means of ladder filters in BAW technology which provide good selectivity close to the passband but poor rejection far from the passband.

A CRF single stage presents a slow roll-off outside the frequency passband, which makes it not adequate for some applications with stringent requirements that demand high near band rejection. One solution is cascading several CRF stages to improve the rejection increasing the order of the resulting filtering function. However, this solution increases the insertion loss of the resulting filter. It only uses mainline couplings between resonators and, as a result, the filtering response does not have transmission zeros.

The selectivity of a CRF can be improved using fewer stages by means of exploiting the characteristics of cross-couplings between resonators which enable the creation of transmission zeros in the response. In [51], it was demonstrated how the addition of a small capacitance between the input and the output ports can produce 2 transmission zeros to increase selectivity. That capacitance assumes the role of a cross-coupling between the source and load nodes of the filter.

This section will explain how the concept of cross-couplings in CRFs can be applied to achieve advanced filtering responses with high selectivity. These responses can be solvently synthesized by means of the coupling matrix which relates the couplings in a coupled resonator network to a prescribed filtering response.

### 4.3.1 Parallel Connected CRFs

#### Parallel Connected Topology Implemented with CRFs

The application of the coupling matrix filter design approach to CRFs provides the advantage of synthesizing topologies that are able to produce arbitrary Chebyshev responses with high selectivity by means of the allocation of transmission zeros close to the passband. In this subsection, a parallel connected configuration is presented which is composed of two CRF branches. Fig. 4.15(a) shows the nodal representation of a parallel connected configuration composed of four resonators. This configuration can be implemented by two CRFs in parallel connection taking into account some

considerations and the addition of some external support elements.

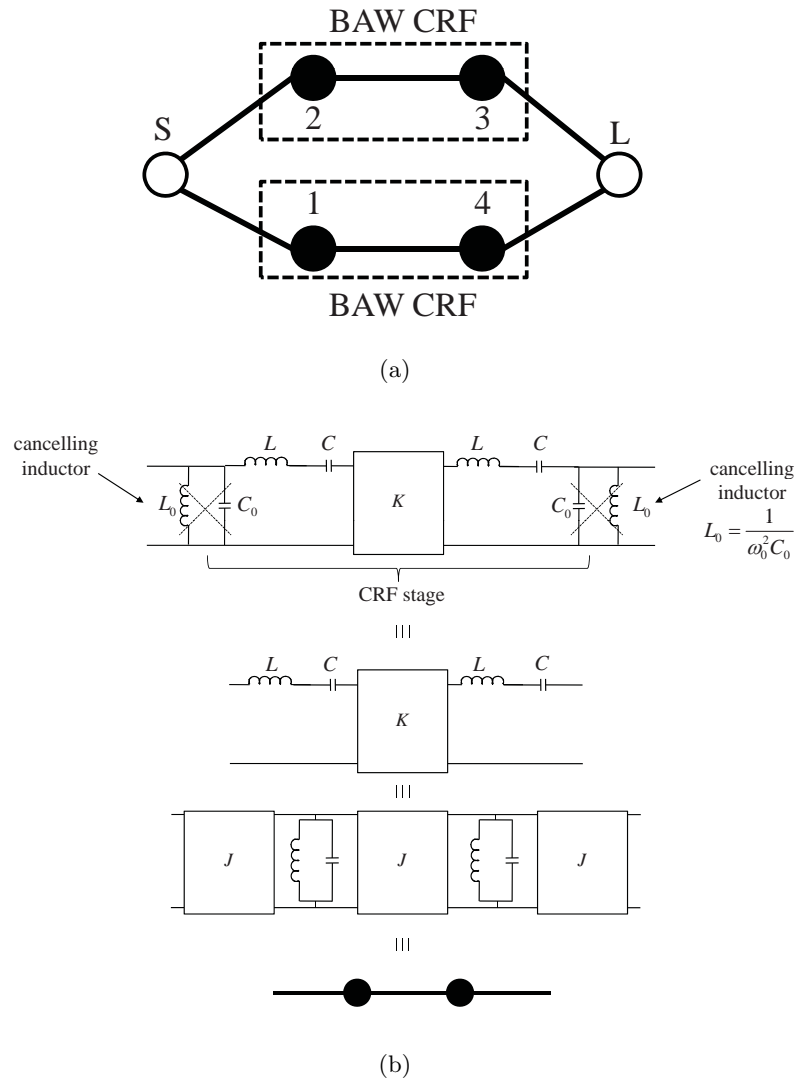


**Figure 4.15:** (a) Nodal representation of a filter network of order 4 in parallel connected configuration. (b) Equivalent networks with series and parallel resonators for a CRF when its parallel capacitors have been removed.

The CRF network is slightly modified by removing its input/output parallel capacitors. It can be done in narrow-band by the use of inductors. Fig. 4.15(b) shows how a branch of the parallel connected configuration with CRFs is implemented. Two inductors are added to the input and output ports of the CRF device to remove the static capacitors. The resulting equivalent electrical network is composed of two series LC resonators connected by means of the impedance inverter. It can be shown with

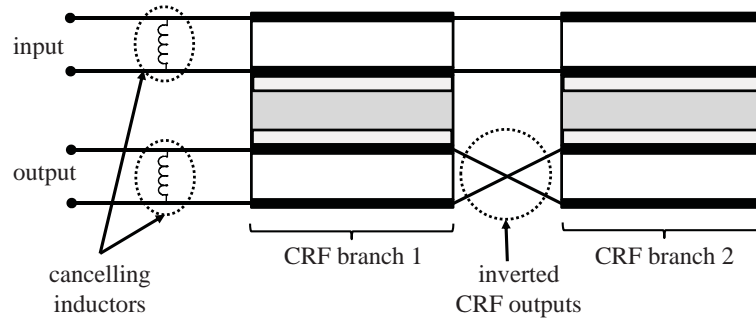


**Figure 4.16:** CRF parallel connected topology. The inverted connection at the lower resonators creates a  $180^\circ$  phase shift between branches.

ABCD matrixes that it is equivalent to a network composed of shunt LC resonators coupled by means of an admittance inverter and also with admittance inverters at the input and output of the circuit. The equivalent network implemented with shunt resonators makes up one of the branches of the topology presented in Fig. 4.15(a). Each admittance inverter is related to a coupling and the shunt LC resonators to the resonator nodes.

One of the key points in the parallel connected configuration using two parallel networks is that one of the couplings must have a negative sign while the others remain positive or viceversa. Although it can be carried out by means of the coupling layers implementing each coupler with  $90^\circ$  (positive coupling) and  $270^\circ$  (negative coupling) of phase shift respectively, the high electrical length of the acoustic coupling layers implementing the  $180^\circ$  phase shift differs too much from an ideal inverter, involving a deterioration of the general filter response, especially at the edges of the passband and out-of-band. Another option is the implementation of 2 CRFs with couplers of  $90^\circ$  and introducing an electric phase shifter of  $180^\circ$  at one of the input/output ports of one of the branches. In this way, the shifter facilitates the creation of a negative coupling. Although the response of the filter is much better than implementing the  $270^\circ$  acoustic coupling layers, there is a need to implement a phase shifter. A more compact solution that exploits the properties of the CRF device is to take the output of each CRF branch with a different polarization as shown in Fig. 4.16. In this way the couplings between the lower resonators of each CRF branch and load have a different sign.

**Table 4.4:** Requirements for the example filter with parallel connected configuration and associated couplings

Passband frequency range	2.40-2.48 GHz
Relative bandwidth	3.28 %
Center frequency	2.44 GHz
$Z_S=Z_L$	50 $\Omega$
Transmission zeros (low-pass frequency)	$\pm 4$ rad/s
Return loss	>25 dB
$Q_{e1}=Q_{e4}$	74.65
$Q_{e2}=Q_{e3}$	33.56
$k_{14}$	0.049
$k_{23}$	0.024

### Filter Design

The design procedure for parallel connected CRFs is roughly the same as in the mainline case of the previous section once the coupling matrix is obtained from the specifications. As a design example, a filter working in the same frequency band of the filter in the previous section is designed with transmission zeros in the lowpass prototype frequencies  $\pm 4$  rad/s. The transmission zeros close to the passband provide higher selectivity than conventional CRF configurations based on mainline couplings. The specifications of the filter considered in this section are summarized in Table 4.4. CRFs in FBAR technology will be assumed, that will imply that the lower resonators of the CRF will be assumed to rest on an air interface, an acoustic short-circuit.

The coupling matrix that fulfills the filter specifications is obtained following the process described in Appendix B and it is reconfigured to a parallel connected topology using the matrix reconfiguration process also described in Appendix B:

$$\mathbf{M} = \begin{bmatrix} 0 & 0.6392 & 0.9533 & 0 & 0 & 0 \\ 0.6392 & 0 & 0 & 0 & 1.4797 & 0 \\ 0.9533 & 0 & 0 & 0.7440 & 0 & 0 \\ 0 & 0 & 0.7440 & 0 & 0 & -0.9533 \\ 0 & 1.4797 & 0 & 0 & 0 & 0.6392 \\ 0 & 0 & 0 & -0.9533 & 0.6392 & 0 \end{bmatrix} \quad (4.19)$$

The matrix shows that a negative coupling must be implemented between the resonator 3 and the load. Table 4.4 shows the external quality factors and the inter-resonator couplings required to design the filter which have been obtained from the coupling matrix and (4.9) and (4.11).

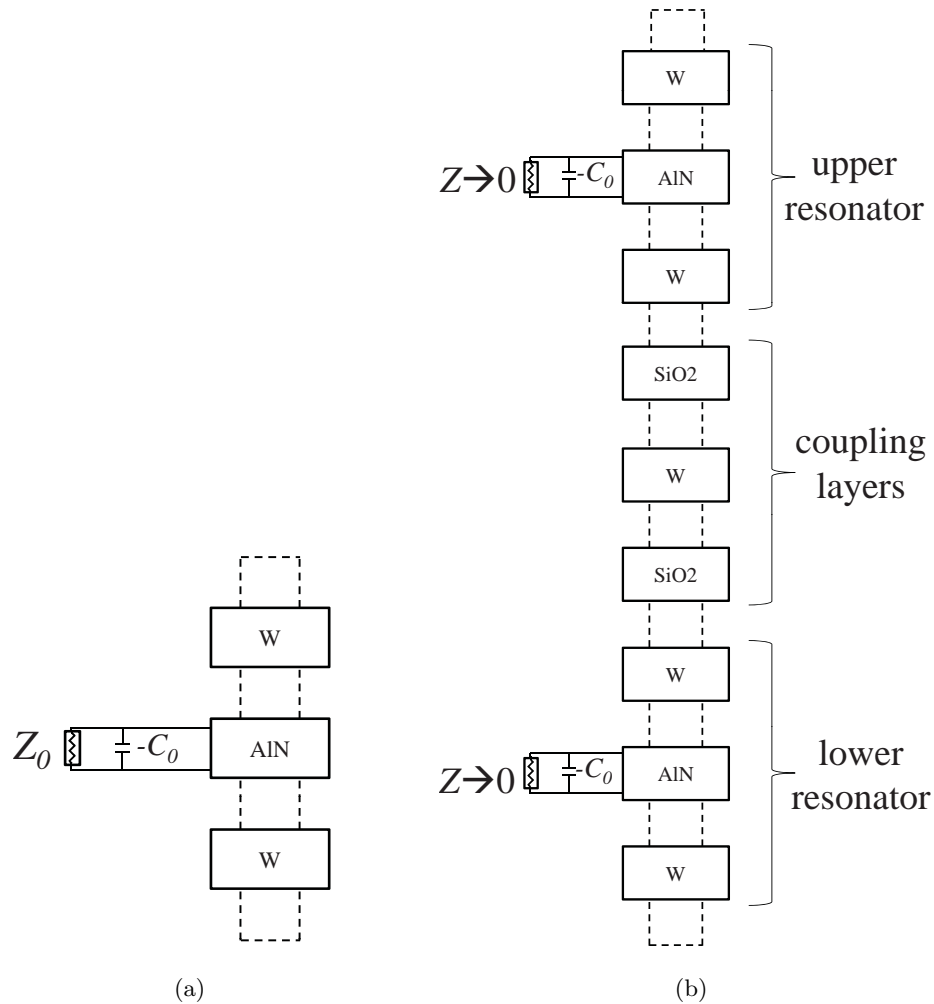


**Figure 4.17:** (a) Mason model configuration to obtain the  $Q_e$  of the resonator when the static capacitor is removed by means of a negative capacitor and (b) configuration to extract the inter-resonator coupling.

Once the coupling matrix is obtained, the design process consists of two steps: 1) Sizing the resonators to fulfill the desired external quality factors and 2) sizing the coupling layers to fulfill the inter-resonator couplings.

**Step 1. External quality factor** In this step, the resonator geometries of each CRF branch are obtained. A simulation configuration such as that shown in Fig. 4.17(a) can be used to obtain the  $Q_e$  of the resonator taking into account that the static capacitors of the resonators must be removed. The simulation to extract the  $Q_e$  is carried out

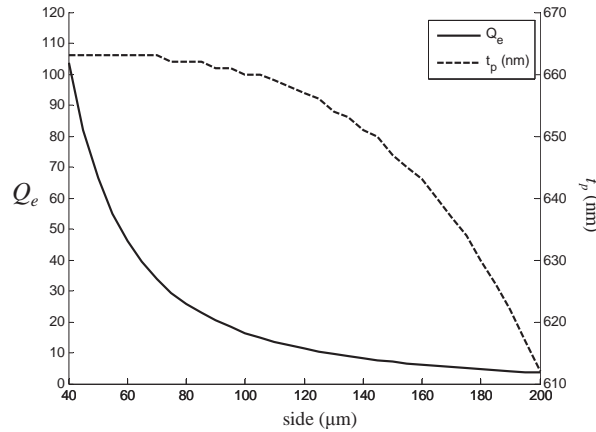


**Figure 4.18:**  $Q_e$  values (continuous line) versus area fulfilling the desired resonance frequency of the resonator composed of a BAW resonator and a shunt cancelling inductor by controlling the piezoelectric thickness  $t_p$  (dashed line)

with a negative capacitor which will be implemented with an inductor.

Fig. 4.18 shows the necessary resonator side and piezoelectric thickness to obtain a given  $Q_e$  at  $f_0$  with electrodes of 200 nm. In this case, the whole resonator is formed by the BAW resonator parallel connected to the inductor that removes its intrinsic shunt capacitor. It can be seen that the  $Q_e$  pattern in this case differs to that obtained for a pure BAW resonator, see Fig. 4.7. When the intrinsic shunt capacitor of the BAW resonator is removed, the  $Q_e$  curve versus side has a downward trend in the whole range of areas of interest in contrast to the case of a pure BAW resonator. This is an interesting effect because lower  $Q_e$  can be implemented which involves higher couplings. Therefore, removing the static capacitors from the resonators can enhance the capabilities of filters such as that presented in the previous section.

From the curve given in Fig. 4.18, the area side of the resonators and the piezoelectric thickness can be obtained to fulfil the external quality factors of each parallel branch 74.65 and 33.56. Therefore, one CRF branch must have an active area of  $47.4 \times 47.4 \mu\text{m}^2$  and the other, an area of  $70.4 \times 70.4 \mu\text{m}^2$ .

**Step 2. Inter-resonator couplings** The extraction of the coupling factor can be carried out directly over the CRF structure as shown in Fig. 4.17(b), in this case a shunt negative capacitor at the input and output of the CRF is necessary. The negative capacitor cancels the static capacitor of the Mason model in the simulation. In this

**Table 4.5:** Layer thicknesses of the CRF in parallel connected configuration

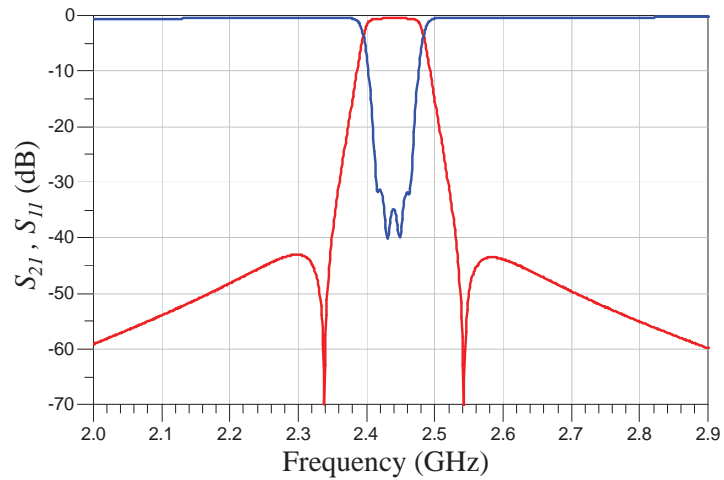
Structure part	Layer	CRF 1	CRF 2
		Thickness (nm)	Thickness (nm)
Upper boundary	Air	-	-
	W	200	200
Upper BAW resonator	AlN	665	665
	W	200	200
Coupling layers	SiO2	709.6	636.5
	W	83.7	203.2
	SiO2	709.6	636.5
Lower BAW resonator	W	200	200
	AlN	665	665
	W	200	200
Lower boundary	Air	-	-

The active area for the CRF 1 is  $47.4 \times 47.4 \mu\text{m}^2$  and for the CRF 2 is  $70.4 \times 70.4 \mu\text{m}^2$ .

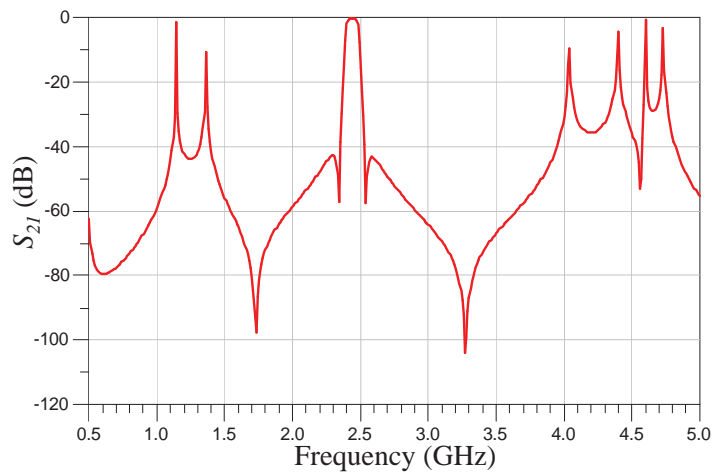
case, the series capacitor that was used in Fig. 4.5(c) to set up the circuit to measure the acoustic coupling between resonators is not needed for simulation and coupling extraction purposes because the cancelling inductors will be part of the final filter device and therefore no shunt capacitors will form impedance inverters.

The value of the impedance inverters that fulfill the coupling values  $k_{14}=0.049$  and  $k_{23}=0.024$  are 0.011 and 0.013 respectively. They are implemented with a set of layers of SiO2/W/SiO2 with thicknesses 709.6/87.3/709.6 nm and 636.5/203.2/636.5 nm for each CRF branch. The values of the coupling layer thicknesses are obtained following the approach presented in section 3.4.

The value of the integrated shunt inductors at the input is  $L_{in}=4.58$  nH and at the output is  $L_{out}=4.01$  nH. The input inductor is calculated taking into account the cancelling inductor of each input resonator  $L_{0i}=1/(w_0^2 C_{0i})$  and merging them as they are placed in the same node. The output capacitor is calculated in the same way and also taking into account the capacitance formed in the coupling layers which here is relevant due to the output cross connection.



(a)



(b)

**Figure 4.19:** (a) Filter response of two parallel connected BAW CRFs and (b) response in a wider span.

### Filter Response

The resulting filter is composed of two CRFs with all the resonators designed to resonate at the same frequency (the central frequency of the filter). They differ in the active area of the CRF and the coupling layers because of the different couplings required for each branch. Table 4.5 summarizes the CRF dimensions for each branch

of the resulting filter. Fig. 4.19(a) shows the filter response of the CRFs connected in parallel presenting the two expected transmission zeros near the passband. Simulations have taken into account inductors with a quality factor of 30 which does not make the final response worse due the fact that they do not take part in the resonances. Resonators with quality factors of 1000 have also been considered. The same losses for the inductors have been taken into account in the next sections. Fig. 4.19(b) shows the response in a wider span of frequencies where the spurious peaks appear far from the passband.

The response fulfills the aim of this section increasing the selectivity of the filter close to passband by means of CRFs and controlling the bandwidth and the return losses of the filter.

### 4.3.2 **Folded Canonical Configuration with CRFs**

#### **Folded Canonical Topology Implemented with CRFs**

The folded canonical configuration of order 4 is an interesting topology for CRF devices because of its ability to insert transmission zeros in the filter response and suitable topology. The nodal representation is shown in Fig. 4.20, it is composed of a mainline branch (continuous line) formed by sequentially coupled resonators and a cross-coupling between resonators 1 and 4 (discontinuous line). This kind of topology was firstly proposed in [82]. In terms of BAW technology CRF manufacturing, it presents two advantages regarding the parallel connected topology: 1) the two CRFs that make up the filter will be identical when the specifications are symmetrical and therefore they can be processed at the same time. It represents an advantage regarding the parallel connected topology, where each parallel branch presents different couplings that involve different coupling layer thicknesses and thus, different manufacturing processes. 2) The input and the output of the device are located in the upper resonators which avoid the necessity of creating vias through a higher number of layers to the lower resonators. However, the main drawback of the folded configuration will be the need for more external elements as will be shown below.

A folded configuration of order 4 implemented with parallel LC resonators is shown in Fig. 4.21(a) where each LC resonator corresponds to a node of Fig. 4.20 and the admittance inverters to an inter-resonator coupling. The inverters that should be drawn

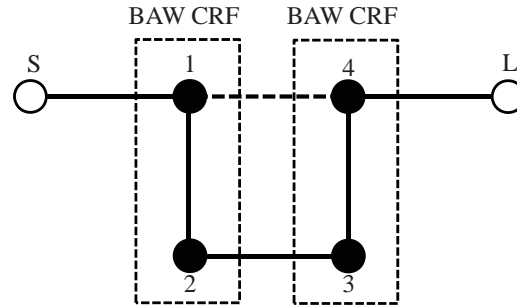


**Figure 4.20:** Nodal representation of a filter network of order 4 in folded canonical configuration

between source/load and the input/output resonators are intrinsically present, that happens because they have the same impedance value as their corresponding port and therefore they are absorbed by it. This concept of inverters absorbed by the ports when they have the same impedance value was proposed in [72].

The equivalent electrical model of a CRF is composed of LC resonators of series type. Therefore, in order to implement the folded configuration with CRFs, it is convenient to reconfigure the folded network composed of parallel LC resonators to series LC resonators. Using the equivalence of Fig. 4.15(b), an equivalent folded configuration network can be obtained with series LC resonators as shown in Fig. 4.21(b). It is composed of a mainline branch with an additional impedance inverter between the input and the output. The mainline branch can be implemented with two cascaded CRFs as shown in Fig. 4.21(c) in the same way as in section 4.2, the difference being that the extreme inverters need an additional external element to be formed. In this case, a transmission line is not intrinsically formed because the extreme resonators are not directly connected to the ports due to the presence of the cross-coupling. The implementation of a real transmission line would occupy considerable space in the final device and has been avoided. Therefore, a series inductor has been added to form the side inverter by means of a T of capacitors where the negative capacitors are implemented with inductors as shown in Fig. 4.21(d).

The inverter that creates the coupling between resonators 1 and 4 has been implemented with a  $\Pi$  of capacitors and an inductor as shown in Fig. 4.22.

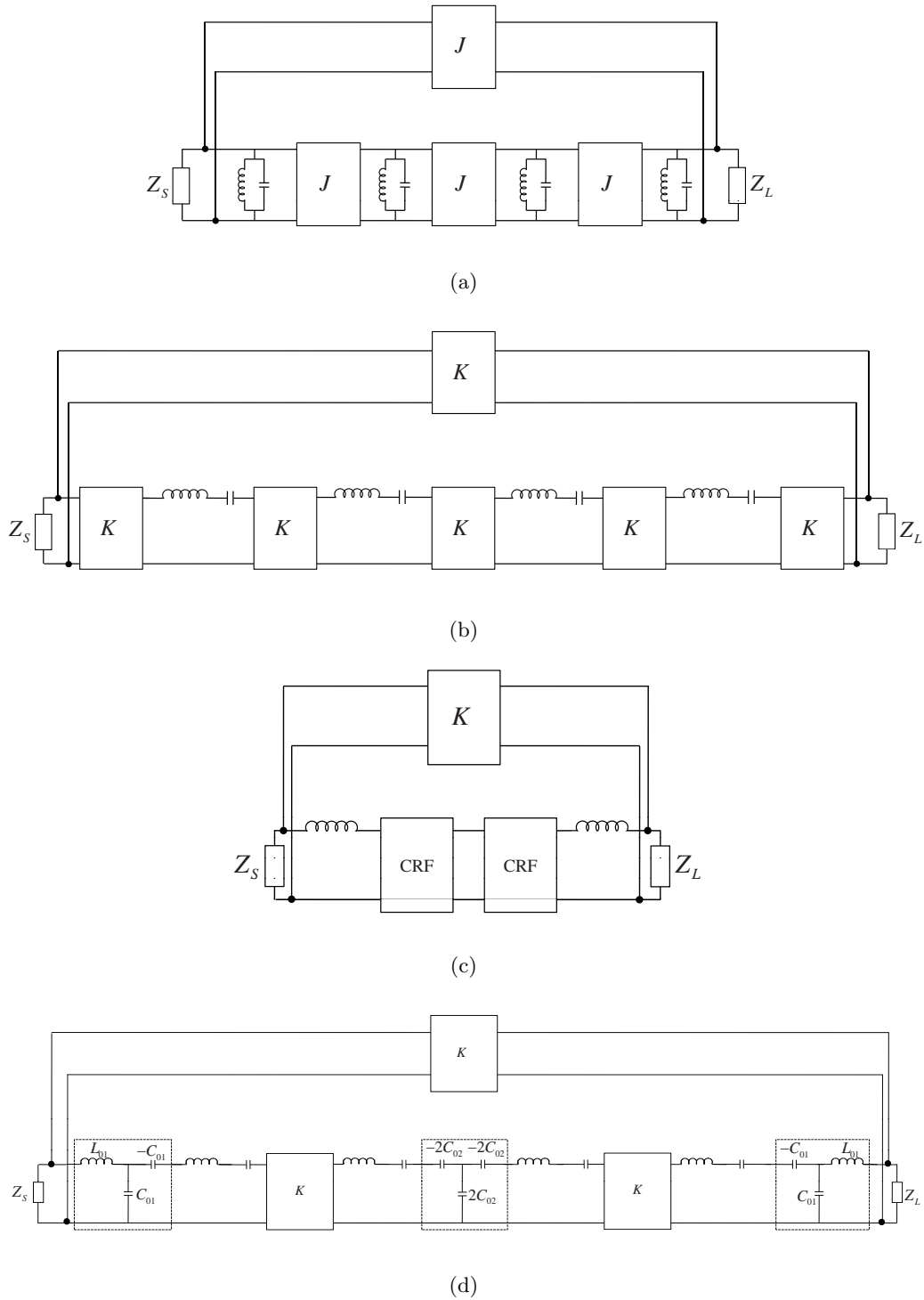


**Figure 4.21:** (a) Folded configuration with parallel LC resonators. (b) Reconfigured network to use series LC resonators. (c) Implementation with CRFs. (d) Equivalent electrical circuit with CRFs.

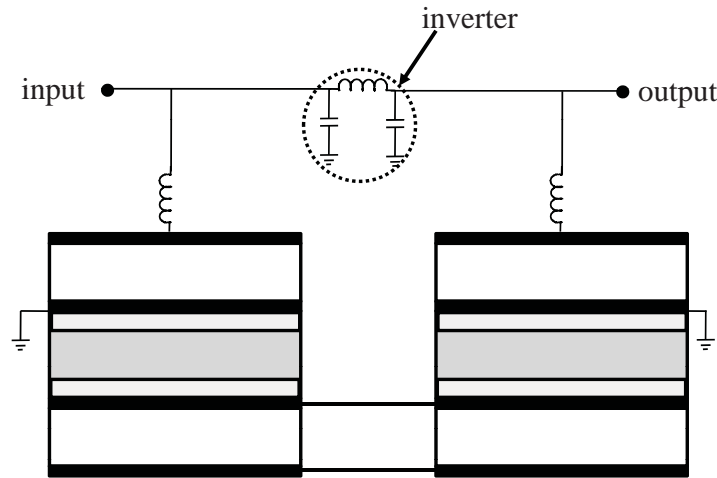


**Figure 4.22:** Cross section of the CRFs in folded configuration and external elements to implement to topology

### Filter Design

To exemplify the kind of responses that this configuration can provide with CRFs, a filter with the same specifications of the previous section has been designed. The coupling matrix is calculated and reconfigured to the folded canonical form following the techniques explained in Appendix B:

$$\mathbf{M} = \begin{bmatrix} 0 & 1.1477 & 0 & 0 & 0 & 0 \\ 1.1477 & 0 & 1.0286 & 0 & -0.0544 & 0 \\ 0 & 1.0286 & 0 & 0.7901 & 0 & 0 \\ 0 & 0 & 0.7901 & 0 & 1.0286 & 0 \\ 0 & -0.0544 & 0 & 1.0286 & 0 & 1.1477 \\ 0 & 0 & 0 & 0 & 1.1477 & 0 \end{bmatrix} \quad (4.20)$$

Note that the cross-coupling must present an opposite sign to that in the mainline couplings in order to create the transmission zeros. The design process is based on the theory of couplings explained above.

The design parameters, external quality factors and inter-resonator couplings, are calculated from the coupling matrix and they are summarized in Table 4.6.

The filter design for the folded configuration will consist of 3 steps quite similar to those followed in section 4.2.

**Table 4.6:** Set of couplings of the folded canonical filter of order 4

$Q_{e1}=Q_{e4}$	74.65
$k_{12}$	0.033
$k_{23}$	0.025
$k_{14}$	-0.002

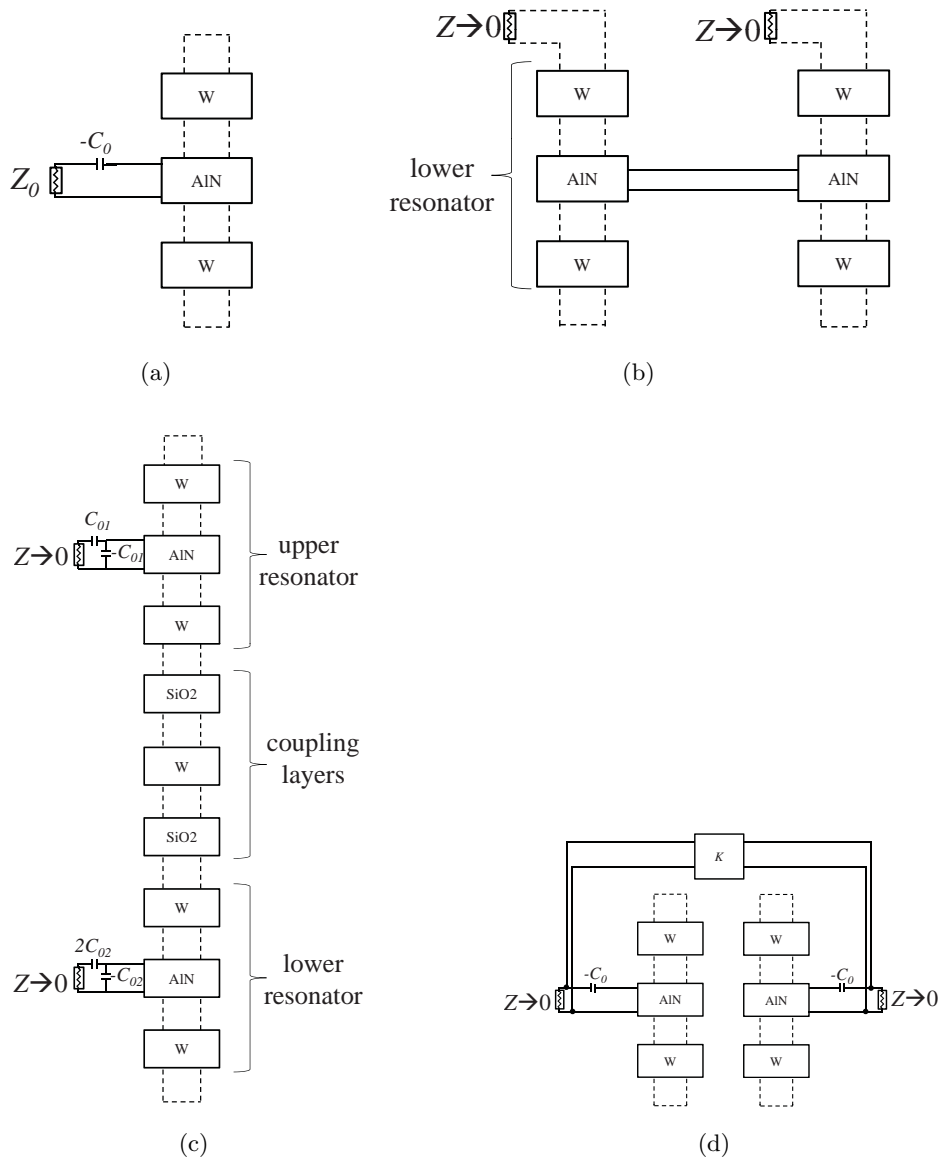


**Figure 4.23:** (a) Mason model configuration to obtain the  $Q_e$  of the input/output resonator with folded configuration, (b) inter-resonator coupling between the lower resonators, (c) vertical acoustical coupling and (d) coupling between the input and the output resonators formed by the electrical impedance inverter

**Step 1. External quality factor** The external quality factor of the input/output resonator will be extracted using the simulation circuit shown in Fig. 4.23(a). A series negative capacitor has been added to the input to form an impedance inverter followed by a series LC resonator as shown in the equivalent circuit in Fig. 4.24. This negative capacitor will be implemented with an inductor in the final structure. The  $S_{11}$  parameter that is used to calculate  $Q_e$ , see (4.16), will be equivalent to that in a shunt LC resonator.

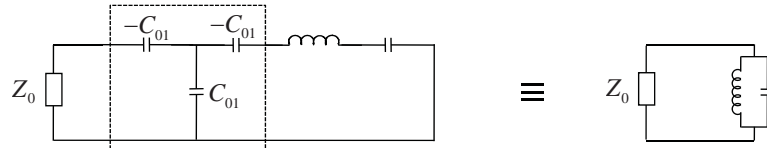


**Figure 4.24:** Equivalent electrical circuit for the extraction of  $Q_e$  in the folded configuration.

Assuming electrodes of  $W$  with a thickness of 200 nm, a piezoelectric thickness of 709 nm and an area side of  $120 \mu\text{m}$  meet the  $Q_e$  requirements and an inductor of 2.44 nH is needed to implement the negative series capacitor in narrow-band.

**Step 2. Electric Coupling between the Lower Resonators** This step is identical to that explained in section 4.2 for the filter of order 4 in mainline configuration. The block formed by the two lower resonators is simulated independently and the transmission response is obtained by decoupling the acoustic ports as shown in Fig. 4.23(b). The coupling value is calculated from the peaks that arise in the transmission response and from (4.13).

Electrodes of  $W$  with a thickness of 250 nm and a piezoelectric thickness of 525.2 nm are found to meet the  $k_{23}$  requirements.

**Step 3. Vertical Acoustic Coupling and Electric Coupling between Upper Resonators** Once the resonators have been sized, the vertical acoustic coupling between the upper and lower resonators can be determined and also the electric coupling between the upper resonators implemented by means of the additional impedance inverter.

Fig. 4.23(c) shows the simulation circuit used to extract  $k_{12}$  and Fig. 4.23(d) the

**Table 4.7:** Layer thicknesses of the CRF in folded configuration

Structure part	Layer/boundary material	Thickness (nm)
Upper boundary	Air	-
	W	200
Upper BAW resonator	AlN	709
	W	200
Coupling layers	SiO2	682
	W	117
	SiO2	682
Lower BAW resonator	W	250
	AlN	525.2
	W	250
Lower boundary	Air	-

The active area of the CRF is  $120 \times 120 \mu\text{m}^2$ .

circuit used to extract the cross-coupling  $k_{14}$  between the upper resonators. A set of SiO2/W/SiO2 coupling layers of thicknesses 682/117/682 nm fulfill  $k_{12}$ . An impedance inverter of value  $700 \Omega$  fulfills  $k_{14}$  and has been implemented by means of the T of capacitors and inductor as shown in Fig. 4.22 with values 45 nH and 93 fF. The low value of the capacitor comes from the high value of the electrical inverter  $K_{14}$  caused by the low necessary coupling between resonators 1 and 4.

### Filter Response

Table 4.7 summarizes the layer thicknesses of the CRF stacks which are identical due to the symmetry of the network and specifications. Fig. 4.25 shows the response of the folded topology implemented with CRFs. It has been plotted jointly with the response of the same structure using ideal negative outer capacitors instead of inductors while the electric inverter has been unchanged, using the T of capacitors and inductor. The comparison of both responses shows that those outer inductors cause the changes regarding the desired response, they introduce additional zeros in the stopband. Moreover, this effect takes place with a worse rejection far from the close stopbands where the transmission tends to be 0 dB.

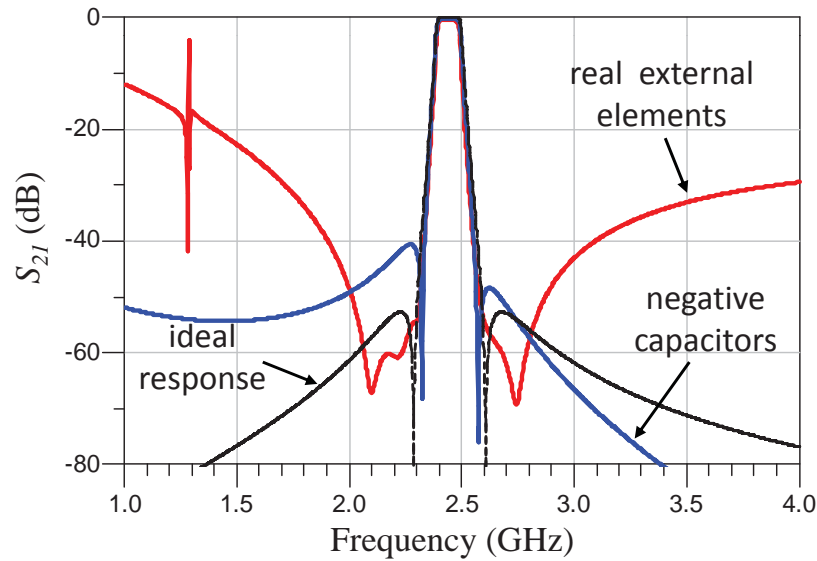


**Figure 4.25:** Ideal filter response for the folded CRF configuration, response implemented with ideal negative capacitors at the input and output resonators and with inductors

#### 4.4 Advanced Responses with SCFs

The SCF is the predecessor of the CRF and it can be interpreted as a CRF without coupling layers (see Fig. 4.26(a)). The lack of a coupling mechanism between the stacked BAW resonators makes them behave as a single resonator as can be seen from its electrical equivalent model in Fig. 4.26(b). Since the appearance of the CRF device, the SCF has been relegated to a second plane basically under the justification that it provides a smaller bandwidth. However, as demonstrated in Chapter 3, a basic CRF implements a bandpass filter of order 2 while a SCF implements a filter of order 1. Therefore, the advantage of a CRF over a SCF is that it can implement filter stages of twice the order of the latter.

Nevertheless, CRFs present a manufacturing drawback regarding SCFs; the extra set of coupling layers makes its manufacturing considerably more difficult than in the SCF case. The number of coupling layers is usually 3 or 5 depending on the desired coupling and only for a single CRF stage. Meanwhile, in the case of a SCF, the total number of layers is not far from a simple BAW resonator making its manufacturing easier.

In this section, a filter topology capable of implementing advanced Chebyshev filter

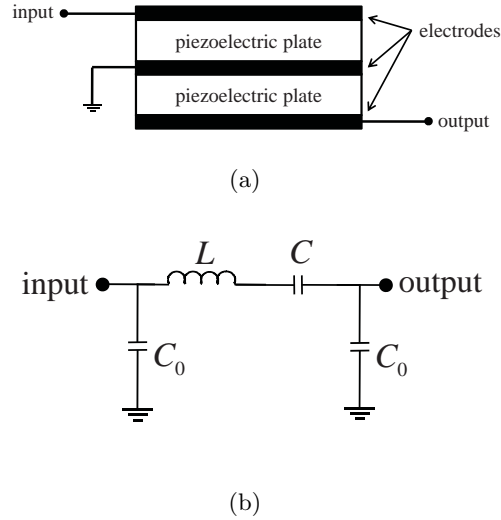


**Figure 4.26:** (a) Stacked Crystal Filter cross section and (b) model.

responses for which SCFs are especially suitable is presented. The topology is known as transversal configuration and the nodal diagram is shown in Fig. 4.27. The general form of the coupling matrix is:

$$\mathbf{M} = \begin{bmatrix} 0 & M_{S1} & M_{S2} & M_{S3} & \cdots & M_{SN} & 0 \\ M_{S1} & M_{11} & 0 & 0 & & 0 & M_{1L} \\ M_{S2} & 0 & M_{22} & 0 & & 0 & M_{2L} \\ M_{S3} & 0 & 0 & M_{33} & & 0 & M_{3L} \\ \vdots & & & & \ddots & & \vdots \\ M_{SN} & 0 & 0 & 0 & & M_{NN} & M_{NL} \\ 0 & M_{1L} & M_{2L} & M_{3L} & \cdots & M_{NL} & 0 \end{bmatrix} \quad (4.21)$$

This configuration is characterized by not having any coupling between resonators. The  $N$  resonators that make up the filter are coupled both to the input and output ports as the first and last row/column of the matrix show. Each resonator is tuned to a particular frequency as the diagonal elements of the matrix show; see (4.12) to find the relationship between the diagonal elements of the coupling matrix and the resonance frequency of any resonator. A SCF fits this configuration perfectly because it presents exactly one resonator coupled to the ports. Fig. 4.28 shows the equivalence of a SCF to a branch of the transversal topology shown in Fig. 4.27 when the static capacitors are removed. Therefore,  $N$  SCFs in parallel connection implement a transversal coupling matrix of order  $N$ . The proposed filter can present an advanced filtering response

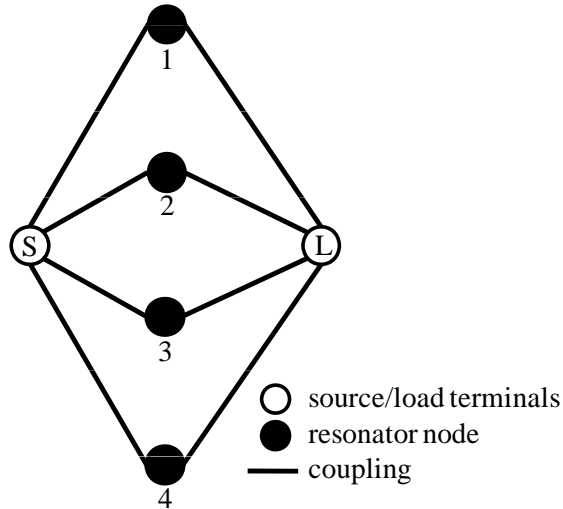


**Figure 4.27:** Nodal diagram of the transversal topology.

together with the easiness of manufacturing SCF devices.

**Filter Design of the Transversal Filter** A W-CDMA filter of order 4 based on SCFs working at  $f_0=2.14$  GHz and bandwidth of 60 MHz will be designed. One transmission zero is allocated above the pass-band and one below to increase the filter selectivity. Table 4.8 gathers the specifications. The coupling matrix for the given requirements is obtained following the procedure presented in Appendix B:

$$\mathbf{M} = \begin{bmatrix} 0 & 0.4569 & -0.6721 & 0.6721 & -0.4569 & 0 \\ 0.4569 & 1.4857 & 0 & 0 & 0 & 0.4569 \\ -0.6721 & 0 & 0.7367 & 0 & 0 & 0.6721 \\ 0.6721 & 0 & 0 & -0.7367 & 0 & 0.6721 \\ -0.4569 & 0 & 0 & 0 & -1.4857 & 0.4569 \\ 0 & 0.4569 & 0.6721 & 0.6721 & 0.4569 & 0 \end{bmatrix} \quad (4.22)$$

Then, the design parameters, external quality factors  $Q_{ei}$  and resonance frequencies  $f_i$  for each resonator numbered by  $i$ , are summarized in Table 4.8 and are obtained from (4.9) and (4.12).

The proposed topology is based on the parallel connection of resonators and each resonator is implemented with a single SCF. No resonator is coupled with another but

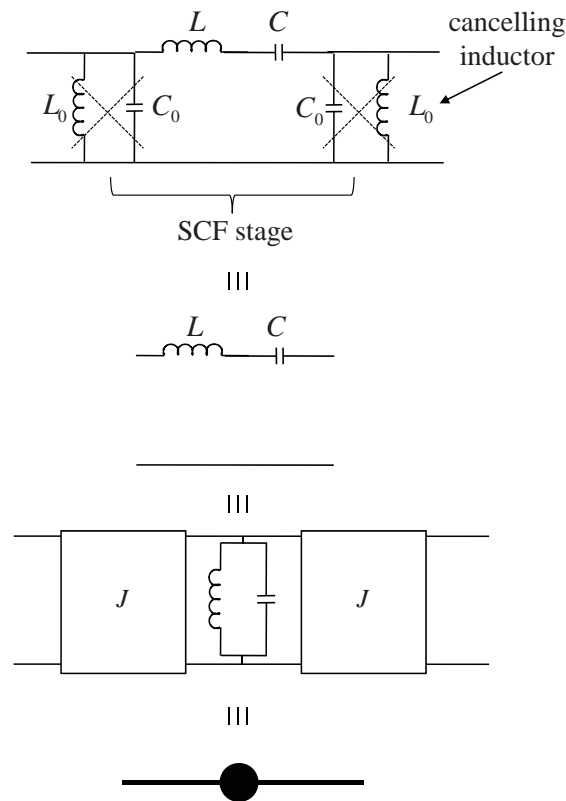


**Figure 4.28:** Stacked Crystal Filter equivalence to a branch of a transversal topology when the static capacitors are cancelled.

**Table 4.8:** Requirements for the example filter based on SCFs in transversal configuration and associated design parameters

Passband frequency range	2.11-2.17 GHz
Relative bandwidth	2.8 %
Center frequency	2.14 GHz
$Z_S = Z_L$	50 $\Omega$
Transmission zeros	$\pm 5$ rad/s
Return loss	>25 dB
$Q_{e1} = Q_{e4}$	170.8
$Q_{e2} = Q_{e3}$	80.0
$f_1$	2.096 GHz
$f_2$	2.118 GHz
$f_3$	2.162 GHz
$f_4$	2.185 GHz

each one is coupled with source and load following the nodal diagram shown in Fig. 4.27. The shunt static capacitor,  $C_{0i}$ , of every SCF  $i$  is removed by means of a shunt inductor with the convenient value to cancel the capacitance effect at  $f_0$ .

The four presented SCFs have different areas and thicknesses of the middle electrode, while the thickness of the remaining layers is identical. The control of the area determines the input and the output  $Q_e$  of the resonators and the control of the middle electrode thickness determines their resonance frequencies. During the design process all the layers of the resonators are taken into account to determine design parameters such as  $Q_e$  and the resonance frequencies. In this case, the  $Q_e$  between a resonator and the input or the output is the same. The proposed SCF symmetric geometry keeps the input and output  $Q_e$  equal as required, that is to say, if the frequency detuning were made by, for example, the upper electrodes, the input and the output  $Q_e$  would be different and the bottom resonator would be modified as well producing a more complex structure to manufacture.

In this topology, as commented above, each resonator presents a different resonance frequency determined by the self-couplings  $M_{ii}$ . Those asynchronous resonators provide a bandwidth enhancement of the overall filter response splitting the transmission poles along the passband. As the resonators are detuned by means of the middle electrode, all the other layers remain identical in terms of thickness for all the resonators, allowing a simple plate to grow during the manufacturing process, due to these layers being processed in parallel.

The parallel resonator topology demands a change of the phase sign between branches 1-3 and 2-4 as seen in (4.22). In this work, a transmission line of impedance  $Z_0$  and electric length of  $180^\circ$  has been added to the output of branches 1 and 3 to create the phase inversion. An additional effect of those lines is the contribution of an out-of-band transmission zero which contributes with higher selectivity close to the passband but worsens the rejection far from it. One drawback of the use of SCFs instead of CRFs is that they cannot implement a change of sign by themselves as in the case of CRFs. Therefore, external elements to produce a  $180^\circ$  phase shift are required such as transmission lines or lumped elements.

Fig. 4.29 shows the schematic of the proposed filter consisting of 4 parallel connected SCFs with the cancelling shunt inductors at their inputs and outputs. The shunt inductors that coincide in the same node have been turned to the equivalent

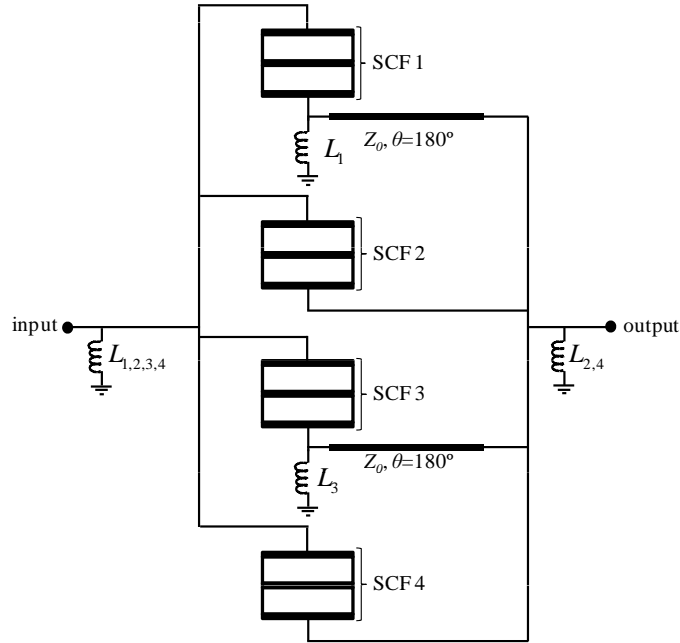


**Figure 4.29:** Transversal configuration with Stacked Crystal Filters.

**Table 4.9:** SCF dimensions

	SCF 1	SCF 2	SCF 3	SCF 4
Top electrode (Mo) thickness (nm)	150	150	150	150
Upper piezoelectric (AlN) thickness (nm)	487	487	487	487
Middle electrode (Mo) thickness (nm)	251	227	170	142
Lower piezoelectric (AlN) thickness (nm)	487	487	487	487
Bottom electrode (Mo) thickness (nm)	150	150	150	150
Side ( $\mu\text{m}$ )	43.6	63.5	61.3	41.0

one. Branches 1 and 3 present the above-mentioned transmission lines.

The SCFs considered are composed of piezoelectric plates of aluminum nitride and electrodes of molybdenum. Fig. 4.30(a) shows the simulation circuit used to extract the  $Q_e$  of each SCF and Fig. 4.30(b) the equivalent electrical circuit.

Table 4.9 summarizes their dimensions to fulfil the requirements in terms of  $Q_e$  and resonance frequencies. The values of the cancelling inductors are  $L_1=16.5$  nH,  $L_3=8.4$  nH,  $L_{2,4}=5.5$  nH and  $L_{1,2,3,4}=2.8$  nH.

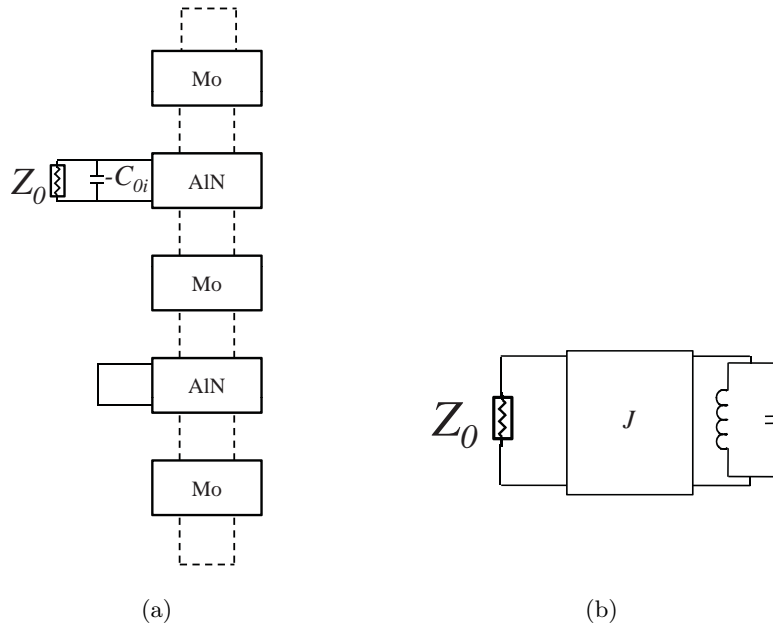


**Figure 4.30:** (a) Simulation circuit based on the Mason model to extract the  $Q_{ei}$  and to center at  $f_i$  each resonator  $i$  and (b) the equivalent electrical circuit.

**Transversal SCFs Filter Response** Fig. 4.31 shows the individual response in terms of transmission of every SCF, which are tuned to their corresponding resonance frequency. Each SCF presents a bandwidth that depends on the  $Q_e$  and resonance frequency to which they were designed.

Finally, Fig. 4.32 shows the filtering response of the proposed structure with the 2 expected transmission zeros: 1 above the passband and 1 below. The above discussed transmission zero originated from the inverting transmission line of  $180^\circ$  is also present in the lower stop-band.

## 4.5 Summary

A CRF is a microwave filter that operates both on the electrical and the mechanical plane and its behavior can be fully modeled electrically by means of a filter topology composed of impedance inverters and series LC resonators. It can therefore implement Chebyshev filter responses with an order equal to the number of BAW resonators present in the structure. The use of electrical representation with filter topology allows the coupling and resonance mechanisms that take place in the device to be identified.

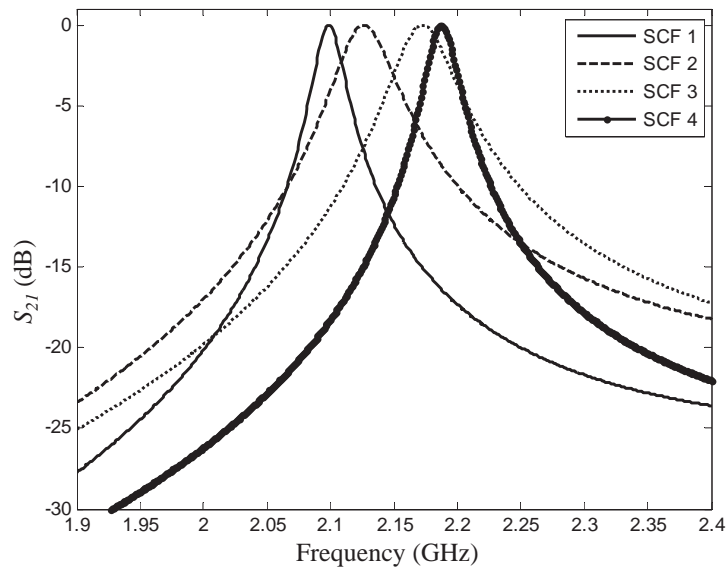


**Figure 4.31:** Individual  $S_{21}$  response of every Stacked Crystal Filter.

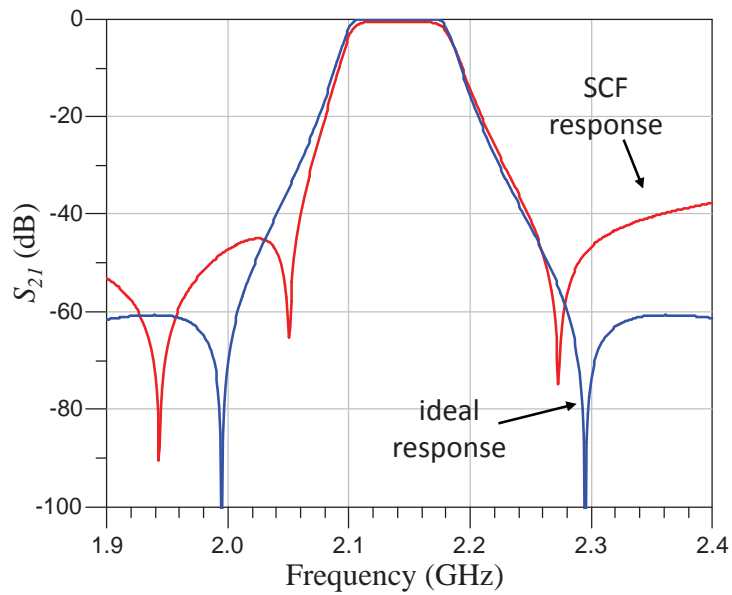


**Figure 4.32:** Response of the transversal SCFs configuration.

General coupling theory has been used to determine the bounds of this device in terms of bandwidths and return losses, which are related to the couplings that this structure can withstand. A filter of order 4 composed of two cascaded CRF basic stages was initially considered, which gathers 3 kinds of couplings: port to resonator coupling, inter-resonator acoustic coupling and inter-resonator coupling formed by a direct connection between resonators. The maximum coupling levels that can be achieved between the ports and the resonators depend on the maximum piezoelectric coupling constant that the resonator can provide and a suitable selection of its active area. Those coupling levels are related to the bandwidth and RL and thus the bounds coming from this coupling are established. In the case of the coupling formed by the electrical connection between lower resonators, maximum coupling levels depend on the piezoelectric coupling constant and not on the active area. This means that the highest coupling between resonators is achieved when the BAW resonators present the highest piezoelectric coupling constant. Nevertheless, to implement an arbitrary Chebyshev response it is not appropriate to have the highest possible couplings in all the coupling parts of the network, but rather, to fulfill the coupling values obtained from the coupling theory filter synthesis procedure. In other words, piezoelectric coupling does not necessarily have to be maximized for all the BAW resonators that comprise the CRF device. This has been demonstrated in this chapter, where the lower BAW resonators of the example filter are designed with a proper SMR stack to reduce the piezoelectric coupling constant in order to fulfill the filter synthesis equations in terms of inter-resonator coupling. The acoustic coupling between resonators covers a wide range of coupling values thanks to the approach that combines high and low acoustic impedance passive layers.

The general coupling theory has been used to obtain filters based on CRFs with advanced filtering responses providing transmission zeros and the consequent selectivity improvement. Several topologies have been reviewed and the two selected and presented in this chapter are the parallel connected CRFs and the folded configuration. The first, presents the advantage of obtaining responses quite close to those desired, but the drawback of the need for CRFs with different geometries in terms of thicknesses in such a way that they cannot be processed in parallel during manufacturing. The folded configuration provides a good selectivity close to the passband as expected from the ideal desired response but at far-off frequencies the attenuation worsens due to the effect of the required external inductors. Nevertheless, the advantage of the folded configuration is that, when it implements filters of order 4 with transmission zeros and

symmetrical responses, the two CRF stacks have the same geometries and they can be manufactured in parallel.

Finally, a RF BAW filter based on SCFs and on a novel topology applied to this technology was presented. The use of parallel connected SCFs to implement a transversal coupling matrix enables the creation of advanced responses with this kind of device easier to manufacture than CRFs.

## Chapter 5

# CRF Functionalities beyond the Bandpass Filter

Bulk acoustic wave coupled resonator filters can provide further functionalities than bandpass filtering. This chapter gathers two of these which expand the potential of this device.

The first one as a bandstop filter is proposed for the first time in this work. Although bandstop filters using BAW technology have been already implemented with ladder filters [83], they have not been studied with CRFs so far. The use of CRFs to implement this function enables a new range of possibilities characteristic of the coupling theory filter synthesis such as control of the bandwidth and rejection levels of the stopband by means of the couplings that take place in the structure.

The second functionality is well known in the BAW technology field; it is the single-ended to differential (SE2DE) mode conversion. This chapter will show how to design SE2DE filters using the theory of couplings developed in the previous chapter.

### 5.1 Bandstop BAW Coupled Resonator Filters

Bandstop filters are widely used in RF devices of several technologies to prevent interferences with other applications and users. Although typical BAW technology filters present bandpass functions, special attention has been paid to bandstop filters in the last years to differentiate between frequency ranges that are inherently spurious free and those with spurious content [83]. Bandstop filters can meet the increasingly drastic

required specifications in terms of rejection.

This section presents a novel topology composed of CRFs providing a controllable bandstop response. Although CRFs present a natural bandpass behavior, a convenient arrangement of those devices can provide a bandstop response. The topology is based on creating a direct path between the input and the output ports that provides full transmission of the signal, and adding CRFs parallel to the direct path in such a way that they absorb energy at the specified stopband. The energy absorption takes place at the desired rejection band where a spurious or undesired signal must be eliminated while the immediate range of frequencies above and below the stopband provides transmission.

### 5.1.1 Direct-Coupled Bandstop Filters

A bandstop characteristic is straightforward to generate from regular low-pass prototype polynomials exchanging the reflection and transfer functions [84]. Then, the coupling matrix can be synthesized following a similar process to the synthesis of bandpass responses described in Appendix B. The difference in the synthesis of the coupling matrix is that it needs to incorporate a direct source-load coupling [85].

This kind of bandstop filter synthesis takes advantage of the flexibility on the Chebyshev response of the bandpass filter synthesis procedure. An equi-ripple in the passband is translated to a controlled equi-ripple inside the frequency range of the stopband. The stopband can be easily controlled by means of the control of the couplings.

Once the bandstop coupling matrix is synthesized it can also be reconfigured to obtain the most appropriate topology. Below, a bandstop filter composed of a parallel connected CRF with direct source-load coupling is presented. Fig. 5.1 shows the nodal representation of a parallel connected filter of order 4 where a direct coupling between source and load takes place.

### 5.1.2 Example of a Bandstop Filter with Parallel Connected CRFs

A filter with the specifications given in Table. 5.1 will be designed to exemplify a bandstop filter composed of CRFs. The coupling matrix presents a non-zero value at the source-load coupling element and the other elements present the parallel connected

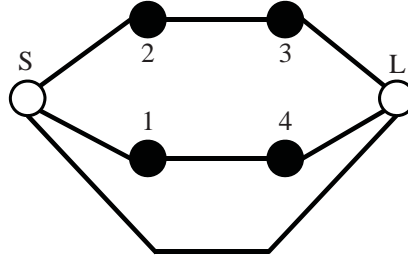


**Figure 5.1:** Nodal representation of a bandstop filter of order 4 in parallel connected configuration

**Table 5.1:** Requirements for the bandstop filter with parallel connected configuration and associated couplings

Bandstop frequency range	2.40-2.48 GHz
Relative bandwidth	3.28 %
Center frequency	2.44 GHz
$Z_S=Z_L$	50 $\Omega$
Stopband rejection	>22 dB
$Q_{e1}=Q_{e4}$	15.2
$Q_{e2}=Q_{e3}$	87.6
$k_{14}$	0.052
$k_{23}$	0.037
$M_{SL}$	1

topology:

$$\mathbf{M} = \begin{bmatrix} 0 & 1.4122 & 0.5898 & 0 & 0 & 1.0000 \\ 1.4122 & 0 & 0 & 0 & 1.5720 & 0 \\ 0.5898 & 0 & 0 & 1.1277 & 0 & 0 \\ 0 & 0 & 1.1277 & 0 & 0 & -0.5898 \\ 0 & 1.5720 & 0 & 0 & 0 & 1.4122 \\ 1.0000 & 0 & 0 & -0.5898 & 1.4122 & 0 \end{bmatrix} \quad (5.1)$$

Note that the bandstop coupling matrix presents a unit value in the position corresponding to the source-load coupling.

Fig. 5.2 shows the configuration of the bandstop filter implemented with CRFs. It presents the same topology as the parallel connected one for bandpass filters with the addition of the impedance inverter formed with lumped elements. The direct coupling  $M_{S1}$  involves an impedance inverter of value  $K=M_{S1}Z_0$ . The value of the direct coupling is  $M_{S1}=1$  and therefore, it could alternatively be implemented by means of a quarter-wave transmission line with impedance  $Z_0$ .

After applying exactly the same design process as for bandpass filters, the band-

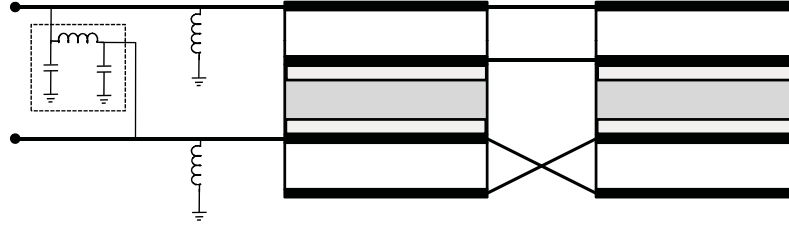


**Figure 5.2:** CRF configuration of the bandstop filter including external elements

**Table 5.2:** Layer thicknesses of the bandstop CRF

Structure part	Layer	CRF 1	CRF 2
		Thickness (nm)	Thickness (nm)
Upper boundary	Air	-	-
	W	200	200
Upper BAW resonator	AlN	666.1	665.6
	W	200	200
	SiO <sub>2</sub>	728	685
Coupling layers	W	72.5	118.1
	SiO <sub>2</sub>	728	685
	W	200	200
Lower BAW resonator	AlN	666.1	665.6
	W	200	200
	Air	-	-

The active areas of the CRF 1 and 2 are  $104.4 \times 104.4 \mu\text{m}^2$  and  $43.7 \times 43.7 \mu\text{m}^2$  respectively.

stop CRF dimensions are given in Table 5.2. The input and output cancelling inductors have values  $L_{input}=2.57 \text{ nH}$  and  $L_{output}=2.50 \text{ nH}$  respectively. The values of the lumped elements that implement the inverter are  $C_{inv}=1.3 \text{ pF}$  and  $L_{inv}=3.26 \text{ nH}$  for the capacitors and inductor respectively.

Fig. 5.3 shows the bandstop response of the proposed filter. Although the response was designed theoretically without any reflection zero, the designed filter with external lumped elements has two reflection zeros above the stopband and two below it. These occur because of the effect of the inductors which behave as negative capacitors in narrowband around  $f_0$ , but far from the stopband their inductive behavior in the device causes the poles in the passbands. The obtained response presents a rejection better than 22 dB inside the stopband, and the RL are better than 10 dB in the lower

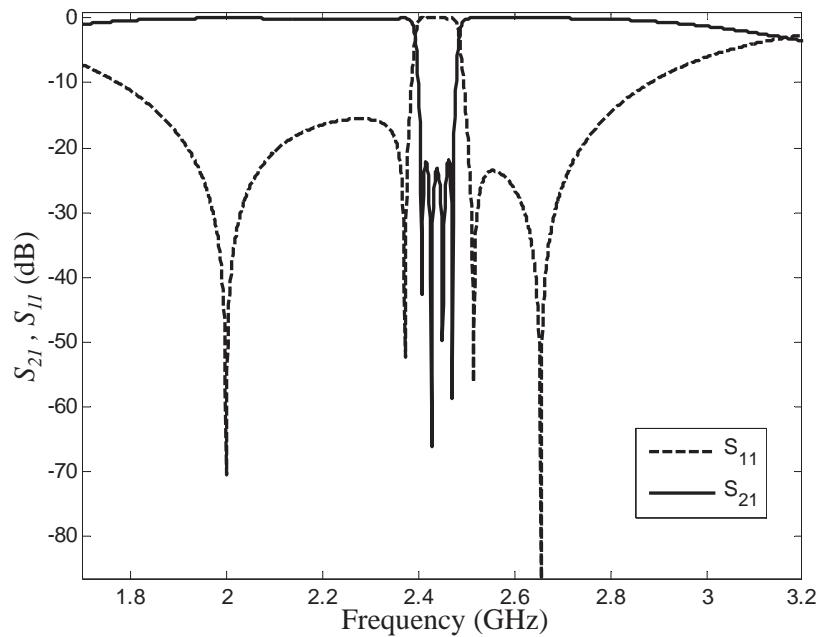


**Figure 5.3:** Response of the stopband filter implemented with CRFs

passband from 1775 MHz to 2384 MHz and in the upper passband from 2494 MHz to 2883 MHz.

## 5.2 Single to Balanced Mode Operation with Coupled Resonator Filters

Coupled resonator filters are very suitable devices to bring BAW technology to duplexers. A duplexer may be found close to the antenna in some handheld communication systems. Duplexers create a simultaneous access to the antenna from both the receiver and the transmitter parts of the system. Some applications, such as for example, W-CDMA, present stringent specifications to separate the receiver and transmitter signals which have bands that can be quite close [54].

In the transmitter path, a power amplifier is found before the RF transmitter filter and in the receiver path, a LNA follows the RF receiver filter as shown in Fig. 5.4. The antenna and the power amplifier typically have  $50 \Omega$  impedance and present single-ended ports. However LNAs inputs often present higher impedances, for example  $100 \Omega$  or  $200 \Omega$ , and they have balanced ports. Therefore, there must be a single to balanced

conversion between the antenna and the LNA, and an impedance transformation.

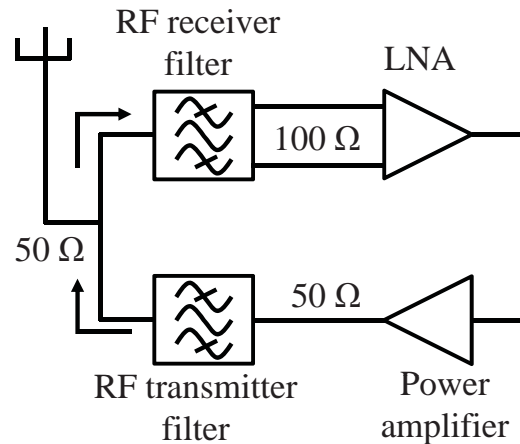


**Figure 5.4:** Duplexer block diagram

Ladder filters provide very high quality filters, but they are not capable of providing SE2DE input/output ports, or impedance transformation. A bulk acoustic wave coupled resonator filter can provide mode conversion between a single-ended port and a balanced one thanks to the galvanic isolation between the input and the output. Therefore, a CRF is a key device in BAW technology for single-to-balanced RF filters [52]. Moreover, it can provide impedance transformation matching the input and output resonators to the desired ports. These features render a CRF a device that can perform the same functions as a filter and a balun all at once.

### 5.2.1 SE2DE CRF Filter with Impedance Transformation Ratio 1:4

In [53], Fattinger et al proposed the first SE2DE based on CRFs. The filter configuration provided an impedance transformation ratio of 50:200 useful for LNAs with input impedance of 200  $\Omega$ . The principle of operation of the SE2DE can be explained from the configuration shown in Fig. 5.5. Two identical branches are considered; each branch is composed of two identical CRFs in series connection. The single-ended input signal is applied to the upper electrode of the input resonator of each CRF branch and their lower electrodes are grounded. Note that a 180° phase shift is produced between the signals of the two branches due to the connection of the lower resonators. One branch presents an inverted electrical electrode connection regarding the other one. When the signal arrives to the output resonators of each branch, it presents the same amplitude

$V_{out}$  but opposite sign. Therefore, the balanced output is produced between the upper electrodes of the output resonators of each branch with a voltage difference of  $2V_{out}$ . Some variants on this configuration can produce the same results, for example inverting the outputs or the inputs instead of the electrical connection of the lower resonators.

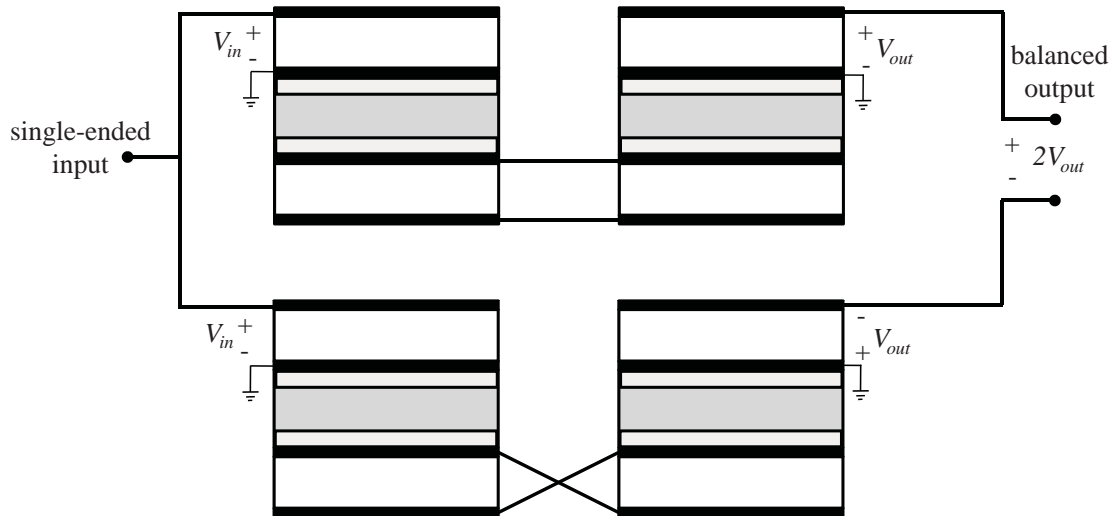


**Figure 5.5:** CRF configuration to provide a single-ended to balanced conversion

Another important feature to take into account in this configuration is the impedance transformation between the input and the output ports. It is assumed that each branch is composed of a CRF filter of order 4 matched to input and output ports of impedance  $Z_0$ . In this way the CRF layer stacks are identical and can be manufactured in parallel. When the two branches are connected as in Fig. 5.5, the input and output impedances of the resulting device are not  $Z_0$ . The input port sees the two branch inputs in parallel, so that, the input impedance is  $Z_0/2$ . Meanwhile, the output port sees the two branch outputs in series and the corresponding impedance is  $2Z_0$ . Therefore, if the filters of order 4 that make up each branch are designed at  $Z_0=100\ \Omega$ , the input impedance of the resulting device is  $50\ \Omega$  and the output impedance  $200\ \Omega$ . This configuration provides an impedance transformation ratio of 1:4.

As a design example, a filter with the requirements presented in Table 5.3 and the topology shown in Fig. 5.5 will be synthesized. The specifications are the same as the single-ended output filter of section 4.2, the difference being the source and load impedances and the requirement of mode conversion. The set of couplings and external

**Table 5.3:** Requirements for the mode-conversion filter and associated couplings

Passband frequency range	2.40-2.48 GHz
Relative bandwidth	3.28 %
Center frequency	2.44 GHz
$Z_S$	50 $\Omega$
$Z_L$	200 $\Omega$
Return loss	15 dB
$Q_{e1}=Q_{e4}$	36.5
$k_{12}=k_{34}$	0.026
$k_{23}$	0.021

quality factors are the same. In order to design this mode-conversion and impedance transformer filter, each branch composed of a CRF of order 4 is synthesized following exactly the same design procedure as in section 4.2. The only difference to consider here is that this branch is designed taking into account input and output ports of 100  $\Omega$  to obtain a final device with a conversion from 50  $\Omega$  to 200  $\Omega$ .

Table 5.4 shows the layer thicknesses of a CRF stack. The four CRF stacks have the same layer configuration and geometry. The input and output resonators have been sized to provide the desired  $Q_e$  when they are connected to 100  $\Omega$  ports.

Fig. 5.6 shows the phase of each branch of the mode-conversion device. A phase difference of 180° can be shown throughout the frequency range. This phase difference is the key to provide the mode conversion. The phase has been calculated straightforwardly simulating each branch independently, that is to say a conventional filter of order 4, using ports of 100  $\Omega$  and taking into account the polarity of the ports shown in Fig. 5.5.

The response of the mode-conversion filter is shown in Fig. 5.7. Although a total of 8 resonators make up the filter structure, the response corresponds to a filter of order 4. The duplication of the structure enables the mode-conversion and impedance transformation but does not increase the order of the resulting filter, nor does it improve the response characteristic.

**Table 5.4:** Layer thicknesses of one CRF stack of the mode-conversion filter

Structure part	Layer/boundary material	Thickness (nm)
Upper boundary	Air	-
Upper BAW resonator	W	200
	AlN	693
	W	200
Coupling layers	SiO <sub>2</sub>	661
	W	149
	SiO <sub>2</sub>	661
Lower BAW resonator	W	243
	AlN	479
	W	243
Bragg reflector	SiO <sub>2</sub>	900
	W	440
	SiO <sub>2</sub>	900
	W	440
	SiO <sub>2</sub>	500
Lower boundary	Si	-

The active area of the CRF is  $86 \times 86 \mu\text{m}^2$ .

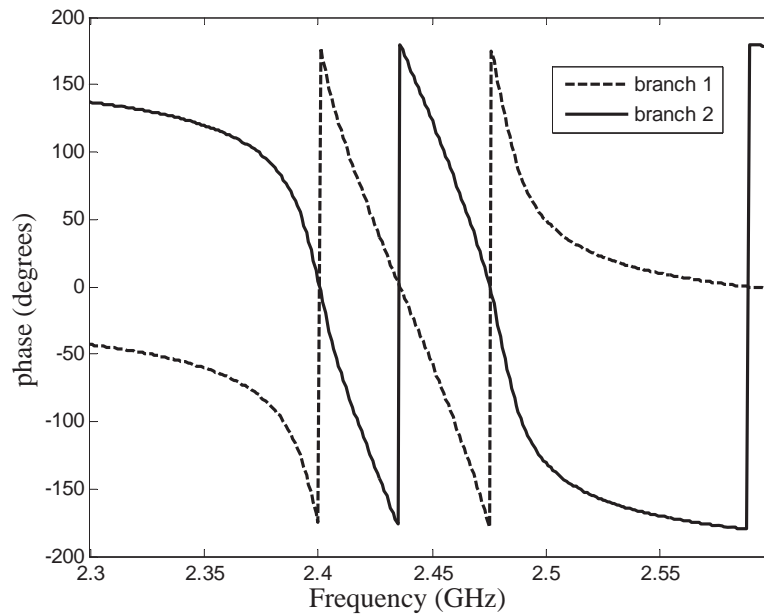


**Figure 5.6:** Phase of each branch of the mode-conversion filter with impedance transformation ratio 1:4

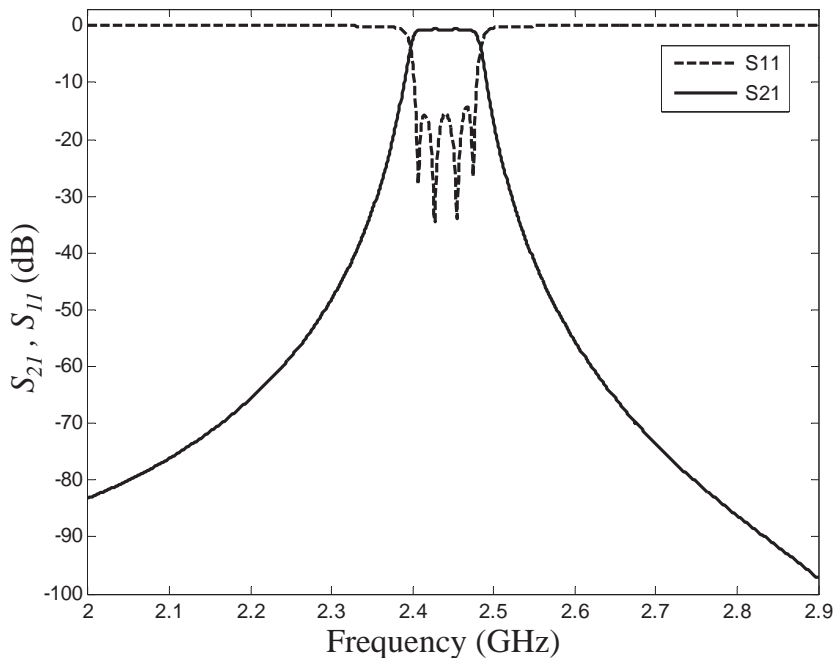


**Figure 5.7:** Response of the mode-conversion filter with impedance transformation ratio 1:4

### 5.2.2 SE2DE CRF Filter with Arbitrary Impedance Transformation Ratio 1:t

In the previous subsection, a SE2DE CRF filter with an impedance transformation of ratio 1:4 was presented. This configuration works well for LNAs with input impedance of  $200 \Omega$ . However, LNAs with other input impedances may be present in a communication system and a more flexible transformation ratio may be required. A SE2DE CRF filter with arbitrary impedance transformation ratio 1:t is presented in [86] and [87].

The principle of operation of this device is basically the same as the SE2DE filter presented in [53] and can be explained by Fig. 5.8. Two basic CRF stacks are considered. The single-ended signal is applied to the input resonator of each CRF branch but with opposite polarization by means of reversing the electrode connection. The voltage that is produced at the output resonators of each branch has the same absolute value and opposite sign. The control of the transformation ratio comes from the possibility of matching the upper resonators to a different impedance than the lower resonators. In the previous subsection, the input and output resonators were both upper resonators and they were forced to have the same layer thickness in order to be processed in

parallel during the manufacturing.

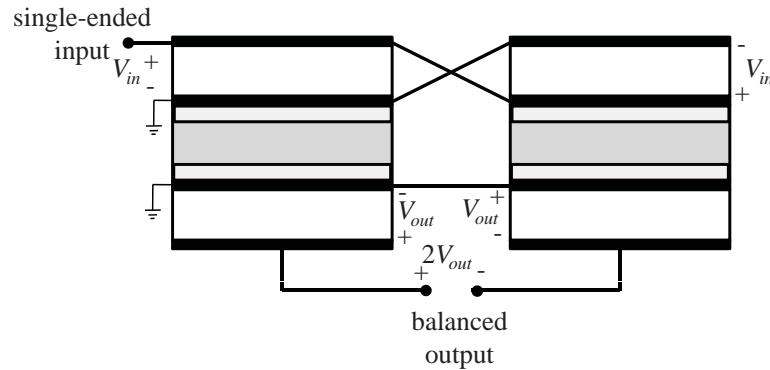


**Figure 5.8:** CRF configuration to provide a single-ended to balanced conversion and arbitrary 1:t impedance transformation

In this new configuration, the filter design process presented in chapter 4 can also be applied. Assuming a general impedance transformation from  $Z_{01}$  to  $Z_{02}$ , each CRF branch must be designed with an input impedance of  $2Z_{01}$  and an output impedance of  $Z_{02}/2$ . In this way, when the branches are connected as in Fig. 5.8, the input impedance of the whole device sees the input impedances of the branches in parallel resulting in  $Z_{01}$  and the output impedance of the device sees the output impedances of each branch in series connection resulting in  $Z_{02}$ .

As a design example a SE2DE filter for W-CDMA with the specifications given in Table 5.5 and impedance transformation  $50 \Omega$  to  $100 \Omega$  will be designed. The input resonators are designed to provide a  $Q_e=33.17$  when they are coupled to an input port of  $100 \Omega$  ( $2Z_{01}$ ) and the output ports to provide the same  $Q_e$  but coupled to an output port of  $50 \Omega$  ( $Z_{02}/2$ ).

**Table 5.5:** Requirements for the mode-conversion filter with impedance transformation ratio 1:2 and associated couplings

Passband frequency range	2.11-2.17 GHz
Relative bandwidth	2.8 %
Center frequency	2.14 GHz
$Z_S$	$50 \Omega$
$Z_L$	$100 \Omega$
RL	15 dB
$Q_{e1}=Q_{e2}$	33.17
$k_{12}$	0.036

A summary of the geometries of the CRFs is shown in Table 5.6. Note that the input and output resonators share the same active area; therefore, they are matched to the corresponding impedance with the help of the electrode and piezoelectric thicknesses that allow the resonator to be centered at  $f_0$  and the necessary  $Q_e$  to be fulfilled.

**Table 5.6:** Layer thicknesses of one CRF stack of the mode-conversion filter with impedance transformation ratio 1:2

Structure part	Layer/boundary material	Thickness (nm)
Upper boundary	Air	-
	W	170
Upper BAW resonator	AlN	1046
	W	170
	SiO <sub>2</sub>	759
Coupling layers	W	161
	SiO <sub>2</sub>	759
	W	200
Lower BAW resonator	AlN	890
	W	200
Lower boundary	Air	-

The active area of the CRF is  $110 \times 110 \mu\text{m}^2$ .

Fig. 5.9 shows the phase of each branch that makes up the SE2DE filter. The phase is obtained considering a CRF stack and measuring the phase of the transmission response taking into account an input port of  $100 \Omega$  and an output port of  $50 \Omega$ . Fig. 5.10 shows the response of the device which corresponds to a filter of order 2. The drawback of this configuration is the low order of the resulting filter. To improve the selectivity of the response, it can be combined with other CRFs as in [87].

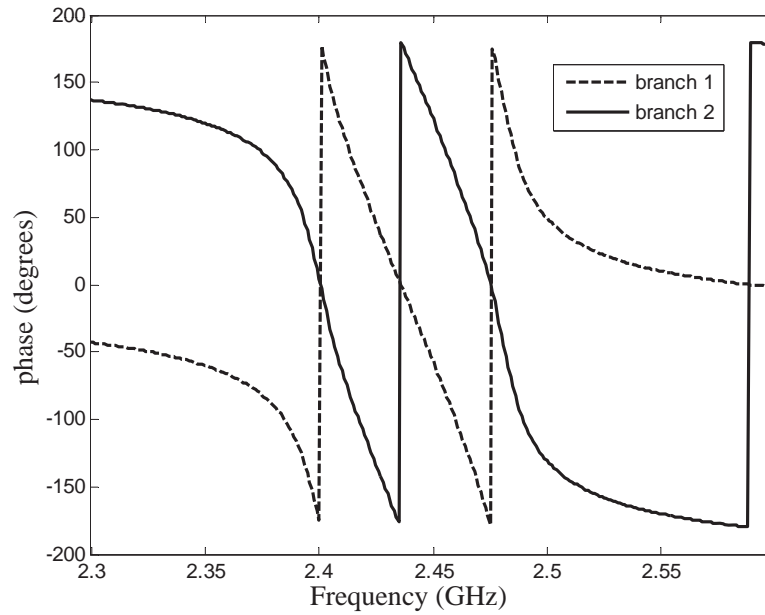


**Figure 5.9:** Phase of each branch of the mode-conversion filter with impedance transformation ratio 1:2

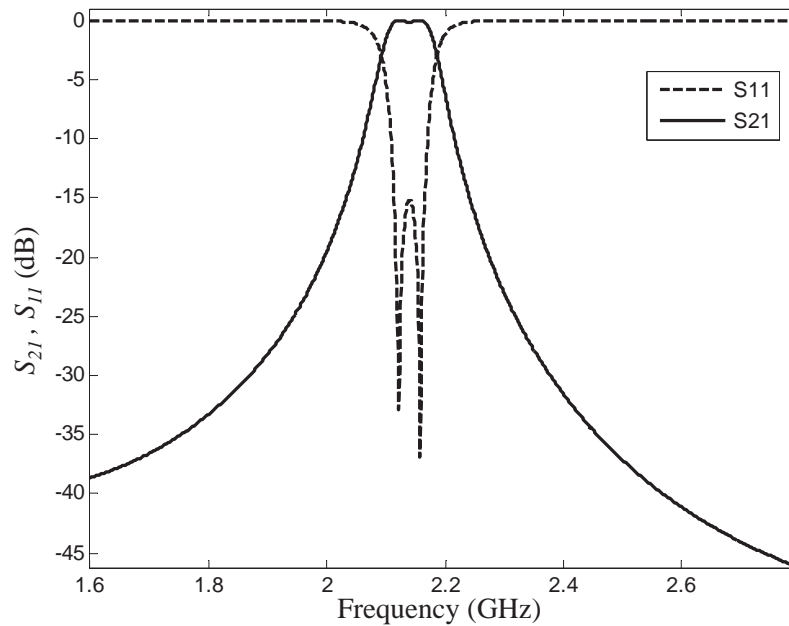


**Figure 5.10:** Response of the mode-conversion filter with impedance transformation ratio 1:2

## 5.3 Summary

In this chapter, two functionalities of CRFs have been presented beyond the bandpass one: bandstop filters and single-ended to balanced mode conversion.

A novel approach to implement bandstop filters with CRFs has been presented based on the bandstop coupling matrix. A set of parallel connected CRFs and a direct coupling between source and load have been used to form the bandstop response. The BAW bandstop filter may be of special interest when a specific narrow band of frequencies needs to be attenuated. Although the same operation could be done by a bandpass filter, it may be difficult to obtain a good rejection performance over the stopband and at the same time maintain a low insertion loss and good return loss performance over the main signal band.

This section also demonstrated how the coupling theory can also be used to design filters with mode-conversion from single-ended to differential mode. This functionality of CRFs enables the use of BAW technology for mode-conversion, a performance which was formerly carried out by SAW technology or BAW filters combined with baluns.

## Chapter 6

# Conclusions and Future Work

### 6.1 Conclusions

BAW technology can be considered quite a recent technology, the advances in wafer processing in microelectronics in the last decade have enabled a successful manufacturing of miniaturized and high-performance thin film BAW filters. BAW technology is still maturing and providing new solutions for several RF filter requirements and applications. It is an exciting technology to work with because there are many topics that still require a lot of research: manufacturing processes, characterization of acoustic materials, device modeling, device design, new materials, new devices and structures, 2D and 3D simulations of the devices, etc. Chapter 2 provided a description of the BAW technology, its foundations, figures of merit, materials and types of devices.

The ladder type filter is currently the most used BAW filter type. Therefore, most of the efforts in improving BAW technology have been driven by the requirements that ladder filters can meet. The CRF has recently emerged as a very promising BAW filter type. It presents very attractive features such as better rejection far from the passband regarding ladder filter responses, wider bandwidths and mode-conversion from single-ended input to balanced output. CRFs have encountered a BAW technology where a lot of work has been carried out in manufacturing, characterization, improvement of materials or the resonators. However, CRFs are still difficult to design and manufacture, since more layers are used to form more than one resonator and they are coupled in the vertical direction. CRF modeling and design techniques have not been explored in depth and have been mainly entrusted to optimization techniques in a similar way

to those usually carried out for ladder filters. One of the challenges in CRFs is how to make their design friendlier and more efficient in terms of taking the most of their capabilities.

Chapter 3 of this Ph.D. dissertation researched the modeling of CRFs and variants of the basic device. The proposed equivalent electrical models provide a compact and clear way of explaining the filtering behavior of the structure. The models offer an explanation of the filter mechanisms that take place inside the structure: resonances and couplings. Moreover, they create a link between the coupling theory of filter synthesis and the BAW device. The coupling layers mechanism, a key element of a CRF, has been investigated, their effects have been studied and their design considerations have been presented.

The coupling theory is a widely extended and powerful technique to design microwave filters especially suitable for CRF type devices which can be modeled by coupled resonator circuits. In Chapter 4, the technique was applied to CRFs taking into account the particularities of the structure and its filter mechanisms which can be inferred from the proposed models.

Therefore, CRF filter design has also been one of the main aims of this work. An identification of the coupling and resonating mechanisms in the device has facilitated an analytical and systematic way of synthesizing it. Assuming a set of filter requirements and material parameters, the whole filter geometry is obtained from the design process.

A typical CRF device can provide standard Chebyshev type responses. The advantage of applying an analytical tool to design also arises when more advanced responses are required such as Chebyshev responses with transmission zeros to improve the filter selectivity. The insertion of transmission zeros had been thought to be a characteristic typical of ladder filters, but this work has shown that CRFs are also capable of providing it. The coupling matrix has been used to obtain a variety of new configurations based on CRFs that can implement those advanced responses.

Moreover, a way of analyzing CRF devices was presented using the coupling theory. The values of the couplings that take place in the structure are limited depending on the material parameters and the layer configuration. A control on the geometries of the structure enables the desired coupling to be obtained which lies within the range of feasible values. The coupling values are related to the bandwidth of the filter and its return losses. Therefore, the performance limits of the device can be evaluated. The

technique is useful to determine if a set of requirements can be fulfilled by a given structure. It also distinguishes which are the most limiting couplings and gives a clear picture of how they can be improved adding external elements.

In the current spectrum scenario, stringent specifications in terms of rejection can be required for narrow frequency bands. For this reason, in Chapter 5, BAW bandstop filters have been investigated. CRF based structures with Chebyshev type bandstop responses have been proposed. A bandstop coupling matrix synthesis procedure has been used to obtain the coupling values and the configuration for given specifications. The proposed approach uses a direct coupling between source and load to provide transmission and a CRF structure in parallel connection to create the rejection band. Chapter 5 also showed how the proposed filter design can be used to design CRFs in mode-conversion configuration. This functionality of CRFs enables a performance of BAW technology that was formerly carried out by SAW technology or BAW filters combined with baluns.

## 6.2 Future Work

Below, some of the questions that could be addressed in future extensions of this dissertation are detailed.

The proposed filter design approach for CRFs provides a range of possibilities to obtain new structures and devices to meet specifications that may seem beyond their reach. The reconfiguration of the coupling matrix can be used to look for topologies that make sense using BAW coupled resonators. The proposal of new structures and the use of novel materials will entail an accurate modelling.

BAW CRFs are thought to have an acoustic coupling between resonators. Nevertheless, the electric coupling between resonators or between resonators and source/load is the most limiting part of the structure when wide bandwidths must be reached. A possible line of investigation could be on the research of electric coupling mechanisms or elements to improve those couplings.

The analysis of the coupling limits in CRF structures can be used to explore the introduction of external elements to improve their responses. It provides a way of determining which parts of the structure are limiting the response characteristics.

The experimental validation of the results presented in this work is another possible line to follow in the future. That would require a long-term work inside BAW technology facilities or a strong collaboration with a BAW group. The proposed techniques can be used in parallel to a manufacturing process. For example, when deviations of the lower BAW resonators of a CRF regarding the desired characteristics occur once they have already been manufactured, an update of the geometries of the layers that remain to be fabricated can be carried out in order to correct them. This application of the technique could be used for trimming purposes but also for redesigning the coupling layers or other parts of the structure.

# Appendix A

## Properties of Selected Materials

The properties of the materials used in BAW technology depend on the foundry where the thin film devices are manufactured, their processes and the reproducibility. This work has used properties reported in the literature as reference properties and published in [81] and [88]. Table A.1 shows the properties of metals typically used in the BAW industry to implement electrodes or multilayered structures based on the Bragg reflector. Table A.2 shows the properties of piezoelectric materials that may be used as transducers in BAW resonators and non-piezoelectric dielectrics that may be present in a BAW device as for example in the substrate or Bragg reflectors.

**Table A.1:** Acoustic Properties of Metals

Material	Density, $\rho$ (kg/m <sup>3</sup> )	Velocity (m/s), $v$	Impedance, $Z_m$ ( $\times 10^7$ kg/m <sup>2</sup> )	Resistivity ( $\mu\Omega$ cm)
W	19200	5200	9.98	5.39
Mo	10200	6200	6.32	5.7
Al	2700	6300	1.70	2.8
Cu	8900	4700	4.18	1.67

**Table A.2:** Acoustic Properties of Piezoelectric and Dielectric Materials

Material	Density, $\rho$ (kg/m <sup>3</sup> )	Velocity, $v$ (m/s)	Impedance, $Z_m$ ( $\times 10^7$ kg/m <sup>2</sup> )	Piezoelectric Constant, $e$ (C/m <sup>2</sup> )	Relative Per- mittivity, $\epsilon_r$
AlN	3260	11000	3.59	1.5	9.7
ZnO	5665	6350	3.6	1.36	10.8
PZT	7500	4600	3.45	5.87	>70
SiO <sub>2</sub>	2200	5600	1.2	-	3.99
Si	2332	8429	1.95	-	11.7

## Appendix B

# Coupling Matrix Generation

The aim of this Appendix is to provide a brief explanation of the procedure to obtain a coupling matrix of a coupled resonator circuit from a set of filter response specifications. This Appendix is based on the work developed by Cameron published in [79] and [77], and later gathered in the book [76]. Therefore, for any details on the techniques, the reader is referred to the above-mentioned references. Here, the method to obtain the  $N + 2$  coupling matrix presented in [77] which overcomes some of the shortcomings of the original  $N$  matrix [79] will be described.

In order to obtain the coupling matrix conveniently, a coupling matrix generator software has been created during this PhD program. The software is implemented by MATLAB and a graphical user interface has been developed. The coupling matrix generation software has enabled the possibility of implementing multiple and flexible filtering responses. It has been a key tool for the synthesis of advanced responses presented in chapter 4.

## B.1 Polynomial Based Chebyshev Filter Functions

The transfer and reflection Chebyshev functions of a two-port lossless coupled resonator network with  $N$  resonators may be expressed as:

$$S_{21}(s) = \frac{P(s)}{\varepsilon E(s)} \quad (\text{B.1.1})$$

$$S_{11}(s) = \frac{F(s)}{\varepsilon_R E(s)} \quad (\text{B.1.2})$$

where  $s$  is the complex frequency variable and

$$\varepsilon = \frac{1}{\sqrt{10^{RL/10} - 1}} \left. \frac{P(s)}{F(s)} \right|_{s=j} \quad (\text{B.1.3})$$

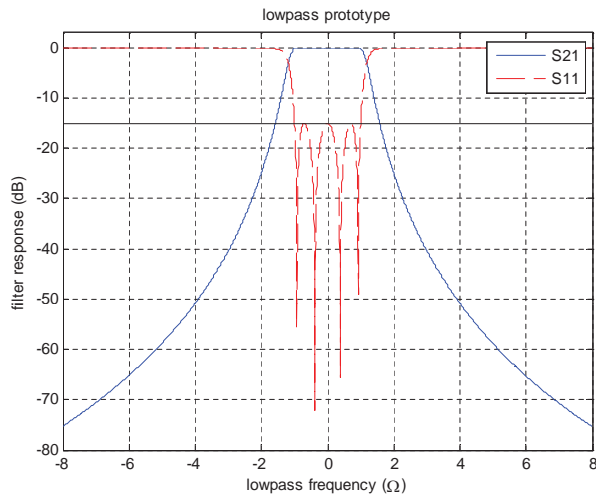
the relationship between the complex frequency variable  $s$  and the prototype lowpass frequency  $\Omega$  is  $s = i\Omega$ .  $RL$  is the return loss in dB and polynomials  $E(s)$ ,  $F(s)$  and  $P(s)$  are normalized to the highest degree coefficient.  $E(s)$  and  $F(s)$  are  $N$  degree polynomials and  $P(s)$  a  $n_{fz}$  degree polynomial.  $n_{fz}$  is the number of finite-position prescribed transmission zeros (TZs) and  $n_{fz} \leq N$  to be a realizable network.

$\varepsilon_R$  is unity for all cases except for fully canonical filtering functions, that is to say the number of TZs equals the order of the filter  $n_{fz} = N$ :

$$\varepsilon_R = \frac{\varepsilon}{\sqrt{\varepsilon^2 - 1}} \quad (\text{B.1.4})$$

The recursive technique and the alternating pole method presented in [79] may be used to obtain the coefficients of the polynomials using as input parameters the filter degree, the position of the prescribed zeros and the  $RL$ .

Figs. B.1–B.4 show example Chebyshev filtering responses and the associated polynomials. The coefficients of the  $E(s)$ ,  $F(s)$  and  $P(s)$  polynomials are normalized to set the highest-degree coefficient to unity. The polynomials that appear in Fig. B.1, B.2 and Fig. B.3 have been used in chapter 4. Fig. B.4 shows a fully canonical filtering response with the same number of finite zeros and filter order.

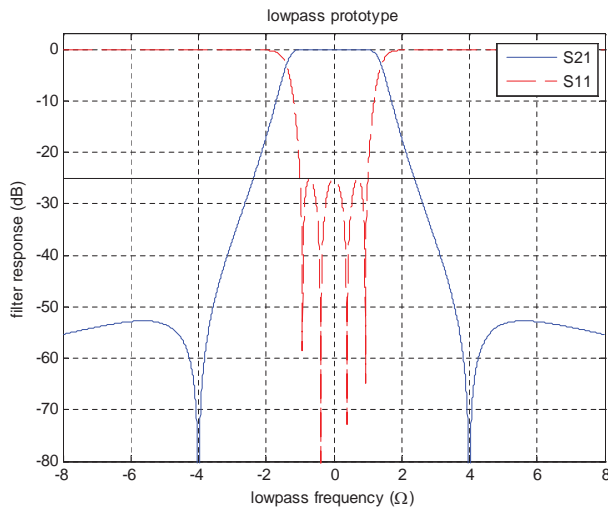


Specifications:

- $N=4$
- $RL=15$  dB
- $TZs=[]$

<i>Polynomial Coefficients</i> ( $\epsilon=1.4457$ and $\epsilon_r=1$ )			
$s^i, i=$	$E(s)$	$F(s)$	$P(s)$
0	0.7029	0.1250	i1.0000
1	1.7673	0.0000	
2	2.3995	1.0000	
3	1.6730	0.0000	
4	1.0000	1.0000	

**Figure B.1:** Classical Chebyshev response without transmission zeros.

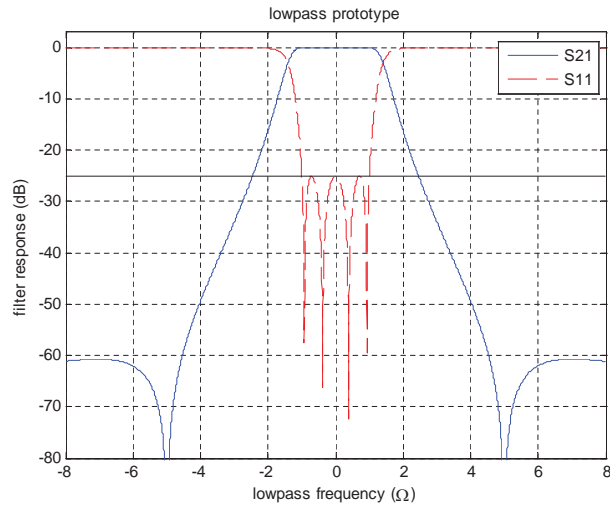


Specifications:

- $N=4$
- $RL=25$  dB
- $TZs=[\pm 4$  rad]

<i>Polynomial Coefficients</i> ( $\epsilon=6.9823$ and $\epsilon_r=1$ )			
$s^i, i=$	$E(s)$	$F(s)$	$P(s)$
0	2.2952	0.1291	i16.0000
1	4.4317	0.0000	0.0000
2	4.4783	1.0081	i1.0000
3	2.6345	0.0000	
4	1.0000	1.0000	

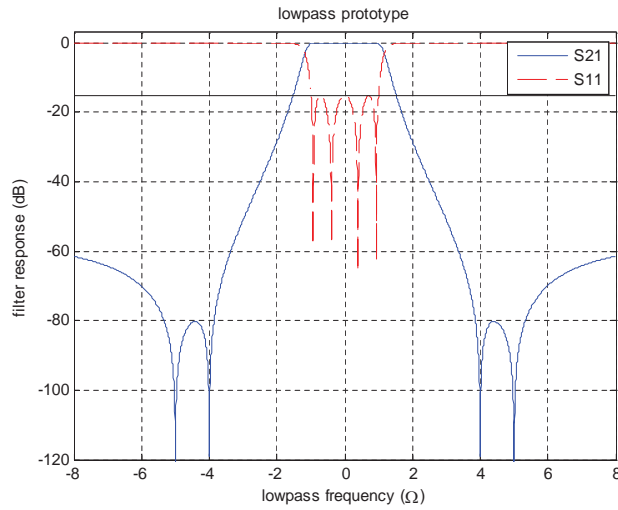
**Figure B.2:** Chebyshev response with finite transmission zeros at  $\pm 4$  rad.



- Specifications:
- $N=4$
  - $RL=25$  dB
  - $TZs=[\pm 5$  rad]

Polynomial Coefficients ( $\epsilon=11.0382$ )			
$s^i, i=$	$E(s)$	$F(s)$	$P(s)$
0	2.2684	0.1276	i25.0000
1	4.4414	0.0000	0.0000
2	4.4949	1.0051	i1.0000
3	2.6419	0.0000	0.0000
4	1.0000	1.0000	0.0000

Figure B.3: Chebyshev response with finite transmission zeros at  $\pm 5$  rad.



- Specifications:
- $N=4$
  - $RL=15$  dB
  - $TZs=[\pm 4$  rad,  $\pm 5$  rad]

Polynomial Coefficients ( $\epsilon=548.7922$ )			
$s^i, i=$	$E(s)$	$F(s)$	$P(s)$
0	0.7407	0.1317	i400.0000
1	1.7817	0.0000	0.0000
2	2.3967	1.0132	i41.0000
3	1.6634	0.0000	0.0000
4	1.0000	1.0000	i1.0000

Figure B.4: Fully canonical filtering function.

## B.2 Coupling Matrix Synthesis

To synthesize the coupling matrix, we consider a two-port admittance parameter matrix  $[Y_N]$ :

$$[Y_N] = \begin{bmatrix} y_{11}(s) & y_{12}(s) \\ y_{21}(s) & y_{22}(s) \end{bmatrix} \quad (\text{B.2.5})$$

First, the matrix will be constructed from the transmission and reflection functions given by (B.1.1) and (B.1.2) respectively. Then, the matrix will be constructed from the transversal array network shown in Fig B.5. The array implements a lowpass filter and then, it is composed of lowpass resonators which comprises one parallel-connected capacitor and one frequency invariant susceptance [77]. Each resonator is coupled to source and load by means of admittance inverters. The direct source–load coupling inverter is included to allow fully canonical transfer functions to be realized. By equating the two constructed  $[Y_N]$  matrices, the elements of the coupling matrix, associated with the transversal array network, will be related to the coefficients of the  $S_{21}$  and  $S_{11}$  polynomials.

### B.2.1 Admittance Matrix $[Y_N]$ from the $S_{21}$ and $S_{11}$ Polynomials

The polynomial ratio for the  $y_{22}(s)$  and  $y_{21}(s)$  elements of  $[Y_N]$  are obtained from the  $S_{21}$  and  $S_{11}$  polynomials:

$$\begin{aligned} \text{For } N_{\text{Even}} : \quad y_{21}(s) &= \frac{y_{21n}(s)}{y_d(s)} = \frac{(P(s)/\varepsilon)}{m_1(s)} \\ y_{22}(s) &= \frac{y_{22n}(s)}{y_d(s)} = \frac{n_1(s)}{m_1(s)} \\ \text{For } N_{\text{Odd}} : \quad y_{21}(s) &= \frac{y_{21n}(s)}{y_d(s)} = \frac{(P(s)/\varepsilon)}{n_1(s)} \\ y_{22}(s) &= \frac{y_{22n}(s)}{y_d(s)} = \frac{m_1(s)}{n_1(s)} \end{aligned} \quad (\text{B.2.6})$$

where

$$\begin{aligned} m_1(s) &= \text{Re}(e_0 + f_0) + j\text{Im}(e_1 + f_1)s + \text{Re}(e_2 + f_2)s^2 + \dots \\ n_1(s) &= j\text{Im}(e_0 + f_0) + \text{Re}(e_1 + f_1)s + j\text{Im}(e_2 + f_2)s^2 + \dots \end{aligned} \quad (\text{B.2.7})$$

$e_i$  and  $f_i$ ,  $i=0,1,2,3,\dots,N$ , are the coefficients of  $E(s)$  and  $F(s)/\varepsilon_r$ .

The residues  $r_{21k}$  and  $r_{22k}$  of  $y_{22}(s)$  and  $y_{21}(s)$  respectively may be found with partial fraction expansions and the eigenvalues of the network  $\lambda_k$  are found by rooting their

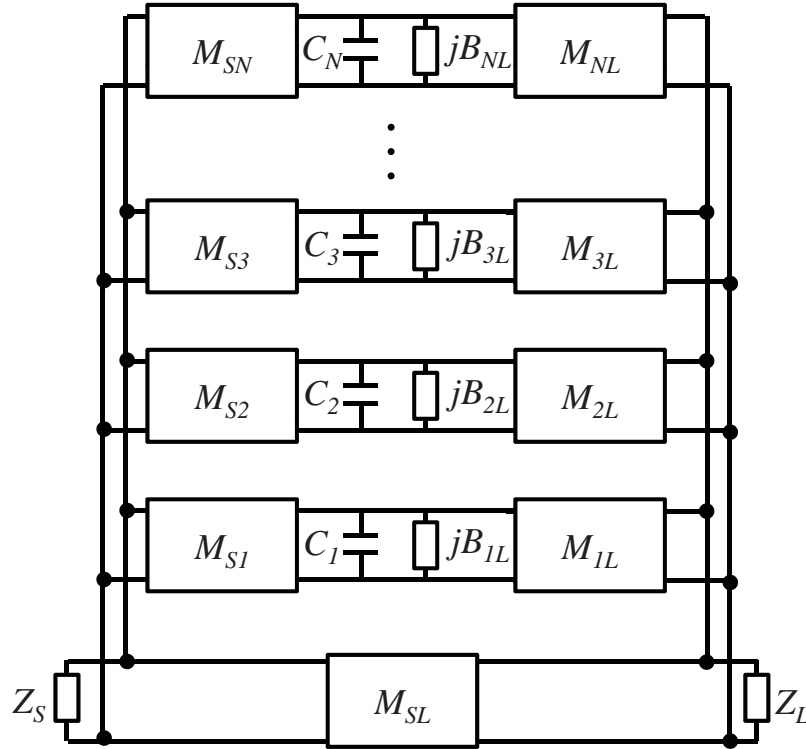


**Figure B.5:** Canonical Transversal Circuit where  $N$  lowpass resonators are coupled to source and load and there exist a direct coupling between source and load.

denominator. Then, the admittance matrix can be expressed as:

$$[Y_N] = \frac{1}{y_d(s)} \begin{bmatrix} y_{11n}(s) & y_{12n}(s) \\ y_{21n}(s) & y_{22n}(s) \end{bmatrix} = j \begin{bmatrix} 0 & K_\infty \\ K_\infty & 0 \end{bmatrix} + \sum_{k=1}^N \frac{1}{(s - j\lambda_k)} \begin{bmatrix} r_{11k} & r_{12k} \\ r_{21k} & r_{22k} \end{bmatrix} \quad (\text{B.2.8})$$

where  $K_\infty = 0$ , except for the fully canonical case:

$$K_\infty = \frac{\varepsilon}{\varepsilon_R} (\varepsilon_R - 1) \quad (\text{B.2.9})$$

And also for the fully canonical case a new polynomial  $y_{21n}'(s)$  is used:

$$y_{21n}'(s) = y_{21n}(s) - jK_\infty y_d(s) \quad (\text{B.2.10})$$

### B.2.2 Admittance Matrix $[Y_N]$ from the Canonical Transversal Array

The admittance matrix  $[Y_N]$  may be obtained from the fully canonical network shown in Fig. B.5.

The admittance matrix of one resonating branch  $k$  is:

$$[y_k] = \begin{bmatrix} y_{11k}(s) & y_{12k}(s) \\ y_{21k}(s) & y_{22k}(s) \end{bmatrix} = \frac{1}{sC_k + jB_k} \begin{bmatrix} M_{S_k}^2 & M_{S_k}M_{L_k} \\ M_{S_k}M_{L_k} & M_{L_k}^2 \end{bmatrix} \quad (\text{B.2.11})$$

Then, the admittance matrix  $[Y_N]$  is obtained by the sum of the admittance matrixes of its branches:

$$[Y_N] = j \begin{bmatrix} 0 & M_{SL} \\ M_{SL} & 0 \end{bmatrix} + \sum_{k=1}^N \frac{1}{(sC_k + jB_k)} \begin{bmatrix} M_{S_k}^2 & M_{S_k}M_{L_k} \\ M_{S_k}M_{L_k} & M_{L_k}^2 \end{bmatrix} \quad (\text{B.2.12})$$

### B.2.3 Transversal Coupling Matrix

The values of the couplings will be obtained equating (B.2.8) and (B.2.12). The direct coupling is  $M_{SL} = K_\infty$  and the following equality can be written:

$$\frac{r_{21k}}{(s - j\lambda_k)} = \frac{M_{S_k}M_{L_k}}{(sC_k + jB_k)} \quad (\text{B.2.13})$$

$$\frac{r_{22k}}{(s - j\lambda_k)} = \frac{M_{L_k}^2}{(sC_k + jB_k)} \quad (\text{B.2.14})$$

Therefore, the values of the couplings and the circuit elements are:

$$\begin{aligned} C_k &= 1 \\ M_{L_k} &= \sqrt{r_{22k}} \\ M_{S_k} &= r_{21k} / \sqrt{r_{22k}} \\ B_k (\equiv M_{kk}) &= -\lambda_k \end{aligned} \quad (\text{B.2.15})$$

The capacitors  $C_k$  of the lowpass resonators are all unity, and the frequency-invariant susceptances  $B_k$  (representing the self couplings  $M_{11} \rightarrow M_{NN}$ ), the input couplings  $M_{S_k}$ , the output couplings  $M_{L_k}$ , and the direct source–load coupling  $M_{SL}$  are all now known, the reciprocal transversal coupling matrix representing the network in Fig. B.5 and expressed in Fig. B.6 may now be constructed.  $M_{S_k}$  are the input couplings and occupy the first row and column of the matrix from positions 1 to  $N$ . Similarly,  $M_{L_k}$  are the output couplings and they occupy the last row and column of from positions 1 to  $N$ . All other entries are zero.

Fig. B.7 shows the transversal coupling matrixes that have been obtained from the polynomials given in Figs. B.1–B.4.

	$S$	1	2	3	...	$k$	...	$N-1$	$N$	$L$
$S$		$M_{S1}$	$M_{S2}$	$M_{S3}$	...	$M_{Sk}$	...	$M_{S,N-1}$	$M_{SN}$	$M_{SL}$
1	$M_{S1}$	$M_{11}$								$M_{L1}$
2	$M_{S2}$		$M_{22}$							$M_{L2}$
3	$M_{S3}$			$M_{33}$						$M_{L3}$
...	...				...					...
$k$	$M_{Sk}$					$M_{kk}$				$M_{Lk}$
...	...									...
$N-1$	$M_{S,N-1}$							$M_{N-1,N-1}$		$M_{L,N-1}$
$N$	$M_{SN}$								$M_{NN}$	$M_{LN}$
$L$	$M_{SL}$	$M_{L1}$	$M_{L2}$	$M_{L3}$	...	$M_{Lk}$	...	$M_{L,N-1}$	$M_{LN}$	

Figure B.6: Canonical coupling matrix  $\mathbf{M}$  for the transversal array

### B.3 Coupling Matrix Reduction

The coupling matrix  $\mathbf{M}$  that was generated in the previous section from the synthesis procedure implements a coupled resonator filter where the couplings occur between source–load, resonator–load and source–resonator. There are no inter-resonator couplings. The diagonal elements represent the offset from the center frequency of the filter of each resonance. Since this configuration may not be practical or that required in some technologies or situations, it is usual to annihilate the couplings with a sequence of similarity transforms or rotations until a more convenient form is obtained. The use of similarity transformations ensures that the eigenvalues and the eigenvectors of the matrix  $\mathbf{M}$  are preserved and therefore, it yields exactly the same transfer and reflection characteristics as the original matrix. For a full description of the coupling matrix reduction procedure see [76] or [79].

### B.4 Graphical User Interface

Fig. B.8 shows the graphical user interface of the coupling generation software that has been developed. The different parts will be described regarding the numbered labels:

1. The specifications are defined for a lowpass prototype frequency response in terms of: return losses (RL), order of the filter ( $N$ ) and the finite complex transmission zeros in the  $s$ -plane.

	$S$	1	2	3	4	$L$
$S$	0	0.3624	-0.5356	0.5356	-0.3624	0
1	0.3624	1.1854	0	0	0	0.3624
2	-0.5356	0	0.5428	0	0	0.5356
3	0.5356	0	0	-0.5428	0	0.5356
4	-0.3624	0	0	0	-1.1854	0.3624
$L$	0	0.3624	0.5356	0.5356	0.3624	0

(a)

	$S$	1	2	3	4	$L$
$S$	0	0.4520	-0.6741	0.6741	-0.4520	0
1	0.4520	1.4797	0	0	0	0.4520
2	-0.6741	0	0.7440	0	0	0.6741
3	0.6741	0	0	-0.7440	0	0.6741
4	-0.4520	0	0	0	-1.4797	0.4520
$L$	0	0.4520	0.6741	0.6741	0.4520	0

(b)

	$S$	1	2	3	4	$L$
$S$	0	0.4569	-0.6721	0.6721	-0.4569	0
1	0.4569	1.4857	0	0	0	0.4569
2	-0.6721	0	0.7367	0	0	0.6721
3	0.6721	0	0	-0.7367	0	0.6721
4	-0.4569	0	0	0	-1.4857	0.4569
$L$	0	0.4569	0.6721	0.6721	0.4569	0

(c)

	$S$	1	2	3	4	$L$
$S$	0	0.3515	-0.5406	0.5406	-0.3515	0.0009
1	0.3515	1.1796	0	0	0	0.3515
2	-0.5406	0	0.5599	0	0	0.5406
3	0.5406	0	0	-0.5599	0	0.5406
4	-0.3515	0	0	0	-1.1796	0.3515
$L$	0.0009	0.3515	0.5406	0.5406	0.3515	0

(d)

**Figure B.7:** (a), (b), (c) and (d) transversal coupling matrixes corresponding to the filter specifications and polynomial coefficients of Figs. B.1, B.2, B.3 and B.4 respectively

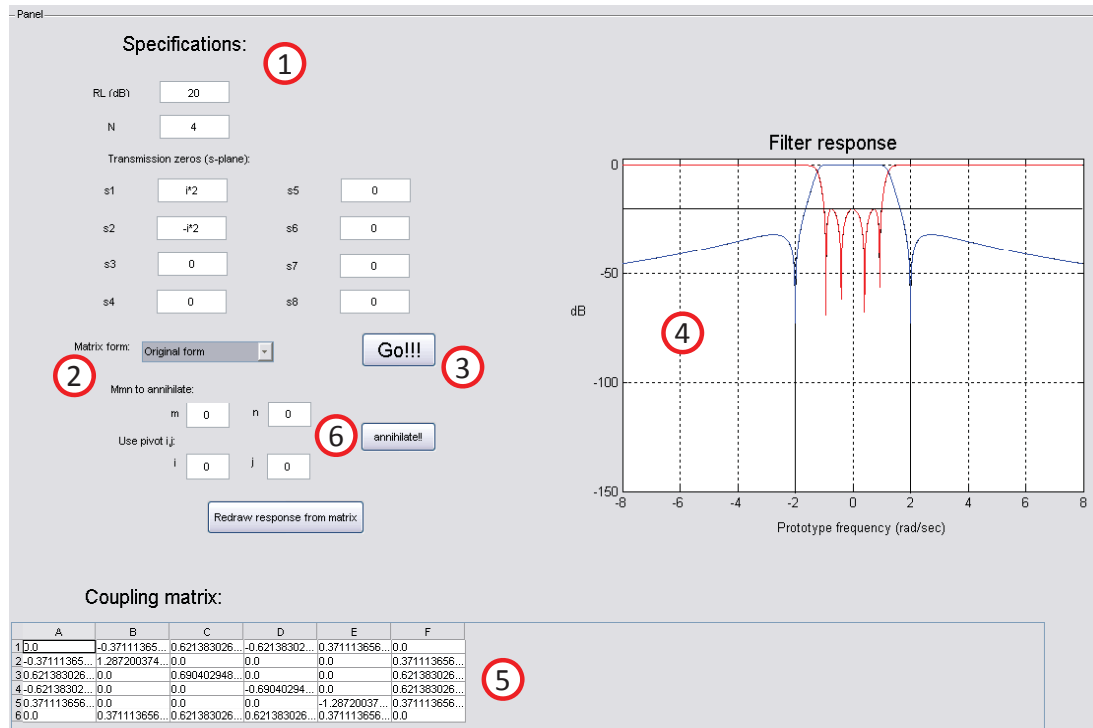


**Figure B.8:** Graphical user interface of the coupling matrix generation software

2. The desired matrix form to be obtained is selected. The routines for some of the most known configurations have been implemented: fully canonical, folded canonical and parallel connected.
3. Button to generate the coupling matrix.
4. Filter response that is generated.
5. Coupling matrix.
6. Similarity transformations can be performed by means of selecting the coupling matrix element to annihilate and the pivot that performs the rotation. The resulting coupling matrix is generated for every rotation.

# Bibliography

- [1] R. Aigner, “RF-MEMS filters manufactured on silicon: key facts about bulk-acoustic-wave technology,” *Silicon Monolithic Integrated Circuits in RF Systems, 2003. Digest of Papers. 2003 Topical Meeting on*, pp. 157 – 161, apr. 2003.
- [2] A. Kennerley and I. Hunter, “Miniature microwave filters using high permittivity ceramics,” *Technologies for Wireless Applications Digest, 1995., MTT-S Symposium on*, pp. 135 –139, feb. 1995.
- [3] T. Ishizaki, M. Fujita, H. Kagata, T. Uwano, and H. Miyake, “A very small dielectric planar filter for portable telephones,” *Microwave Theory and Techniques, IEEE Transactions on*, vol. 42, no. 11, pp. 2017 –2022, Nov. 1994.
- [4] C. Ruppel, L. Reindl, and R. Weigel, “SAW devices and their wireless communications applications,” *IEEE Microwave Magazine*, vol. 3, pp. 65 – 71, 1995.
- [5] J. Bouchaud, “RF MEMS applications, markets and industry,” *MIMOSA Workshop*, 2009.
- [6] K. Lakin, “A review of thin-film resonator technology,” *Microwave Magazine, IEEE*, vol. 4, no. 4, pp. 61 – 67, dec. 2003.
- [7] F. Bi and B. Barber, “Bulk acoustic wave RF technology,” *Microwave Magazine, IEEE*, vol. 9, no. 5, pp. 65 –80, 2008.
- [8] R. Aigner, “High performance RF-filters suitable for above IC integration: film bulk-acoustic- resonators (FBAR) on silicon,” pp. 141 – 146, 2003.
- [9] S. Mahon and R. Aigner, “Bulk Acoustic Wave Devices. Why, How, and Where They are Going ,” pp. 15–18, May 14–17, 2007.

- [10] T. Grudkowski, J. Black, T. Reeder, D. Cullen, and R. Wagner, "Fundamental mode VHF/UHF bulk acoustic wave resonators and filters on silicon," *1980 Ultrasonics Symposium*, pp. 829 – 833, 1980.
- [11] K. Lakin, J. Wang, G. Kline, A. Landin, Y. Chen, and J. Hunt, "Thin film resonators and filters," *1982 Ultrasonics Symposium*, pp. 466 – 475, 1982.
- [12] M. Driscoll, R. Moore, J. Rosenbaum, S. Krischnaswamy, and J. Szedon, "Recent advances in monolithic film resonator technology," *IEEE Ultrasonics Symposium*, p. 365, 1986.
- [13] K. Lakin, "Thin film resonators and filters," *Ultrasonics Symposium, 1999. Proceedings. 1999 IEEE*, vol. 2, pp. 895 –906 vol.2, 1999.
- [14] M. Johnston, I. Kymissis, and K. Shepard, "FBAR-CMOS oscillator array for mass-sensing applications," *Sensors Journal, IEEE*, vol. 10, no. 6, pp. 1042 –1047, 2010.
- [15] D. Petit, E. Cesar, P. Bar, S. Joblot, G. Parat, O. Berchaud, D. Barbier, and J.-F. Carpentier, "Thermally stable oscillator at 2.5 Ghz using temperature compensated BAW resonator and its integrated temperature sensor," pp. 895 –898, 2008.
- [16] R. Ruby, P. Bradley, Y. Oshmyansky, A. Chien, and I. Larson, J.D., "Thin film bulk wave acoustic resonators (FBAR) for wireless applications," *IEEE Ultrasonics Symposium*, vol. 1, pp. 813 – 821, Oct. 2001.
- [17] K. Lakin, G. Kline, and K. McCarron, "Development of miniature filters for wireless applications," *Microwave Theory and Techniques, IEEE Transactions on*, vol. 43, no. 12, pp. 2933 –2939, dec. 1995.
- [18] W. Newell, "Face-mounted piezoelectric resonators," *Proceedings of the IEEE*, vol. 53, no. 6, pp. 575 – 581, jun. 1965.
- [19] R. Ruby, "Review and comparison of bulk acoustic wave FBAR, SMR technology," *Ultrasonics Symposium, 2007. IEEE*, pp. 1029 –1040, oct. 2007.
- [20] S. Marksteiner, J. Kaitila, G. Fattinger, and R. Aigner, "Optimization of acoustic mirrors for solidly mounted BAW resonators," *Ultrasonics Symposium, 2005 IEEE*, vol. 1, pp. 329 – 332, sep. 2005.

- 
- [21] R. Aigner, "Volume manufacturing of BAW-filters in a CMOS fab," in *Acoustic Wave Device Symposium*, Chiba, Japan, Mar. 2004.
- [22] —, "Bringing BAW technology into volume production: The ten commandments and the seven deadly sins," *Proceedings of International Chiba Symposium on Acoustic Wave Devices*, mar. 2007.
- [23] D. M. Pozar, *Microwave Engineering, 3rd edition*. John Wiley & Sons, 2005.
- [24] G. Fattinger, "BAW resonator design considerations - an overview," pp. 762–767, May 2008.
- [25] I. Larson, J.D., P. Bradley, S. Wartenberg, and R. Ruby, "Modified Butterworth-Van Dyke circuit for FBAR resonators and automated measurement system," *Ultrasonics Symposium, 2000 IEEE*, vol. 1, pp. 863–868 vol.1, oct. 2000.
- [26] W. Xu, A. Abbaspour-Tamijani, and J. Chae, "Oscillating behavior of quality factor of a film bulk acoustic resonator in liquids," pp. 696–699, 2009.
- [27] P. Muralt, J. Antifakos, M. Cantoni, R. Lanz, and F. Martin, "Is there a better material for thin film BAW applications than AlN?" *Ultrasonics Symposium, 2005 IEEE*, vol. 1, pp. 315–320, sep. 2005.
- [28] Q. Su, P. Kirby, E. Komuro, M. Imura, Q. Zhang, and R. Whatmore, "Thin-film bulk acoustic resonators and filters using ZnO and lead-zirconium-titanate thin films," *Microwave Theory and Techniques, IEEE Transactions on*, vol. 49, no. 4, pp. 769–778, apr. 2001.
- [29] J. Kaitila, "Review of Wave Propagation in BAW Thin Film Devices - Progress and Prospects," *Ultrasonics Symposium, 2007. IEEE*, pp. 120–129, 28-31 Oct. 2007.
- [30] S.-H. Lee, J.-H. Kim, G. Mansfeld, K. Yoon, and J.-K. Lee, "Influence of electrodes and Bragg reflector on the quality of thin film bulk acoustic wave resonators," pp. 45–49, 2002.
- [31] K. Lakin, J. Belsick, J. McDonald, and K. McCarron, "Improved bulk wave resonator coupling coefficient for wide bandwidth filters," *Ultrasonics Symposium, 2001 IEEE*, vol. 1, pp. 827–831 vol.1, 2001.

- [32] E. Iborra, M. Clement, J. Olivares, J. Sangrador, N. Rimmer, and A. Rastogi, "Aluminum nitride bulk acoustic wave devices with iridium bottom electrodes," *Ultrasonics Symposium, 2007. IEEE*, pp. 616 –619, oct. 2007.
- [33] K. Zhang, H. Gu, G. Hu, and W. Li, "Membrane structure FBAR fabricated with highly c-axis oriented AlN film based on platinum electrode," *Solid-State and Integrated Circuit Technology, 2006. ICSICT '06. 8th International Conference on*, pp. 596 – 598, 2006.
- [34] Y. Aota, S. Tanifuji, H. Oguma, S. Kameda, H. Nakase, T. Takagi, and K. Tsubouchi, "FBAR characteristics with AlN film using MOCVD method and Ru/Ta electrode," *Ultrasonics Symposium, 2007. IEEE*, pp. 1425 – 1428, 2007.
- [35] K. Lakin, K. McCarron, and J. McDonald, "Temperature compensated bulk acoustic thin film resonators," vol. 1, pp. 855 –858 vol.1, Oct. 2000.
- [36] S. Krishnaswamy, J. Rosenbaum, S. Horwitz, C. Vale, and R. Moore, "Film bulk acoustic wave resonator technology," *Ultrasonics Symposium, 1990. Proceedings., IEEE 1990*, vol. 1, pp. 529 –536, Dec. 1990.
- [37] K. Lakin, G. Kline, and K. McCarron, "Thin film bulk acoustic wave filters for GPS," vol. 1, pp. 471 – 476, Oct. 1992.
- [38] O. Menendez, P. de Paco, R. Villarino, and J. Parron, "Closed-form expressions for the design of ladder-type FBAR filters," *Microwave and Wireless Components Letters, IEEE*, vol. 16, no. 12, pp. 657 –659, dec. 2006.
- [39] L. Mang and F. Hickernell, "ZnO thin film resonator lattice filters," *Frequency Control Symposium, 1996. 50th., Proceedings of the 1996 IEEE International.*, pp. 363 –365, jun. 1996.
- [40] E. Kerherve, P. Ancey, M. Aid, and A. Kaiser, "BAW technologies: Development and applications within MARTINA, MIMOSA and MOBILIS IST european projects," pp. 341 –350, 2006.
- [41] H. Jin, S. Dong, and D. Wang, "Design of balanced RF filter for wireless applications using FBAR technology," pp. 57 –60, 2005.
- [42] A. Ballato and T. Lukaszek, "Stacked-crystal filters," *Proceedings of the IEEE*, vol. 61, no. 10, pp. 1495 – 1496, oct. 1973.

- [43] K. Lakin, G. Kline, R. Ketcham, J. Martin, and K. McCarron, "Stacked crystal filters implemented with thin films," *Frequency Control, 1989., Proceedings of the 43rd Annual Symposium on*, pp. 536 –543, may. 1989.
- [44] K. Lakin, J. Belsick, J. McDonald, K. McCarron, and C. Andrus, "Bulk acoustic wave resonators and filters for applications above 2 ghz," vol. 3, pp. 1487 –1490, 2002.
- [45] K. Lakin, "Equivalent circuit modeling of stacked crystal filters," *Thirty Fifth Annual Frequency Control Symposium. 1981*, pp. 257 – 262, 1981.
- [46] —, "Modeling of thin film resonators and filters," vol. 1, pp. 149 – 152, June 1992.
- [47] K. M. Lakin, "Coupled resonator filters," *IEEE Ultrasonics Symposium*, vol. 1, pp. 901–908, Oct. 2002.
- [48] P. de Paco, O. Menendez, and E. Corrales, "Equivalent circuit modeling of coupled resonator filters," *Ultrasonics, Ferroelectrics and Frequency Control, IEEE Transactions on*, vol. 55, no. 9, pp. 2030 –2037, sep. 2008.
- [49] A. Volatier, E. Defay, A. N'hari, J. F. Carpentier, P. Ancey, and B. Dubus, "Design, elaboration and characterization of coupled resonator filters for WCDMA applications," *IEEE Ultrasonics Symposium*, pp. 829–832, Oct. 2006.
- [50] M. Small, T. Jamneala, L. Callaghan, J. Larson, and R. Ruby, "A de-coupled stacked bulk acoustic resonator (DSBAR) filter with 2 dB bandwidth > 4%," *Ultrasonics Symposium*, pp. 604 – 607, 2007.
- [51] T. Jamneala, M. Small, R. Ruby, and J. Larson, "Coupled resonator filter with single-layer acoustic coupler," *Ultrasonics, Ferroelectrics and Frequency Control, IEEE Transactions on*, vol. 55, no. 10, pp. 2320 –2326, 2008.
- [52] G. Fattinger, R. Aigner, and W. Nessler, "Coupled bulk acoustic wave resonator filters: key technology for single-to-balanced RF filters," vol. 2, pp. 927 – 929, 2004.
- [53] G. Fattinger, J. Kaitila, R. Aigner, and W. Nessler, "Single-to-balanced filters for mobile phones using coupled resonator BAW technology," *Ultrasonics Symposium, 2004 IEEE*, vol. 1, pp. 416 – 419 Vol.1, aug. 2004.

- [54] L. Mourot, P. Bar, C. Arnaud, G. Parat, and J.-F. Carpentier, "Coupled resonator filters for W-CDMA duplexer application," pp. 214 –217, 2008.
- [55] K. Lakin, "Thin film BAW filters for wide bandwidth and high performance applications," vol. 2, pp. 923 – 926, 2004.
- [56] M. Allah, J. Kaitila, R. Thalhammer, W. Weber, and D. Schmitt-Landsiedel, "Temperature compensated solidly mounted resonators with thin SiO<sub>2</sub> layers," *Ultrasonics Symposium (IUS), 2009 IEEE International*, pp. 859 –862, 2009.
- [57] K. Lakin, J. Belsick, J. McDonald, and K. McCarron, "Improved bulk wave resonator coupling coefficient for wide bandwidth filters," *Ultrasonics Symposium, 2001 IEEE*, vol. 1, pp. 827 –831, 2001.
- [58] D. Petit, N. Abele, A. Volatier, A. Lefevre, P. Ancey, and J.-F. Carpentier, "Temperature compensated bulk acoustic wave resonator and its predictive 1D acoustic tool for RF filtering," *Ultrasonics Symposium, 2007. IEEE*, pp. 1243 –1246, 2007.
- [59] J. David and N. Cheeke, *Fundamentals and Applications of Ultrasonic Waves*. CRC Press LLC, 2002.
- [60] J. Rosenbaum, *Bulk Acoustic Wave Theory and Devices*. Artech House, 1988.
- [61] B. A. Auld, *Fundamentals and Applications of Ultrasonic Waves*. Wiley, 1973.
- [62] E. Sittig, *Physical Acoustics, vol.IX*. Eds. W.P. Mason and R.N. Thurston (Academic Press), 1972.
- [63] R. Weigel, D. Morgan, J. Owens, A. Ballato, K. Lakin, K. Hashimoto, and C. Ruppel, "Microwave acoustic materials, devices, and applications," *Microwave Theory and Techniques, IEEE Transactions on*, vol. 50, no. 3, pp. 738 –749, mar. 2002.
- [64] W. Chen and D. Han, *Plasticity for Structural Engineers*. J. Ross, 2007.
- [65] K. Lakin, "Fundamental properties of thin film resonators," *Frequency Control, 1991., Proceedings of the 45th Annual Symposium on*, pp. 201 –206, may. 1991.
- [66] S. Salgar, G. Kim, D.-H. Han, and B. Kim, "Modeling and simulation of the thin film bulk acoustic resonator," *Frequency Control Symposium and PDA Exhibition, 2002. IEEE International*, pp. 40–44, 2002.

- [67] K. Nakamura and H. Kanbara, "Theoretical analysis of a piezoelectric thin film resonator with acoustic quarter-wave multilayers," *Frequency Control Symposium, 1998. Proceedings of the 1998 IEEE International*, pp. 876–881, 27–29 May 1998.
- [68] S.-H. Kim, J.-H. Kim, J.-K. Lee, S.-H. Lee, and K. H. Yoon, "Bragg reflector thin film resonator using aluminium nitride deposited by RF sputtering," *Microwave Conference, 2000 Asia-Pacific*, pp. 1535–1538, 2000.
- [69] O. Menendez, P. de Paco, J. Gemio, J. Verdu, and E. Corrales, "Methodology for designing microwave acoustic filters with Butterworth/Chebyshev response," *International Journal of Microwave and Wireless Technologies*, vol. 1, pp. 11–18, Mar. 2009.
- [70] A. Reinhardt, V. Laude, R. Lanz, P. Muralt, M. Solal, S. Ballandras, and W. Steichen, "Design of coupled resonator filters using admittance and scattering matrices," *IEEE Ultrasonics Symposium*, vol. 2, pp. 1428–1431, Oct. 5–8, 2003.
- [71] A. Ballato and T. Lukaszek, "A Novel Frequency Selective Device: The Stacked-Crystal Filter," *27th Annual Symposium on Frequency Control. 1973*, pp. 262–276, 1973.
- [72] J. S. G. Hong and M. J. Lancaster, *Microstrip Filters for RF/Microwave Applications*. John Wiley & Sons, 2001.
- [73] K. M. Lakin, "Coupled resonator filters bulk acoustic wave coupled resonator filters," *IEEE International Frequency Control Symposium and PDA Exhibition*, pp. 8–14, 2002.
- [74] J. Olivares, E. Wegmann, M. Clement, J. Capilla, E. Iborra, and J. Sangrador, "Wide bandwidth bragg mirrors for multi-band filter chips," pp. 2119–2122, 2009.
- [75] J. Kaitila and G. Fattinger, "Measurement of acoustical parameters of thin films," *Ultrasonics Symposium, 2006. IEEE*, pp. 464–467, oct. 2006.
- [76] R. J. Cameron, R. Mansour, and C. M. Kudsia, *Microwave Filters for Communication Systems: Fundamentals, Design and Applications*. Wiley-Interscience, 2007.
- [77] R. Cameron, "Advanced coupling matrix synthesis techniques for microwave filters," *Microwave Theory and Techniques, IEEE Transactions on*, vol. 51, no. 1, pp. 1–10, jan. 2003.

- 
- [78] A. Atia and A. Williams, "Narrow-bandpass waveguide filters," *Microwave Theory and Techniques, IEEE Transactions on*, vol. 20, no. 4, pp. 258 – 265, apr. 1972.
- [79] R. Cameron, "General coupling matrix synthesis methods for Chebyshev filtering functions," *Microwave Theory and Techniques, IEEE Transactions on*, vol. 47, no. 4, pp. 433 –442, apr. 1999.
- [80] D. Swanson and G. Macchiarella, "Microwave filter design by synthesis and optimization," *Microwave Magazine, IEEE*, vol. 8, no. 2, pp. 55 –69, apr. 2007.
- [81] K. Y. Hashimoto, *RF bulk acoustic wave filters for communications*. Artech House, 2009.
- [82] R. Levy, "Filters with single transmission zeros at real or imaginary frequencies," *Microwave Theory and Techniques, IEEE Transactions on*, vol. 24, no. 4, pp. 172 – 181, Apr. 1976.
- [83] L. Mourot, P. Bar, G. Parat, P. Ancey, S. Bila, and J.-F. Carpentier, "Stopband filters built in the BAW technology [application notes]," *Microwave Magazine, IEEE*, vol. 9, no. 5, pp. 104 –116, 2008.
- [84] J.-R. Qian and W.-C. Zhuang, "New narrow-band dual-mode bandstop waveguide filters," *Microwave Theory and Techniques, IEEE Transactions on*, vol. 31, no. 12, pp. 1045 –1050, 1983.
- [85] R. Cameron, M. Yu, and Y. Wang, "Direct-coupled microwave filters with single and dual stopbands," *Microwave Theory and Techniques, IEEE Transactions on*, vol. 53, no. 11, pp. 3288 – 3297, 2005.
- [86] S. Gilbert, R. Parker, M. Small, U. Koelle, J. Larson, and R. Ruby, "An ultra-miniature, low cost single ended to differential filter for ISM band applications," pp. 839 –842, 2008.
- [87] R. Ruby, S. Gilbert, A. Chien, and T. Jamneala, "GPS and WiFi single ended to differential CRF filters using SiOCH as a de-coupling layer," pp. 872 –875, 2009.
- [88] I. Larson, J.D., S. Gilbert, and B. Xu, "PZT material properties at UHF and microwave frequencies derived from FBAR measurements," vol. 1, pp. 173 – 177 Vol.1, 2004.